

FULL ENVELOPE NONLINEAR CONTROLLER DESIGN FOR A NOVEL  
ELECTRIC VTOL(EVTOL) AIR-TAXI VIA INDI APPROACH COMBINED  
WITH CA

A THESIS SUBMITTED TO  
THE GRADUATE SCHOOL OF NATURAL AND APPLIED SCIENCES  
OF  
MIDDLE EAST TECHNICAL UNIVERSITY

BY

EMRE CAN SUIÇMEZ

IN PARTIAL FULFILLMENT OF THE REQUIREMENTS  
FOR  
THE DEGREE OF DOCTOR OF PHILOSOPHY  
IN  
AEROSPACE ENGINEERING

MAY 2021



Approval of the thesis:

**FULL ENVELOPE NONLINEAR CONTROLLER DESIGN FOR A NOVEL  
ELECTRIC VTOL(EVTOL) AIR-TAXI VIA INDI APPROACH COMBINED  
WITH CA**

submitted by **EMRE CAN SUIÇMEZ** in partial fulfillment of the requirements for  
the degree of **Doctor of Philosophy in Aerospace Engineering Department, Middle East Technical University** by,

Prof. Dr. Halil Kalıpçılar  
Dean, Graduate School of **Natural and Applied Sciences**

\_\_\_\_\_

Prof. Dr. İsmail H. Tuncer  
Head of Department, **Aerospace Engineering**

\_\_\_\_\_

Assist. Prof. Dr. Ali Türker Kutay  
Supervisor, **Aerospace Engineering, METU**

\_\_\_\_\_

**Examining Committee Members:**

Prof. Dr. Ozan Tekinalp  
Aerospace Engineering, METU

\_\_\_\_\_

Assist. Prof. Dr. Ali Türker Kutay  
Aerospace Engineering, METU

\_\_\_\_\_

Prof. Dr. Kemal Leblebicioğlu  
Electrical and Electronics Engineering, METU

\_\_\_\_\_

Prof. Dr. Coşku Kasnakoğlu  
Electrical and Electronics Engineering, TOBB ETÜ

\_\_\_\_\_

Prof. Dr. Metin Uymaz Salamcı  
Mechanical Engineering, Gazi University

\_\_\_\_\_

Date: 21.05.2021

**I hereby declare that all information in this document has been obtained and presented in accordance with academic rules and ethical conduct. I also declare that, as required by these rules and conduct, I have fully cited and referenced all material and results that are not original to this work.**

Name, Surname: EMRE CAN SUIÇMEZ

Signature :

## **ABSTRACT**

### **FULL ENVELOPE NONLINEAR CONTROLLER DESIGN FOR A NOVEL ELECTRIC VTOL(EVTOL) AIR-TAXI VIA INDI APPROACH COMBINED WITH CA**

SUIÇMEZ, EMRE CAN

Ph.D., Department of Aerospace Engineering

Supervisor: Assist. Prof. Dr. Ali Türker Kutay

May 2021, 144 pages

On-demand urban air mobility (UAM) has become very popular in recent years with the introduction of the electric vertical take-off and landing (eVTOL) aircraft concept. Thanks to the key advantages of electric propulsion (e.g., very low noise and zero carbon-emission), short/medium range eVTOL "air-taxi" concept emerged as a feasible solution considering the requirements of the on-demand UAM. With this motivation, flight control problems of a novel eVTOL air-taxi are discussed and a unified flight controller is designed considering the full flight envelope. The air-taxi has a fixed-wing surface to have aerodynamically efficient forward flight, and uses only tilting electric propulsion units (i.e. the pure thrust vector control) to achieve full envelope flight control. The aircraft does not have any conventional control and stability surfaces such as aileron, elevator, rudder, horizontal/vertical tail. Therefore, the unified controller design becomes more challenging compared to the conventional aircraft configuration. The flight dynamics model of the air-taxi does not exist in literature since the air-taxi has a novel configuration. First, a preliminary flight dynamics model is generated using the component build-up approach for hover and high speed forward flight. Then, the hover and forward flight models are merged to simulate the

transition dynamics. Two main challenges regarding the flight control are the severe nonlinearities in the flight dynamics during the transition flight and deterioration of the controller's performance in specific flight conditions due to the limited control authority (i.e., the actuator saturation). The first challenge is resolved via designing a sensor-based nonlinear controller for the entire flight envelope using the Incremental Nonlinear Dynamic Inversion (INDI) method. The INDI approach has improved robustness to modeling errors compared to the classical nonlinear dynamic inversion (NDI) methods. Therefore, the INDI based controller design fits very well to the problem considering the severe nonlinearities in the flight dynamics model. The INDI controller is formulated specifically considering the highly coupled pure thrust vector control approach. For the second problem, an online optimization-based Control Allocation (CA) algorithm is designed and integrated into the INDI controller. Resolving the actuator saturation related problems requires special attention due to the thrust vector control's coupled nature. The CA prioritizes the rotational channels over the translational channels to adequately allocate the limited control authority in case of actuator saturation. Various nonlinear simulation tests are performed considering the full envelope flight control, disturbance rejection characteristics at limited control authority and criticality of the CA design, robustness to model parameters, etc. Simulation results show that the controller has satisfactory performance, disturbance rejection characteristics, and significant robustness to the modeling errors. Moreover, it is observed that the CA plays a vital role in guaranteeing stable flight in case of severe actuator saturation.

**Keywords:** Incremental Nonlinear Dynamic Inversion (INDI), Control Allocation (CA), Actuator Saturation, Thrust Vector Control, Distributed Electric Propulsion (DEP), Vertical Takeoff and Landing (VTOL), Air-taxi, On-demand Urban Air Mobility (UAM)

## ÖZ

### ÖZGÜN BİR ELEKTRİKLİ VTOL (EVTOL) HAVA-TAKSİ'NİN TÜM UÇUŞ ZARFI İÇİN İNDİ VE CA YÖNTEMLERİ KULLANILARAK DOĞRUSAL OLMAYAN KONTROLCÜ TASARIMI

SUIÇMEZ, EMRE CAN

Doktora, Havacılık ve Uzay Mühendisliği Bölümü

Tez Yöneticisi: Dr. Öğr. Üyesi. Ali Türker Kutay

Mayıs 2021 , 144 sayfa

İsteğe bağlı kentsel hava ulaşımı (UAM), elektrikli dikey kalkış ve iniş (eVTOL) uçak konseptinin ortaya çıkması ile son yıllarda çok popüler hale geldi. Elektrikli tahrikin temel avantajları sayesinde (örneğin, çok düşük gürültü ve sıfır karbon emisyonu), kısa /orta menzilli eVTOL "hava-taksi" konsepti, isteğe bağlı UAM'nin gereklilikleri göz önüne alındığında uygulanabilir bir çözüm olarak ortaya çıkmıştır. Bu motivasyonla, özgün bir eVTOL hava taksinin uçuş kontrol ile ilgili sorunları analiz edilerek, tam uçuş zarfını kapsayan birleşik bir uçuş kontrolcüsü tasarlanmıştır. Hava taksi, ileri uçuşta aerodinamik olarak verimli sabit kanat yüzeyine sahiptir ve tam zarf uçuş kontrolünü sağlamak için sadece dönebilen elektrikli tahrik ünitelerini (saf itki vektörü kontrolünü) kullanır. Uçakta kanatçık, irtifa dümeni, dümen, dikey/yatay kuyruk gibi herhangi bir geleneksel kontrol ve stabilite yüzeyi yoktur. Bu nedenle, birleşik kontrolcü tasarımı geleneksel uçak konfigürasyonuna kıyasla daha zorlu hale gelir. Hava taksi özgün bir konfigürasyona sahip olduğu için uçuş dinamiği modeli literatürde mevcut değildir. İlk olarak, "hover" ve yüksek hızlı ileri uçuş için

"component build-up" yaklaşımı kullanılarak başlangıç seviyesinde bir uçuş dinamiği modeli oluşturulur. Daha sonra, geçiş dinamiklerini simüle etmek için "hover" ve ileri uçuş modelleri birleştirilir. Uçuş kontrolü ile ilgili iki temel zorluk, geçiş uçuşu sırasında uçuş dinamiklerindeki ciddi derecede doğrusal olmayan etkiler ve sınırlı kontrol otoritesi (yani eyleyici doygunluğu) nedeniyle kontrolcünün belirli uçuş koşullarında performansının bozulmasıdır. İlk zorluk, tüm uçuş zarfı için sensör-tabanlı doğrusal olmayan Artımlı Doğrusal Olmayan Dinamik Ters Çevirme (INDI) yöntemine dayanan bir kontrolcü tasarlayarak çözülür. INDI yaklaşımı, klasik doğrusal olmayan dinamik ters çevirme (NDI) yöntemlerine kıyasla modelleme hatalarına karşı daha gürbüzdür. Uçuş dinamiği modelindeki ciddi doğrusal olmama durumları göz önünde bulundurulduğunda, INDI yaklaşımı kontrol probleminin çözümü için çok uygun bir yöntemdir. INDI kontrolcüsü, yüksek oranda birleşik dinamiğe sahip, saf itme vektörü kontrol yaklaşımı dikkate alınarak özel olarak formüle edilmiştir. İkinci sorunun çözümü için, çevrimiçi optimizasyon tabanlı bir Kontrol Tahsisi (CA) algoritması tasarlanmış ve INDI kontrolcüsüne entegre edilmiştir. Eyleyici doygunluğu ile ilgili sorunların çözülmesi, itki vektörü kontrolünün birleşik doğası nedeniyle özel dikkat gerektirir. CA, eyleyici doygunluğu durumunda, sınırlı kontrol yetkisini uygun şekilde tahsis etmek için rotasyonel kanalların kontrolüne çizgisel kanallara göre daha çok öncelik verir. Tam zarf uçuş kontrolü, sınırlı kontrol otoritesinde bozucu etkilerin giderilmesi ve CA tasarımının kritikliği, model parametrelerine olan gürbüzlük, vb. dikkate alınarak çok sayıda doğrusal olmayan simülasyon testi gerçekleştirilmiştir. Simülasyon sonuçları, kontrolcünün tatmin edici performansa, bozucu etkileri giderme ve modelleme hatalarına karşı ciddi derecede gürbüzlük özelliklerine sahip olduğunu göstermektedir. Ayrıca, CA'nın ciddi derecedeki eyleyici doygunluğu durumunda istikrarlı uçuşu garanti etmede hayati bir rol oynadığı gözlenmiştir.

Anahtar Kelimeler: Artımlı Doğrusal Olmayan Dinamik Ters Çevirme (INDI), Kontrol Tahsisi (CA), Eyleyici Doygunluğu, İtke Vektörü Kontrolü, Dağıtılmış Elektrikli Tahrik (DEP), Dikey İniş ve Kalkış (VTOL), Hava-taksi, İsteğe Bağlı Kentsel Hava Ulaşımı (UAM)



*To my precious little girl Arya, my beloved wife and family*

## ACKNOWLEDGMENTS

First of all, I would like to express my sincere gratitude to my advisor Assist. Prof. Dr. Ali Türker Kutay for its invaluable guidance, support and advice throughout my research and education.

I would also like to express my gratitude to my thesis committee members, Prof. Dr. Ozan Tekinalp, Prof. Dr. Kemal Leblebiciođlu, Prof. Dr. Cořku Kasnakođlu, and Prof. Dr. Metin Uymaz Salamcı for their beneficial reviews and support.

I would like to thank entire academic staff of Department of Aerospace Engineering. I'm also grateful to administrative staff of Aerospace Engineering Department and special thanks to Derya Kaya and Nilgün Kaplan for their understanding and supportive attitudes.

I am also thankful to all of my colleagues especially Halil Kutay, Hakan Tiftikçi, Ercüment Türkođlu, Valentin Machanek, and Jens Dodenhöft for their valuable guidance and support.

I would like to express my sincere thanks to my lovely family, Halit, Nurcan, řencan, Tekin, İbrahim, İlknur and our little ones Ezgi, Efe and Arya. I would like to specially thank my father and mother for their invaluable support and love especially at challenging times. I also thank God to give me the opportunity to meet my sweetheart Tuđba who helped me at each stage of my life with her endless love and support.

Finally, I would like to express my sincere gratitude to The Scientific and Technological Research Council of Turkey (TÜBİTAK) for its scholarship support.

## TABLE OF CONTENTS

ABSTRACT . . . . .	v
ÖZ . . . . .	vii
ACKNOWLEDGMENTS . . . . .	x
TABLE OF CONTENTS . . . . .	xi
LIST OF TABLES . . . . .	xv
LIST OF FIGURES . . . . .	xvi
LIST OF ABBREVIATIONS . . . . .	xx
CHAPTERS	
1 INTRODUCTION . . . . .	1
1.1 eVTOL Air-Taxi Concepts with Distributed Electric Propulsion (DEP) . . . . .	3
1.1.1 Pros and cons of DEP Considering the Requirements of on-demand UAM . . . . .	3
1.1.2 DEP eVTOL Air-taxi Concepts . . . . .	6
1.1.2.1 Long Range DEP eVTOL Air-taxi Concepts . . . . .	8
1.2 Motivation and Contributions of the Thesis . . . . .	9
1.3 Organization and Overview of the Chapters . . . . .	13
2 FLIGHT DYNAMICS MODELING . . . . .	17
2.1 Aerodynamic Modeling . . . . .	18

2.1.1	Forward Flight: Wing-Body Aerodynamic Modeling . . . . .	19
2.1.1.1	Generating the Digital DATCOM Input File . . . . .	20
2.1.1.2	Digital DATCOM Results . . . . .	21
2.1.1.3	Wing-Body Aerodynamic Forces and Moments . . . . .	27
2.1.2	Hover Flight: Estimation of Aerodynamic Resistance Force . .	29
2.1.3	Complete Aerodynamic Model Considering the Transition . .	30
2.2	Electric Ducted Fan(EDF) Modeling . . . . .	31
2.2.1	Estimation of the Thrust and Torque Coefficients . . . . .	32
2.2.2	Deciding on the Total Number of EDFs and Their Distribution	35
2.2.3	EDF Propulsion Forces and Moments . . . . .	36
2.2.4	EDF Actuator Dynamics . . . . .	38
2.3	Sensor Modeling . . . . .	40
2.4	6-DOF Equations Of Motion . . . . .	41
3	UNIFIED FLIGHT CONTROLLER: DESIGN, VERIFICATION AND DIS- CUSSION . . . . .	45
3.1	Challenges of the Unified Controller Design and Main Contributions .	45
3.2	LQR Controller Design . . . . .	50
3.2.1	Reduced Size Control Input Definitions . . . . .	51
3.2.2	Trim & Linearization . . . . .	52
3.2.2.1	Simplified Trim Algorithm . . . . .	53
3.2.2.2	Main Trim Algorithm . . . . .	55
3.2.2.3	Linearization . . . . .	55
3.2.3	Design of the LQR Cruise Controller . . . . .	56

3.2.3.1	Trim Point Search . . . . .	56
3.2.3.2	Linearized Model . . . . .	58
3.2.3.3	Analyzing the Open Loop Dynamics . . . . .	59
3.2.3.4	LQR Controller Design . . . . .	60
3.2.3.5	Analyzing the Closed Loop Dynamics . . . . .	64
3.2.3.6	Nonlinear Simulation Results . . . . .	65
3.2.4	Conclusion for the LQR based Unified Controller Design . . .	69
3.3	Unified Incremental Nonlinear Dynamic Inversion (INDI) Controller Design with Integrated Control Allocation (CA) . . . . .	70
3.3.1	Literature Review of the INDI and CA Methods . . . . .	71
3.3.2	The Unified INDI+CA Controller Design . . . . .	74
3.3.2.1	Definition of the Control Inputs . . . . .	75
3.3.2.2	Formulation of the INDI Control Law . . . . .	78
3.3.2.3	Filtering Sensor Noise & Data Synchronization . . . . .	82
3.3.2.4	Linear Controller: Required State Derivatives . . . . .	83
3.3.2.5	Command Generator . . . . .	85
3.3.2.6	Overall INDI Controller Structure . . . . .	86
3.3.2.7	Control Allocation Design & Integration into the INDI controller . . . . .	88
3.3.3	Nonlinear Simulation Results . . . . .	93
3.3.3.1	Vertical Take-off, Hover & Low Speed Flight . . . . .	95
3.3.3.2	Transition From Hover to Cruise Flight . . . . .	99
3.3.3.3	Importance of the CA: Hover to Cruise Transition with- out the CA . . . . .	105

3.3.3.4	Climb/Descent & Coordinated Turn at Cruise . . . . .	107
3.3.3.5	Transition from Cruise Flight to Hover & Vertical Land- ing . . . . .	110
3.3.3.6	Importance of the CA: Disturbance Rejection with and without the CA . . . . .	113
3.3.3.7	Inherent Robustness to the Modeling Errors: Error in Drag Coefficient . . . . .	117
3.3.3.8	Robustness to the Model Dependent Parameters: Error in Roll and Yaw Moment of Inertia and Mass . . . . .	120
4	CONCLUSION AND FUTURE WORKS . . . . .	127
	REFERENCES . . . . .	131
	APPENDICES	
A	ACTIVE SET ALGORITHM USED TO SOLVE THE CA PROBLEM . . .	141
	CURRICULUM VITAE . . . . .	143

## LIST OF TABLES

### TABLES

Table 1.1 Funds Raised by Fast-growing eVTOL Companies, data taken from [3]. . . . .	2
Table 2.1 Digital DATCOM Parameter Definitions . . . . .	22
Table 2.2 Digital DATCOM Input File . . . . .	23
Table 2.3 Parameters of the Schübeler HST-215 EDF. . . . .	33
Table 2.4 EDF sets definitions and parameters . . . . .	36
Table 2.5 Parameters of the thrust/rpm and the tilt angle actuator dynamics (note that relation between the thrust and rpm is defined in Equation (2.12)).	39
Table 2.6 Parameters of the MEMS IMU sensor model . . . . .	40
Table 2.7 General parameters of the air-taxi . . . . .	43
Table 3.1 Normalization factors used for the tuning of $Q$ and $R$ Matrices. . . . .	62
Table 3.2 Linear controller gains. . . . .	85
Table 3.3 Linear controller gains for the navigation commands. . . . .	85

## LIST OF FIGURES

### FIGURES

Figure 1.1	Lilium-jet eVTOL air-taxi [10], figure taken from [7]. . . . .	10
Figure 2.1	Forward flight aerodynamic modeling, static coefficients. . . . .	21
Figure 2.2	Forward flight aerodynamic modeling, dynamic force coefficients. . . . .	24
Figure 2.3	Forward flight aerodynamic modeling, dynamic moment coefficients. . . . .	24
Figure 2.4	Forward flight aerodynamic modeling, Lift to Drag ratio (L/D). . . . .	25
Figure 2.5	Schübeler HST-215 Electric Ducted Fan (EDF), data taken from [13]. . . . .	32
Figure 2.6	Schübeler HST-215 Electric Ducted Fan Thrust coefficient ( $C_T$ ) Estimation. . . . .	33
Figure 2.7	Efficiency values of Schübeler EDF . . . . .	34
Figure 2.8	Top view of the aircraft showing EDF sets and their distribution. . . . .	36
Figure 2.9	Block diagram of the actuator dynamics model. . . . .	40
Figure 3.1	Reduced size control inputs for the LQR cruise controller design, top view. . . . .	52
Figure 3.2	Eigenvalues of the open loop system linearized at cruise trim condition. . . . .	60
Figure 3.3	Eigenvalues of the closed loop system for cruise condition. . . . .	65



Figure 3.4	Tracking performance of the LQR cruise controller for climb and descent maneuvers at cruise, state response. . . . .	66
Figure 3.5	Tracking performance of the LQR cruise controller for climb and descent maneuvers at cruise, control inputs. . . . .	66
Figure 3.6	Tracking performance of the LQR cruise controller for coordinated turn maneuvers at cruise, state response. . . . .	67
Figure 3.7	Tracking performance of the LQR cruise controller for coordinated turn maneuvers at cruise, control inputs. . . . .	68
Figure 3.8	LQR cruise controller performance away from the cruise design/trim condition (18 m/s away from the cruise trim airspeed), state response. . . . .	69
Figure 3.9	LQR cruise controller performance away from the cruise design/trim condition (18 m/s away from the cruise trim airspeed), control inputs. . . . .	70
Figure 3.10	Thrust vectoring and control input visualization for the INDI controller, side-view of the aircraft. . . . .	77
Figure 3.11	Combination of EDF sets to 4 sections: front left( <i>fl</i> ), front right( <i>fr</i> ), wing left( <i>wl</i> ) and wing right( <i>wr</i> ) for the INDI controller design, top-view. . . . .	78
Figure 3.12	High level block diagram of the INDI controller with integrated CA. . . . .	88
Figure 3.13	Hover & low speed flight test results, state response. . . . .	95
Figure 3.14	Hover & low speed flight test results, required and obtained state derivatives. . . . .	96
Figure 3.15	Hover & low speed flight test results, actuator states. . . . .	98
Figure 3.16	Hover to cruise transition test results, states. . . . .	101

Figure 3.17	Hover to cruise transition test results, required and obtained state derivatives. . . . .	102
Figure 3.18	Hover to cruise transition test results, actuator states. . . . .	103
Figure 3.19	Hover to cruise transition test results without the Control Allocation, states. . . . .	105
Figure 3.20	Hover to cruise transition test results without the Control Allocation, required and obtained state derivatives. . . . .	106
Figure 3.21	Hover to cruise transition test results without the Control Allocation, actuator states. . . . .	107
Figure 3.22	Climb/Descent & Coordinated turn at cruise, states. . . . .	108
Figure 3.23	Climb/Descent & Coordinated turn at cruise, required and obtained state derivatives. . . . .	109
Figure 3.24	Climb/Descent & Coordinated turn at cruise, actuator states. . . . .	110
Figure 3.25	Transition from Cruise Flight to Hover & Vertical Landing, states. . . . .	111
Figure 3.26	Transition from Cruise Flight to Hover & Vertical Landing, required and obtained state derivatives. . . . .	112
Figure 3.27	Transition from Cruise Flight to Hover & Vertical Landing, actuator states. . . . .	113
Figure 3.28	Roll moment disturbance rejection characteristics at hover with and without Control Allocation, states. . . . .	114
Figure 3.29	Roll moment disturbance rejection characteristics at hover with and without Control Allocation, actuator dynamics. . . . .	115
Figure 3.30	Roll moment disturbance rejection characteristics at hover with and without Control Allocation, the CA trade-off between roll moment disturbance rejection and altitude command tracking. . . . .	116
Figure 3.31	Inherent robustness to error in drag coefficient. . . . .	118

Figure 3.32	Inherent robustness to error in drag coefficient, actuator states. . .	119
Figure 3.33	Robustness to error in roll moment of inertia, states. . . . .	121
Figure 3.34	Robustness to error in roll moment of inertia, actuator states. . .	122
Figure 3.35	Robustness to error in yaw moment of inertia, states. . . . .	123
Figure 3.36	Robustness to error in yaw moment of inertia, actuator states. . .	124
Figure 3.37	Robustness to error in mass, states. . . . .	125
Figure 3.38	Robustness to error in mass, actuator states. . . . .	126

## LIST OF ABBREVIATIONS

$\phi, \theta, \psi$	Aircraft Roll, Pitch and Yaw Euler Angles
$p, q, r$	Aircraft body angular velocities
$u, v, w$	Aircraft body translational velocities
$p_n$	Aircraft position in North
$p_e$	Aircraft position in East
$h$	Altitude
$M$	Mach number
$V_{inf}$	Airspeed
$\alpha$	Angle of attack
$\beta$	Angle of sideslip
$\gamma$	Flight path angle
$\bar{q}$	Dynamic pressure
$S$	Wing reference area
$\bar{c}$	Mean aerodynamic chord
$b_{ref}$	Wing span
$l_{fus}$	Fuselage length
$h_{fus}$	Fuselage mean height
$C_T$	Electric Ducted Fan (EDF) Thrust coefficient
$C_Q$	Electric Ducted Fan (EDF) Torque coefficient
$m$	Maximum takeoff mass
$W_{MTOW}$	Maximum takeoff weight
$J$	Inertia matrix
$I_x$	Inertia in the aircraft body-x direction
$I_y$	Inertia in the aircraft body-y direction

$I_z$	Inertia in the aircraft body-z direction
$F_{aero}^b$	Aerodynamic forces in the aircraft body axis
$F_{prop}^b$	Propulsion forces in the aircraft body axis
$F_{grav}^b$	Gravitational forces in the aircraft body axis
$F_{dist}^b$	Disturbance forces in the aircraft body axis
$M_{aero}^b$	Aerodynamic moments in the aircraft body axis
$M_{prop}^b$	Propulsion moments in the aircraft body axis
$M_{dist}^b$	Disturbance moments in the aircraft body axis
$F_{edf}^b$	Force generated by the EDF in the aircraft body axis
$M_{edf}^b$	Moment generated by the EDF in the aircraft body axis
$F_{edf}^m$	Force generated by the EDF in the EDF body axis
$M_{edf}^m$	Moment generated by the EDF in the EDF body axis
$L_{prop}$	Roll moment generated by the propulsion system in the aircraft body axis
$M_{prop}$	Pitch moment generated by the propulsion system in the aircraft body axis
$N_{prop}$	Yaw moment generated by the propulsion system in the aircraft body axis
$F_{x_{prop}}$	Force generated by the propulsion system in the aircraft body x-axis
$F_{y_{prop}}$	Force generated by the propulsion system in the aircraft body y-axis
$F_{z_{prop}}$	Force generated by the propulsion system in the aircraft body z-axis
$\delta$	EDF tilt angle
$rpm$	EDF rpm (revolutions per minute)
$T$	EDF Thrust
$Q$	EDF Torque

$fl$	Front-left EDF section
$fr$	Front-right EDF section
$wl$	Wing-left EDF section
$wr$	Wing-right EDF section
$\Delta x$	EDF x-lever arm in the aircraft body axis
$\Delta y$	EDF y-lever arm in the aircraft body axis
$\Delta z$	EDF z-lever arm in the aircraft body axis
$\sigma$	EDF turn direction
$T_{cmd}$	Thrust commanded by the controller
$\delta_{cmd}$	Tilt angle commanded by the controller
$T_{act}$	Thrust generated by the actuators/EDF considering actuator dynamics
$\delta_{act}$	Tilt angle generated by the actuators/EDF considering actuator dynamics
$\omega_{n_T}$	Natural frequency of the thrust actuator dynamics
$\zeta_T$	Damping coefficient of the thrust actuator dynamics
$\omega_{n_\delta}$	Natural frequency of the tilt angle actuator dynamics
$\zeta_\delta$	Damping coefficient of the tilt angle actuator dynamics
$U$	Control input vector
$x$	State vector
$U_{trim}$	Control input vector at trim condition
$x_{trim}$	State vector at trim condition
$A$	State matrix of the linearized state space representation
$B$	Input matrix of the linearized state space representation
$C$	Output matrix of the linearized state space representation
$U_{lb}$	Lower bound of the control input vector
$U_{ub}$	Upper bound of the control input vector
$U_0$	Initial conditions for the control input vector

$x_d$	Desired state vector/trajectory
$K$	LQR Controller gain
$Q$	LQR Controller state weight matrix
$R$	LQR Controller input weight matrix
$U_{INDI}$	INDI control input vector
$U_{INDI,0}$	INDI control input vector at the previous time step
$\Delta U_{INDI}$	Incremental INDI control input vector
$v_{INDI}$	Virtual INDI control input vector
$\Delta v_{INDI}$	Incremental virtual INDI control input vector
$T_{v,INDI}$	Transformation matrix between the virtual and INDI control input vectors
$\dot{x}_0$	INDI controller's state derivative estimation via sensor measurements
$\dot{x}_{req}$	INDI controller's required state derivatives
$T_x$	Component of thrust in the aircraft body x-axis
$T_z$	Component of thrust in the aircraft body z-axis
$U_{act}$	Actuator states of the INDI controller considering the actuator dynamics
$g$	INDI controller's virtual control input matrix
$H_f$	INDI controller noise filter
$\omega_{n_f}$	Natural frequency of the INDI controller's noise filter
$\zeta_f$	Damping coefficient of the INDI controller's noise filter
$\Delta U_{CA}$	Incremental control input generated by the Control Allocation (CA) algorithm
$W_v$	State weight matrix of the CA algorithm
$W_u$	Control input weight matrix of the CA algorithm
$\Delta U_{des}$	Desired control input increment of the CA algorithm
$\gamma$	Tuning coefficient of the CA algorithm





## CHAPTER 1

### INTRODUCTION

In recent years, on-demand Urban Air Mobility (UAM) has been a popular topic in aviation, and it emerged as an alternative option for urban mobility currently based on ground transportation [46, 51, 68]. With the increasing number of commuters in crowded cities, traffic congestion causes longer travel times and increased gas emissions harming the environment significantly [68]. Therefore, fast transportation, sustainability (i.e., very low carbon emissions), and efficiency are critical motivational points for the on-demand UAM [46]. There are additional environmental requirements (such as low noise level) of UAM since operations are performed very close to highly populated areas/city centers. In a survey study about the on-demand UAM, one of the main challenges is defined as achieving very low noise levels considering the strict certification requirements of flying at urban areas [46].

Electric propulsion comes with significant advantages compared to conventional propulsion systems (i.e., reciprocating/piston engines or turbine engines) considering the noise, carbon emission, and efficiency needs of UAM [46, 62]. On the other hand, electric propulsion has drawbacks compared to conventional propulsion systems, mainly due to the limited energy capacity of the current battery technology [42, 64]. Nevertheless, with the introduction of electric propulsion in recent years, a new aircraft concept called "air-taxi" emerged as a feasible solution for on-demand UAM [46, 68]. Vertical Takeoff and Landing (VTOL) is a very crucial ability for the air-taxi concept. Air-taxis combining VTOL with electric propulsion are named as "electric Vertical Takeoff and Landing (eVTOL)" in literature [68]. In recent years, many companies and research institutes focus on designing eVTOL air-taxis, and it is possible to see this concept as an alternative urban transportation option in the near future

[51, 68, 46].

eVTOL air-taxi is a relatively new concept, and there are many unique eVTOL projects [68] considering different business requirements (e.g., short-range 1-2 person inner-city transportation, mid-range 4-5 person regional transportation, etc.) Most of these projects are still ongoing, and the race to build feasible eVTOL air-taxi seems to be quite motivational for both small and big companies. Market share of air-taxi is expected to grow very fast [27, 46, 62]. Many startup companies have already received significant amount of investments to design, build and certify eVTOL air-taxis [68]. Total funds raised by some of the fast-growing companies focusing on eVTOL aircraft design are given in Table 1.1. eVTOL air-taxi concept is mentioned briefly to give an introduction about the motivation of the thesis. Details of different eVTOL air-taxi concepts will be discussed in the following sections.

Table 1.1: Funds Raised by Fast-growing eVTOL Companies, data taken from [3].

Company	Founded	Total Funds Raised	Lead Investor
Joby Aviation	2009	\$ 796 Million	Toyota Motor
Lilium GmbH	2015	\$ 376.4 Million	Tencent
Volocopter GmbH	2011	\$ 369.2 Million	Unknown
Ehang	2014	\$ 92 Million	Unknown

A novel fixed-wing eVTOL air-taxi is studied in this thesis. The air-taxi is fully electric and equipped with numerous small tilting Electric Ducted Fans (EDFs) distributed over the aircraft. VTOL ability is combined with efficient high-speed forward flight/cruise thanks to the fixed-wing aerodynamic surface. The transition between vertical and forward flight is achieved by pure thrust vector control of tilting EDFs. Aircraft does not have any conventional stability and control surfaces (e.g., elevator, aileron, rudder, vertical/horizontal tail, etc.). Full envelope flight control mainly consisting of the low-speed vertical flight, transition flight, and high-speed forward flight is achieved by adjusting the thrust vector of EDFs distributed through the aircraft's front and wing sections. The main focus of the thesis is defining problems/challenges regarding the full envelope flight control and designing an effective unified flight

controller for the unique eVTOL aircraft that is not studied before to the best of the author's knowledge.

## **1.1 eVTOL Air-Taxi Concepts with Distributed Electric Propulsion (DEP)**

Electric propulsion has quite different characteristics compared to the traditional propulsion systems (i.e., the reciprocating/piston engines or turbine engines) [61, 49]. One of the critical advantages of electric propulsion is the scale-free design feature [61]. Thanks to the design flexibility, it is possible to distribute numerous electric propulsion units over the airframe considering specific design purposes [42]. The emerging concept of Distributed Electric Propulsion (DEP) comes with key advantageous features especially considering the goals of on-demand UAM [61, 49, 42, 29]. On the other hand, electric propulsion systems have drawbacks mainly due to the limited energy density of current battery technology [61, 42]. Both pros and cons of the DEP concept will be explained in this section, considering the needs of on-demand UAM.

### **1.1.1 Pros and cons of DEP Considering the Requirements of on-demand UAM**

VTOL air taxis should be easily accessible by passengers since fast transportation is one of the main motivations of UAM [46]. Therefore, VTOL air-taxis need to take off and land in or near city centers (i.e., densely populated areas). Moreover, air-taxi transportation will be more efficient if operations are performed at low altitudes (climbing high altitudes requires significant amount of energy and limits the range/endurance). Considering these points, VTOL air-taxis must have very low aircraft noise since even a small fleet of air-taxis could cause significant noise disturbance to the community. In a very detailed feasibility study about urban air transportation [46], it is noted that current helicopters are too noisy to satisfy the noise objectives of on-demand UAM. Many studies show that DEP aircraft produce much less noise compared to aircraft with conventional propulsion systems [49, 46, 41]. Therefore, with proper design and integration of DEP into the air-taxis, noise requirements of urban air transportation can be achieved [46, 49].

Another critical environmental objective of the on-demand UAM is energy sustain-

ability (i.e., decreasing the carbon footprint of air vehicles) [46]. Electric propulsion produces zero carbon emission, which is quite beneficial for urban air transportation [61, 49]. The generation of electricity mainly depends on the combustion of fossil fuels that might have a high carbon footprint [15, 21]. However, the source of electric energy is not considered since it is not directly related to the aircraft's carbon footprint. It is noted that low carbon footprint sources such as wind and solar energy can be used to generate electricity [15]. To conclude, DEP technology will be considerably more environmentally friendly than traditional propulsion systems [49].

Overall performance comparison of aircraft with electric and conventional propulsion systems is not straightforward, and using the same metrics might lead to misconceptions. [62]. Regarding propulsive efficiency, electric motors are significantly better than conventional propulsion systems [49, 62]. Electric propulsion's efficiency can reach values higher than 90 % [18]. On the other hand, for a complete performance comparison considering the overall system integration, battery weight of electric propulsion systems is also relevant since the main burden of electric propulsion is the limited energy densities of batteries [42]. The battery energy density will be discussed at the end of this section in detail.

To sum up, electric propulsion is advantageous considering that very high propulsive efficiency is possible to achieve, and the performance analysis of the overall system should be performed taking into account the integrated systems instead of the propulsion systems only [62]. A more detailed discussion about the performance and efficiency comparisons between electric and traditional propulsion systems can be found in literature [49, 62, 66, 41].

The DEP concept has inherent robustness to system failures thanks to the increased redundancy [42]. With the proper distribution of electric propulsion units and the supplying power system/batteries, propulsion system failures can be handled without catastrophic results [49, 46]. Considering the certification of eVTOL air-taxis in case of failure conditions, increased robustness to propulsion system failures is a critical advantage of the DEP eVTOL concept [46]. On the other hand, most DEP aircraft are over-actuated systems (i.e., the number of control effectors/actuators is higher than the number of control axes/channels). For the over-actuated systems, decoupling of

actuators and control channels is not straightforward in the flight controller design [63]. The need to decouple actuators and control axes emerges in case of limited control authority (i.e., the saturation of actuators). The actuator saturation problem must be properly resolved to avoid instability due to unrealistic (i.e., physically not achievable) solution [63]. This is one of the fundamental challenges of the unified flight controller design for an eVTOL air-taxi with DEP concept and will be discussed throughout the thesis in detail (see Section 3.1).

The main advantages of the DEP are explained considering the goals of on-demand UAM. There are also drawbacks of electric propulsion systems that complicate the design of eVTOL air-taxis. The main disadvantage of the DEP concept is the energy storage weight/cost due to the limited energy density of the battery technology [42, 62]. Based on a study conducted by NASA in 2016, the current energy density of batteries is around 250 Whr/kg [61]. The same study also states that rate of improvement in the energy density is around 8 % per year over the past 30 years, and 400 Whr/kg is expected by 2025. Although the current battery technology is a limiting factor for the electric aircraft in general, the energy and power densities are sufficient for the low payload (2-3 person) and short-range (200-300 km) eVTOL air-taxi concept [62]. Feasibility studies show that with an energy density of 250 Whr/kg, a maximum range of 300 km can be reached with a Maximum Takeoff Weight (MTOW) of 3000 kg [51, 24, 87]. On the industry side, many promising eVTOL air-taxi projects have already received significant amount of investments [46, 68] (see Table 1.1). Most of these projects focus on low payload and short-range eVTOL air-taxis, which is consistent with the theoretical limits of the current battery technology.

Another design challenge for the DEP air-taxi concept is related to safety considerations since the propulsion system entirely depends on high-power electric devices [49]. Proper design solutions are needed to safely integrate the DEP system considering the problems such as battery failure conditions-thermal runaway, distribution of power to electric motors, etc. [49, 42].

To sum up, the eVTOL air-taxi concept with DEP technology has critical advantageous features such as low noise, zero carbon emission, high efficiency, increased

robustness to failures thanks to actuator redundancy, scale-free design, etc. Therefore, the concept has a great potential to meet the targets of the on-demand UAM. The critical sizing factor is the limited energy/power density of the current battery technology. However, studies and ongoing projects show that the current battery technology is already mature enough for small-sized eVTOL air-taxi concepts. Moreover, the expected improvement is promising for larger payload and higher range eVTOL air-taxis [61, 51, 24, 87, 46, 68].

This section summarizes the pros and cons of DEP technology considering the requirements/goals of on-demand UAM. More detailed studies about the DEP technology and its integration into the future aircraft concepts can be found in literature [49, 42, 29] In the next section, DEP eVTOL air-taxi concepts and the unique air-taxi studied in this thesis will be discussed.

### **1.1.2 DEP eVTOL Air-taxi Concepts**

On-demand UAM market expected to grow exponentially in the following years [46, 52]. Therefore, many companies are highly motivated to design eVTOL air-taxis that can be a feasible solution for the on-demand UAM problem. Most of these companies/projects use DEP technology thanks to the advantageous features of the DEP concept. For the purpose of this study, DEP eVTOL air-taxi concepts will be classified based on the operational/market needs (mainly flight range and endurance).

Most of the ongoing and promising DEP eVTOL air-taxi projects can be divided into two groups. The first group focuses on inner-city air transportation with a very short range (e.g., 50-100 km) and endurance. Short-range eVTOL projects in general use several stationary electric propulsion units in multi-copter configuration. DEP provides lift for both hover and higher speed forward flight. Since these type of air-taxis do not have any high-lift aerodynamic surfaces such as fixed wings, the range and endurance are constrained due to the limited energy density of the current battery technology. Without a wing surface, high-speed aerodynamically efficient flight can not be achieved. Therefore, these air-taxi projects have limited ranges and only feasible for inner-city urban air transportation. Some of the most promising short range multi-copter type eVTOL air-taxi projects are Volocopter and Ehang AAV [14, 6].

The second group of DEP eVTOL projects combines electric propulsion with high-lift surfaces (i.e., mainly wings and canards). In hover flight, all of the required lift comes from the propulsion system. On the other hand, in high-speed forward flight, the wing surface generates most of the lift (with an efficient design-high L/D ratio), and the propulsion system only generates the required thrust to overcome the drag. This configuration significantly increases the range (up to 200-300 km) such that regional air transportation between cities becomes feasible. The drawback of this configuration is the increased complexity in the aircraft design since transition dynamics between the hover and forward flight is quite complicated (i.e., modeling & control are quite challenging). The transition is in general achieved via tilting the electric propulsion units which might cause flow separation, significant aero-propulsion couplings, and other aerodynamic phenomena that are hard to deal with. Some configurations use independent electric propulsion units that provide pure thrust for vertical lift and forward flight. In this configuration, problems related to the tilting of propulsion system are avoided since all propulsion units are stationary. On the other hand, the aircraft's weight increases considerably since most of the electric propulsion units (i.e., the ones that provide pure vertical lift for hover flight) are useless in forward flight. Considering these points, many companies are focusing on designing long-range air-taxis with the transitioning DEP concept. Some of the popular ones are Lilium GmbH, Joby Aviation, Kittyhawk, and Airbus Vahana [10, 8, 9, 1].

To sum up, DEP eVTOL air-taxi concepts are discussed in this section considering a classification based on the range/endurance. Multi-copter type eVTOLs have short ranges due to the lack of an efficient high lift aerodynamic surface. The propulsion system provides both the required lift and thrust for the forward flight. Therefore, the range/endurance is significantly constrained by the limited energy density of the current battery technology. The longer-range DEP eVTOL concepts use a high-lift aerodynamic surface (i.e., the wing) to generate efficient lift in high speed forward flight similar to the conventional aircraft configuration. In this concept, propulsion systems tilt to perform the transition between hover and forward flight. The main disadvantage or challenge is the increased complexity that emerged in transition dynamics. There is also an alternative configuration that uses separate propulsion systems for hover and forward flight. The transition dynamics are not complex since there are

no tilting propulsion systems in this configuration. However, this configuration lack efficiency since the propulsion system used for VTOL is useless in forward flight. In the industry side, most of the promising long-range eVTOL projects use tilting propulsion units which support the tilting propulsion concept. A brief introduction of the DEP eVTOL aircraft concepts are discussed considering the promising eVTOL projects in the industry. A more detailed review of various VTOL concepts can be found in literature [39].

### **1.1.2.1 Long Range DEP eVTOL Air-taxi Concepts**

In the previous section, the most common DEP eVTOL air-taxi concepts are briefly introduced. A more detailed discussion will be provided in this section regarding the long-range/endurance DEP eVTOL air-taxis with a high-lift aerodynamic surface (i.e., the wing). There are mainly three configurations named "tilt-rotor", "tilt-wing" and "fixed-wing multicopter" considered for the purpose of this thesis.

The term "tilt-rotor" is, in general, used to define that the transition is achieved via tilting the propulsion units (e.g., rotors, propellers, ducted fans, etc.). Detailed comparison of different tilt-rotor concepts (e.g., tilt-rotor, tilt-duct/nacelle, tilt-prop, etc.) are not introduced in this thesis since the aim is to differentiate "tilt-rotor" and "tilt-wing" concepts. The reader can refer to the review paper [39] for a more detailed comparison between various VTOL configurations. It is noted that the tilt-rotor is the most popular long-range VTOL concept, and most of the promising long-range DEP eVTOL projects use tilt-rotor configuration [10, 8, 9].

For the "tilt-wing" configuration, the entire wing is tilted to perform the transition between hover and forward flight. This configuration is not very popular in the industry for the long-range eVTOL air-taxi concept. However, there are some tilt-wing eVTOL projects held by NASA and Airbus [1, 11]. For the tilt-wing configuration, a very high angle of attack might occur during the transition between hover and forward flight. Therefore, avoiding stall behavior during the transition is quite challenging for the tilt-wing configuration [39].

The "fixed-wing multicopter" concept uses independent propulsion systems for ver-



tical/hover and forward flight. The transition from hover to forward flight is simply performed without tilting any propulsion system. The aircraft design is less complex than the "tilt-rotor" and "tilt-wing" concepts since undesired aerodynamic effects are not present thanks to the decoupling of propulsion systems. The propulsion system used for vertical flight is not used in forward flight and adds an additional weight burden to aircraft design. The range/endurance is more constrained compared to the "tilt-wing" and "tilt-rotor" concepts due to less efficient forward flight and additional weight burden. Therefore, hybrid propulsion systems are preferred for this configuration instead of all-electric aircraft [38]. In the industry, fixed-wing multicopter configuration is not very common for the DEP eVTOL air-taxi concept. A known example for the "fixed-wing multicopter" eVTOL is the Personal Air Vehicle (PAV) designed by Aurora Flight Sciences supported by Boeing Company [2].

## 1.2 Motivation and Contributions of the Thesis

In previous sections, DEP eVTOL air-taxi concepts are introduced, and most common configurations are discussed thoroughly. The air-taxi studied in this thesis is a novel DEP eVTOL with tilt-rotor configuration. Several tilting electric ducted fans (EDFs) are distributed over the fixed-wing and canard/front surfaces, and traditional control and stability surfaces do not exist. Therefore, the aircraft configuration is unique compared to the other tilt-rotor eVTOL air-taxi concepts. The aircraft studied in this thesis is inspired by the Lilium-jet, which is one of the most promising and fast-growing eVTOL air-taxi projects [10]. Lilium is planning to be in service around 2025, and the company has already received a significant amount of investment (\$ 376 Million, see Table 1.1). General information about the "Lilium-jet" and top-side views of the aircraft is given in Figure 1.1. Moreover, top and side views of the aircraft designed in this thesis for the purpose of modeling and control study are given in Figures 2.8 and 3.10. *It is important to note that the aircraft designed and studied in this thesis is different from the Lilium-jet, and all the results and conclusions of the thesis are not related to the Lilium-jet.*

*The thesis focuses on the full envelope flight controller design for the novel air-taxi that is not studied before to the best of the author's knowledge.* A preliminary flight

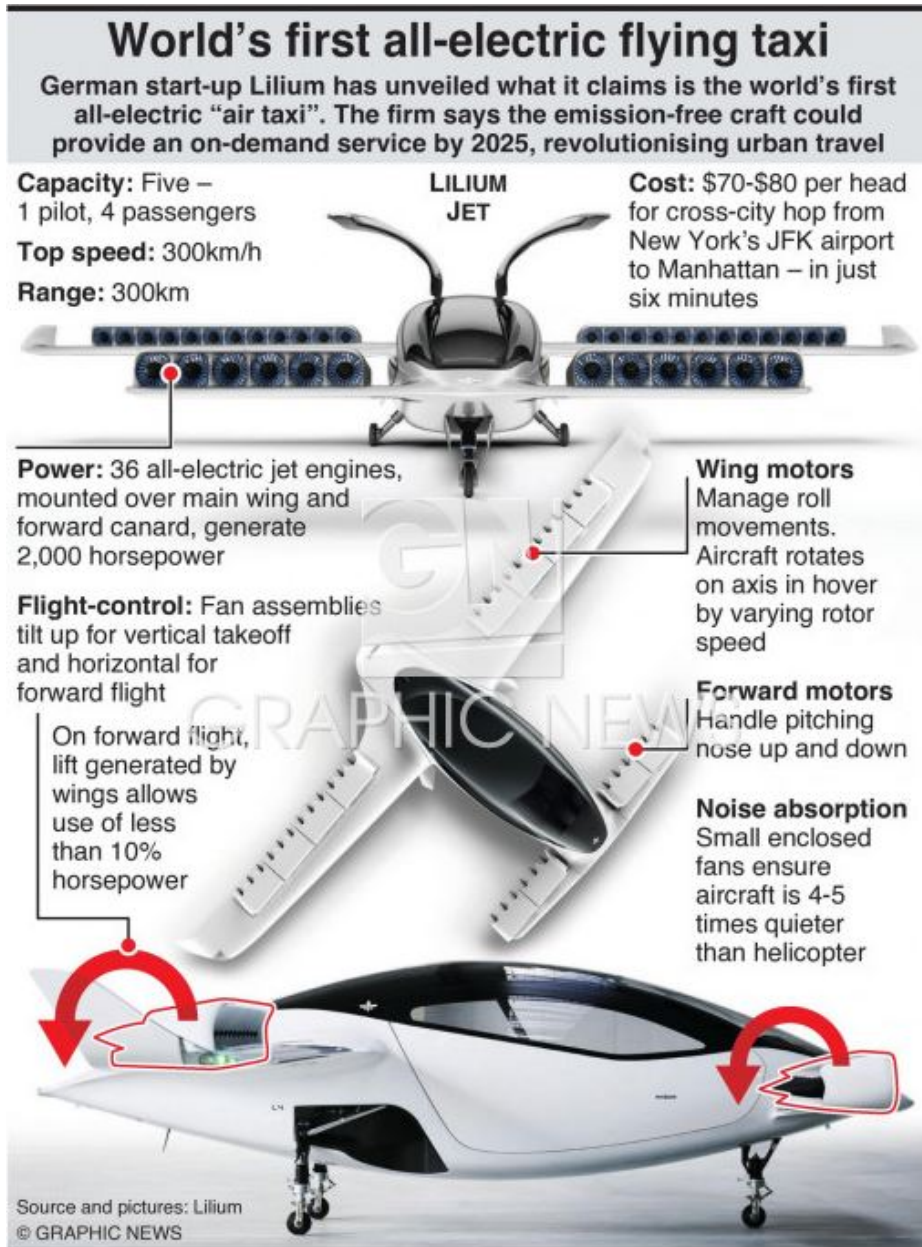


Figure 1.1: Lilium-jet eVTOL air-taxi [10], figure taken from [7].

dynamics model of the air-taxi is generated first since there is no data available to be used in the literature.

The studied air-taxi concept can be classified as long-range DEP eVTOL considering the introduction given in the previous sections. It has a fixed-wing surface for efficient high-speed forward flight and tilting EDFs to transition between hover and forward flight via pure thrust vector control. EDFs are distributed over the front/-

canard and wing of the aircraft. Wing EDFs are located at the trailing edge of the wing surface, similar to a flap configuration. Aircraft do not have any conventional stability and control surfaces such as aileron, elevator, rudder, horizontal/vertical stabilizer, etc. (see Figure 2.8). Full envelope flight control is achieved via adjusting the thrust vector of numerous EDF units properly. *Not having conventional control/stability surfaces has critical advantages: improved aerodynamic efficiency at high speed forward flight, design flexibility-simplicity, better sizing-weight savings, etc. On the other hand, it also comes with problems/challenges regarding the flight control such as open-loop directional instability, limited control authority at specific flight conditions, resolving actuator saturation is not straightforward due to the thrust vector couplings, etc., see Section 3.1 for details.*

*Long-range DEP eVTOL aircraft is an emerging concept and became popular in the aviation industry [9, 10, 8] as part of the future electric aircraft concept, which is seen as a feasible solution for the on-demand UAM [46, 62, 87, 29, 51]. However, there are very few studies in the literature regarding the modeling and full envelope flight controller design of long-range DEP eVTOL aircraft with a fixed-wing aerodynamic surface. Two studies are found in literature similar to the aircraft concept considered in this thesis. A novel fixed-wing tilt-rotor eVTOL is studied in the first paper [33]. The authors focus on both flight dynamics modeling and full envelope flight control of the novel concept. In the second study, the authors put more effort into designing a unified flight controller for a fixed-wing multi-copter type eVTOL aircraft for the entire flight envelope [55]. In both studies, the aircraft has conventional stability/control surfaces which improve stability and control characteristics. The aircraft studied in this thesis differentiates from both long range DEP eVTOL concepts since there are no conventional stability and control surfaces. Pros and cons of this unique design are briefly explained in the previous paragraph and will be discussed thoroughly in Section 3.1 focusing on the flight control problems.*

**MOTIVATION:** To sum up, the motivation of the thesis is defining flight control-related problems/challenges of the unique and promising eVTOL air-taxi and designing a unified flight controller for the entire flight envelope. Taking into account the air-taxi operation, the flight envelope mainly consists of; vertical takeoff, the transition from hover to forward flight, forward flight (with climb/descent and turns),

transition from forward to hover flight, and vertical landing.

**CONTRIBUTIONS:** Contributions of the thesis are discussed comprehensively in Section 3.1 since they are all related to resolving the full envelope flight control problems of the aircraft. In this introduction, a brief description is given as follows considering the main problems and the proposed solution methods regarding the unified flight controller design:

- *Significant nonlinearities and couplings emerge in flight dynamics, especially during the transition between hover and forward flight. A nonlinear controller approach Incremental Nonlinear Dynamic Inversion is adapted to the problem to design a unified and effective flight controller. INDI method is based on nonlinear dynamic inversion (NDI), but it has different characteristics compared to the classical NDI approaches [80, 65]. The main advantage of INDI is the reduced modeling dependency and improved robustness to disturbances compared to NDI since INDI performs a sensor-based dynamic inversion [80, 74, 55, 96]. INDI became a popular and promising nonlinear control approach in recent years with improvements in sensor technology [80, 78, 89, 43, 99, 37, 55]. The INDI method fits well to the problem since flight dynamics modeling of the studied aircraft is quite complex, and significant effort is required to generate a high-fidelity model to be used in the nonlinear dynamic inversion. Thanks to the sensor-based dynamic inversion, the model dependency of the designed INDI controller is only mass, inertia, and EDF lever-arm (mainly depending on the geometry) information (see Section 3.3.2.2 for details). In this thesis, the INDI controller is formulated to design a unified flight controller that covers the entire flight envelope. The INDI controller is designed considering the strong couplings of pure thrust vector control of the unique air-taxi concept. The same design approach can be adapted to other aircraft concepts with modifications.*

- *As mentioned previously, aircraft do not have conventional stability/control surfaces, and the pure thrust vector is used to control the aircraft. Rpm and tilt angle of numerous EDF units (total of 26 EDFs) are adjusted to achieve desired thrust vector. Therefore, the system is over-actuated since the number of control axis/channels is less than the number of control effectors/actuators (i.e., 6 axis to control and 52 control inputs). The number of control inputs is reduced via applying the same*

*control inputs (i.e., rpm and tilt angle) for adjacent EDF units to simplify the controller design. Nevertheless, the system is still over-actuated, and the control allocation problem does not have a unique solution due to the over-actuation [45]. In case of limited control authority (i.e., the actuator saturation), the controller may not track the commands in all channels, and allocation of the available control authority properly becomes a critical problem [77, 63]. This problem is generally referred as "Control Allocation(CA)", and as a general solution in literature, rotational channels are prioritized over translational channels in case of actuator saturation [35, 77]. In this way, the stability of the aircraft is guaranteed via proper CA design. To design CA effectively, the relation between control channels and control effectors needs to be formulated. For the studied aircraft concept, formulating this relation is not straightforward due to the strong couplings caused by the pure thrust vector control concept. Therefore, standard saturation resolving approaches (e.g., anti-wind methods) are not easily implemented, and a specific formulation is required to decouple the thrust vector control. For traditional aircraft, it is easy to decouple control axis and control effectors since conventional control surfaces are inherently decoupled (i.e., aileron to roll axis, elevator to pitch axis, rudder to yaw axis) [47]. To sum up, not having conventional control surfaces and coupled nature of the pure thrust vector control complicate resolving the problems due to limited control authority (i.e., the actuator saturation). An optimization-based CA is designed and integrated into the INDI controller to effectively allocate the limited control authority and guarantee stable flight. Simulation results show that the CA has a vital role in satisfying stable flight in case of severe actuator saturation (see Section 3.3.3.6).*

The motivation and contributions of the thesis are explained briefly in this introductory section. The challenges of the unified flight controller design and proposed solutions/contributions are discussed thoroughly in Chapter 3.

### **1.3 Organization and Overview of the Chapters**

In this section, organization of the thesis chapters and their content are mentioned briefly to give the reader a general overview about the thesis structure and each chapter.

The thesis focuses on designing a unified flight controller for the novel eVTOL air-taxi, considering the entire flight envelope. The flight dynamics model of the air-taxi is not available in the literature. High fidelity modeling requires significant effort since generating a flight dynamics model covering the entire flight envelope is a quite complex task. For the purpose of the thesis, a preliminary flight dynamics model is generated considering the main effects at hover and forward flight. Hover and forward flight dynamic models are merged via a blending coefficient to model the transition dynamics. The component build-up approach is used to estimate the overall aerodynamic and propulsion forces and moments. Sensor and actuator dynamics are included in the flight dynamics model to build a 6-Degree of Freedom (DOF) simulation model. Details of the flight dynamics modeling and simulation model are given in Chapter 2.

Once the flight dynamics model is obtained, controller design is studied in Chapter 3. First, a linear controller is designed for cruise flight to observe the open and closed-loop characteristics of the aircraft at high speed forward flight. LQR method is used to design the linear cruise controller. It is observed that the LQR controller works as expected close to the design condition (i.e., the trim condition). However, due to the severe nonlinearities/couplings in the transition dynamics, the same LQR controller can not perform well when the aircraft is away from the trim condition (i.e., approaching the transition region). Therefore, it is concluded that a gain-scheduled LQR design is necessary to have a unified flight controller that covers the entire flight envelope. A nonlinear sensor-based control method called INDI is used to effectively design a unified controller that is less dependent on the aircraft model. INDI controller is formulated specifically considering the coupled nature of the pure thrust vector control concept. Once the INDI controller is designed, several simulation tests are performed to analyze the performance of the unified INDI controller for the entire flight envelope. It is observed that the INDI controller works satisfactorily if control authority is not limited (i.e., when the actuator saturation does not exist). In case of actuator saturation, a proper allocation of the limited control authority is essential to satisfy stable flight. Resolving actuator saturation is not straightforward due to the coupled nature of the pure thrust vector control. To resolve problems due to the limited control authority, an optimization based CA block is designed and integrated

into the unified INDI controller. The overall flight controller (INDI+CA) is tested for various conditions considering the wide flight envelope, including sensitivity to modeling errors and disturbance rejection characteristics. Based on the simulation results, the performance of the unified controller is satisfactory for the entire flight envelope. Moreover, disturbance rejection characteristics and robustness to modeling errors are quite promising. To sum up, Chapter 3 is about the unified controller design and verification of the controller via nonlinear simulation results.

In the last chapter (Chapter 4), concluding remarks are given considering the motivation of the study, challenges/problems of the full envelope flight controller design, proposed design solutions and contributions, verification of the designed controller, and possible future works.





## CHAPTER 2

### FLIGHT DYNAMICS MODELING

As mentioned in the introduction part (Section 1.2), *the aircraft studied in this thesis has a novel configuration. Therefore, a 6-DOF flight dynamics model of the aircraft, which is not available in the literature, needs to be generated first.* The aircraft has a fixed-wing aerodynamic surface and numerous tilting EDFs distributed through the front/canard and wing sections of the aircraft (see Figure 2.8). The challenging part is estimating the aerodynamic and propulsion forces & moments acting on the aircraft, especially during the transition region. High fidelity modeling of the transition dynamics is quite complex since tilting EDFs also generate aerodynamic forces/moments, and flow separation over the EDF surfaces might occur during the transition. *The main focus and motivation of the thesis are the full envelope flight control of the unique eVTOL aircraft. Therefore, the flight dynamics model is constructed considering the main effects at hover and high speed forward flight. The transition dynamics are obtained via merging the hover and forward flight models based on the airspeed. Considering these points, a preliminary flight dynamics model is generated instead of a high fidelity model including the complex effects during the transition dynamics. Switching between the hover and forward flight model imposes significant nonlinearities during the transition, although the flight dynamics is not modeled with high fidelity (see Section 3.2.3.6).*

To simplify the aerodynamic and propulsion system modeling, aircraft is divided into two primary components, and contributions of each component are added (i.e., the component build-up approach) to find the overall aerodynamic and propulsion forces & moments. The first component is the aircraft wing-body, and the second component is identical EDFs used in each propulsion set. To ease the modeling effort, the

aerodynamic and propulsion models are decoupled. In other words, aero-propulsion couplings are not modeled, although they might have significant contributions to the model especially in transition regions. Modeling of the aero-propulsion couplings is quite complex for the novel air-taxi and requires significant design effort. Therefore, a high fidelity model including aero-propulsion couplings might be the topic of a dedicated study focusing on flight dynamics modeling.

Aerodynamic modeling is divided into two parts named "forward flight" and "hover". For the forward flight modeling, the aerodynamic contribution of the wing-body component is obtained using a semi-empiric software called the DATCOM [100, 70]. The hover flight aerodynamic modeling is more simple and based on a flat-plate approximation. The ground effect at hover is not modeled since it is also considered as part of the high fidelity modeling study similar to the aero-propulsion couplings at transition flight. To estimate the propulsion characteristics (thrust, torque, power) of EDFs, data-sheet of a commercially available EDF [13] is used, and the basic momentum theory is applied to verify the data [73].

In the following sections, first, the aerodynamic model is generated considering the component build-up approach. Second, the propulsion model is given in detail considering also the actuator dynamics of EDF propulsion units. Finally, the 6-DOF Equations of Motion (EOM) are defined to build the flight dynamics model.

## **2.1 Aerodynamic Modeling**

In general, one of the most challenging parts of the flight simulation is evaluating the aerodynamic and propulsion forces/moments which are highly nonlinear and depends on various parameters [22]. For specific flight conditions (e.g. stall regions, coupled aero-propulsion dynamics, hover in ground effect, etc.), these nonlinearities become more dominant and accurate modeling of the aerodynamic and propulsion effects require much more effort.

*The aircraft considered in this study performs VTOL, transition (between hover and forward flight), and other forward flight phases (cruise, climb/descent, coordinated-turn, etc.) considering the full flight envelope. The detailed aerodynamic model-*

*ing of the entire flight envelope requires significant amount of modeling work and could be part of another study dedicated to aerodynamic and propulsion modeling. Moreover, aerodynamic models covering the entire flight envelope do not exist in the literature for a similar aircraft (i.e., a fixed-wing eVTOL with distributed EDFs on wing-canard sections and without conventional control-stability surfaces). As mentioned previously, this work aims to focus on flight control of the novel eVTOL aircraft. Considering these points, the aerodynamic model covering the complete flight regime is obtained using fast and efficient approaches. Taking into account the balance between accuracy and complexity, the "DATCOM" program is chosen to model the wing-body aerodynamic effects at forward flight. The modeling of hover flight is more simple, and it is based on a flat-plate model, which is used in literature for other VTOL concepts [56]. The transition between hover and forward flight is modeled by introducing a blending coefficient. The blending coefficient is based on the forward flight velocity, which is the crucial factor to determine whether the wing-body aerodynamic contribution is dominant or not.*

The details of the preliminary aerodynamic modeling for hover, forward, and transition flight phases are given in the following sections.

### **2.1.1 Forward Flight: Wing-Body Aerodynamic Modeling**

The "United States Air Force (USAF) Stability and Control Digital DATCOM" is a computer program that estimates static stability, control, and dynamic derivative characteristics of fixed-wing aircraft using the methods contained in USAF Stability and Control DATCOM [4, 26, 70]. DATCOM has been used in literature and industry for a long time to build preliminary flight dynamics models of several aircraft and missiles [71, 40, 72, 25, 85, 16, 95]. Compared to the CFD methods, DATCOM is very fast and it generally gives accurate enough results for the preliminary design stage [71, 4, 26]. Another advantage of the DATCOM is compatibility with the "MATLAB" software that is used to build the 6-DOF simulation model of the aircraft [5]. There exist other open source programs such as AVL [30], XFLR5 [32, 57] to estimate the aerodynamic and control coefficients in a fast way. For our case, the DATCOM program is considered to be the most effective approach to generate the preliminary

aerodynamic data for the forward flight model.

### 2.1.1.1 Generating the Digital DATCOM Input File

The DATCOM program requires an input file that contains the 3-D geometry, lifting surface characteristics and desired flight conditions [100, 70]. The aircraft's body and wing geometry is constructed iteratively considering the open-source geometry of the "Lilium" aircraft as a baseline configuration [10]. Iterations are mainly performed by changing the location and geometry of the wing surface and location of the cg. (see Tables 2.1 and 2.2). It is aimed to satisfy following static stability requirements [58] and  $C_L/C_D$  ratio for the final configuration of the aircraft. *As mentioned in Section 1.2, it is important to remind that the results obtained in this thesis are specific to this study and can not be associated with the "Lilium" aircraft [10].*

1.  $C_{m\alpha} < 0 \equiv$  longitudinal static stability
2.  $C_{n\beta} > 0 \equiv$  static directional (weathercock) stability (*can not be satisfied due to the tailless design*)
3.  $C_{l\beta} < 0 \equiv$  lateral static stability
4.  $C_{Y\beta} < 0 \equiv$  sideslip stability
5.  $C_L/C_D > 5$  for  $0 < \alpha_{cruise} < 10 \text{ deg}$

With the iteration of the baseline configuration, all of the design requirements listed above are satisfied except the directional stability. This is an expected result for the tailless aircraft and details are explained in the following section where the DATCOM results are presented and discussed.

Flight conditions are chosen considering the operation of the air-taxi. As represented in Tables 2.1 and 2.2, the DATCOM input file requires the airspeed, altitude and angle of attack envelope as flight condition inputs. DATCOM results are generated only for the sea-level altitude considering that the air-taxi operations will be performed at low altitudes (approx. 0-1000 m.), and the change in aerodynamic coefficients with respect to the altitude is small for the considered altitude range. The maximum

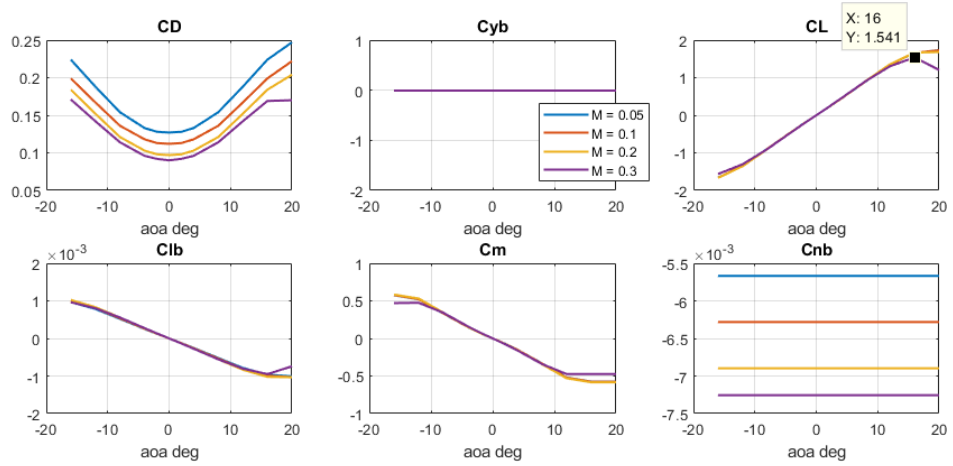


Figure 2.1: Forward flight aerodynamic modeling, static coefficients.

speed is chosen as approximately 100 m/s ( $\approx 0.3$  Mach). The minimum speed that the wing-body aerodynamics become dominant is considered 20 m/s ( $\approx 0.05$  Mach). Therefore, the airspeed range of the DATCOM input file is between 0.05 Mach and 0.3 Mach (Table 2.2). The angle of attack input range is selected as -16 degree to 20 degree, which covers the expected angle of attack values of the wing-body surfaces considering the operational flight envelope (noted that the tilting EDF surfaces which might experience a much higher range of angle of attack values are not included into the preliminary aerodynamic modeling for the scope of this study).

Based on the flight conditions and the design requirements discussed above, the Digital DATCOM input file of the final aircraft configuration and the parameter definitions of the DATCOM input file are given in Tables 2.1 and 2.2, respectively.

### 2.1.1.2 Digital DATCOM Results

The DATCOM input file given in Table 2.2 is used to find the static and dynamic coefficients. Results are represented for the Mach number and angle of attack input ranges at sea level condition.

All of the static coefficients that need to be met as design requirements are given in Figure 2.1. The longitudinal static stability condition (i.e,  $C_{m\alpha} < 0$ ) is satisfied. Lateral static stability  $C_{l\beta} < 0$  is met for positive angle of attack values, and the sideslip

Table 2.1: Digital DATCOM Parameter Definitions

Digital DATCOM	Equations	Definition
MACH	$M$	Mach number breakpoints
ALT	$h$	Altitude breakpoints
ALSCHD	$\alpha$	Angle of attack breakpoints
XCG	$X_{cg}$	Longitudinal location of cg
ZCG	$Z_{cg}$	Vertical location of cg
SREF	$S$	Theoretical wing area
CBARR	$\bar{c}$	Wing mean aerodynamic chord
BLREF	$b_{ref}$	Wing span
X	-	Body x coordinates
R	-	Body radius at the defined x coordinates
XW	-	Longitudinal location of wing
ZW	-	Vertical location of wing
CHRDTP	-	Chord at wing tip
CHRDR	-	Chord at wing root
SSPNE	-	Exposed wing semi-span
SSPN	-	Wing semi-span
SAVSI	-	Wing sweep angle
CHSTAT	-	Reference chord station for sweep angle

stability is nearly achieved since  $C_{Y\beta}$  is slightly negative. *The directional stability requirement could not be satisfied. This is an expected outcome/drawback of the tail-less design since most of the directional stability comes from the vertical tail [58]. Although  $C_{n\beta}$  values are very close to zero, the directional channel is open-loop unstable, which means that the aircraft will not align itself to the relative airflow when there is a yaw moment disturbance. Therefore, the controller must handle unstable dynamics. As mentioned previously, not having conventional stability surfaces (i.e., vertical and horizontal tail) has several advantages considering the aerodynamic efficiency, better sizing, simplicity in design etc. On the other hand, flight control becomes more challenging since the aircraft is not open-loop stable in the directional*

Table 2.2: Digital DATCOM Input File

```

$FLTCON NMACH = 4.0, MACH(1)=0.05,0.1,0.2,0.3,
  ALT=0.0, NALPHA=12.0,
  ALSCHD(1)=-16.0,-12.0,-8.0,-4.0,-2.0,0.0,2.0,4.0,8.0,12.0,16.0,20.0$
$SYNTHS XCG=2.25, ZCG=0.0$
$OPTINS SREF=2.7, CBARR=0.45, BLREF=6.6$
$BODY NX = 20.0,
  X(1)=0.0,0.2100,0.4200,0.6300,0.8400,1.0500,1.2600,1.4700,
  1.6800,1.8900, 2.1100,2.3200,2.5300,2.7400,2.9500,3.1600,3.3700,
  3.5800,3.7900,4.0000,
  R(1)=0.13,0.32,0.47,0.58,0.67,0.72,0.76,0.78,0.78,
  0.78,0.76,0.74,0.72,0.69,0.65,0.61,0.56,0.51,0.44,0.36$
$SYNTHS XW=2.42, ZW=0.0, ALIW=0.0$
$WGPLNF CHRDTP=0.3, SSPNE=3.0, SSPN=3.3, CHRDR=0.6,
  SAVSI=5.71, CHSTAT=0.25,SWAFP=0.0, TWISTA=0.0,SSPNDD=0.0,
  DHDADI=0.0,DHDADO=0.0, TYPE=1.0$
NACA-W-4-0012
CASEID LILIUM AXISYMMETRIC BODY WING
DIM M
SAVE
DAMP
NEXT CASE

```

*channel. A detailed discussion of the open-loop instability and other flight control related challenges will be mentioned in Section 3.1.*

Regarding the separation of flow over the fixed-wing surface, Figure 2.1 shows that stall condition starts above 16 degrees of angle of attack. Therefore, the controller is designed to avoid stall region such that the trim angle of attack values are much lower than 16 degrees. According to Figure 2.4,  $C_L/C_D$  is around 5 for  $\alpha$  around 4-5 degrees. Therefore, for efficient and safe cruise flight, the trim angle of attack should be close to this level. A detailed discussion of the trim angle of attack at cruise, which is selected as 4 degrees, is also given in Section 3.2.3.1.

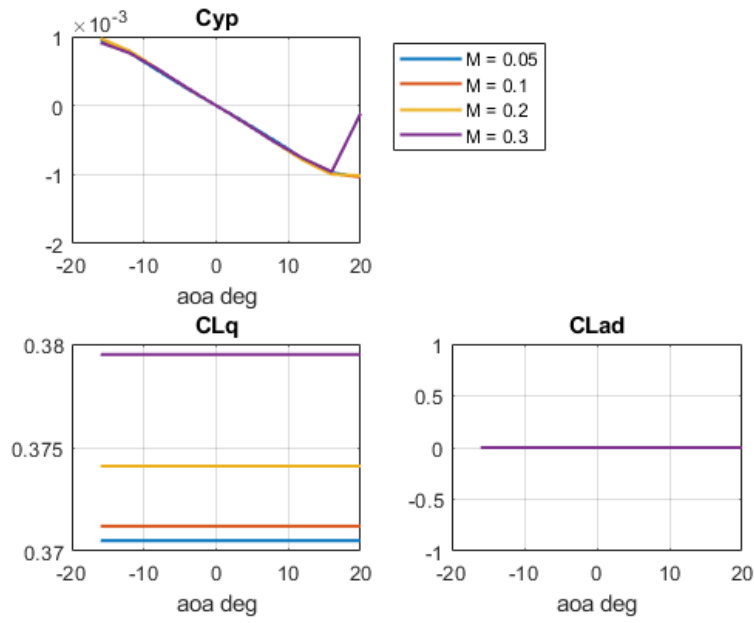


Figure 2.2: Forward flight aerodynamic modeling, dynamic force coefficients.

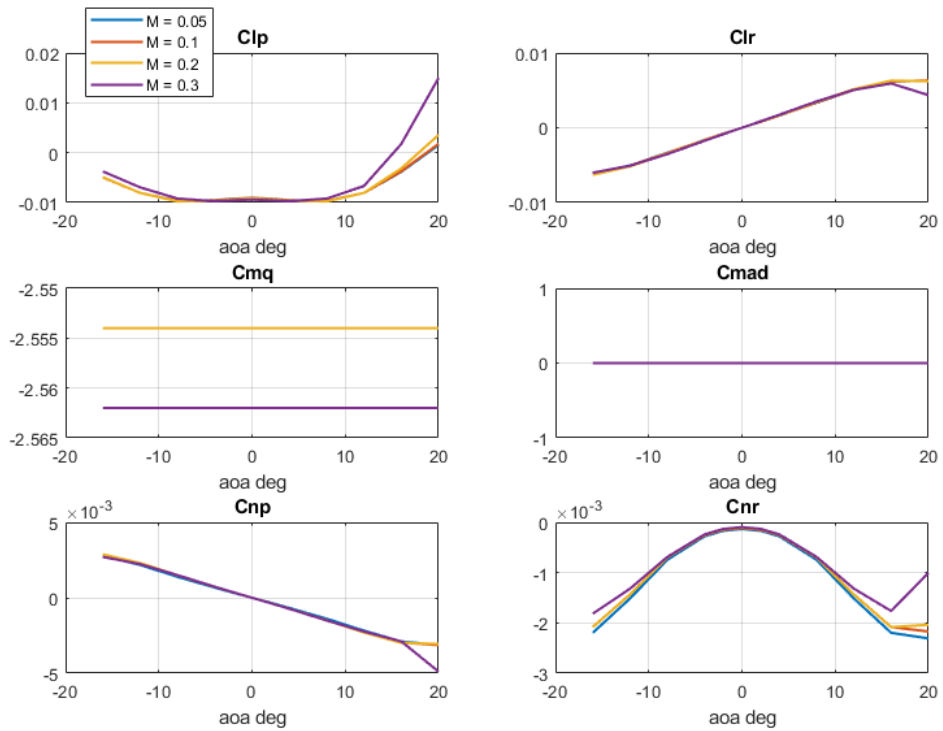


Figure 2.3: Forward flight aerodynamic modeling, dynamic moment coefficients.



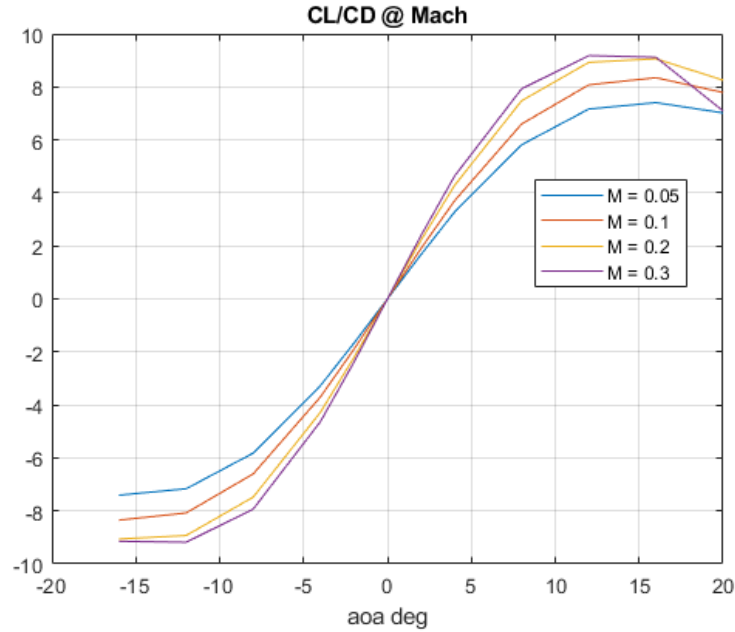


Figure 2.4: Forward flight aerodynamic modeling, Lift to Drag ratio (L/D).

Dynamic coefficients are also estimated via DATCOM, and they are represented in Figures 2.2 and 2.3 for force and moment coefficients, respectively. Digital DATCOM couldn't find  $C_{L\dot{\alpha}}$  and  $C_{m\dot{\alpha}}$  dynamic derivatives. Therefore, these coefficients are taken as zero. It is noted that nonlinearities are observed for some of the dynamic coefficients above stall angle of attack as expected.

According to Figures 2.1, 2.2, and 2.3, Digital DATCOM gives coefficients as a function of Mach number and angle of attack. The results of DATCOM can be used as look-up tables; however, it is preferred to obtain functions for each coefficient using the curve-fitting approach. According to the DATCOM results, variation with Mach number is significant only for  $C_D$  and dynamic coefficients above stall region. Considering these results, all of the coefficients apart from  $C_D$  are represented as a function of angle of attack, whereas  $C_D$  is estimated as a function of both angle of attack and Mach. Static and dynamic coefficients are given as functions in the following Equation set. MATLAB's "polyfit" command is used to determine the polynomial coefficients.

$$\left. \begin{aligned}
C_D &= 0.1425 - 0.3395 \cdot M + 0.00038 \cdot (\alpha \cdot 180/\pi)^2 + 0.5479 \cdot M^2 \\
C_{y\beta} &= -0.0075 \\
C_L &= 0.1128 \cdot \alpha \cdot 180/\pi \\
C_{l\beta} &= -6.68 \cdot 10^{-5} \cdot \alpha \cdot 180/\pi \\
C_m &= -0.0425 \cdot \alpha \cdot 180/\pi \\
C_{n\beta} &= -0.0066 \\
C_{yp} &= -6.5 \cdot 10^{-5} \cdot \alpha \cdot 180/\pi \\
C_{Lq} &= 0.3726 \\
C_{L\dot{\alpha}} &= 0 \\
C_{lp} &= -0.0093 - 7.37 \cdot 10^{-6} \cdot (\alpha \cdot 180/\pi)^2 \\
C_{lr} &= 4.21 \cdot 10^{-4} \cdot \alpha \cdot 180/\pi \\
C_{mq} &= -2.554 \\
C_{m\dot{\alpha}} &= 0 \\
C_{np} &= -1.88 \cdot 10^{-4} \cdot \alpha \cdot 180/\pi \\
C_{nr} &= -1.11 \cdot 10^{-4} - 9.19 \cdot 10^{-6} \cdot (\alpha \cdot 180/\pi)^2
\end{aligned} \right\} \quad (2.1)$$

Functions are valid in the range of predefined input regions which are given in Equation 2.2. The out-of range inputs are clipped to the minimum and maximum values. The minimum and maximum values are determined considering the DATCOM outputs and stall regions given in Figures 2.1, 2.2, 2.3. Mach number range is chosen between 0.05 and 0.5 considering a margin for the maximum airspeed.

$$\left. \begin{aligned} -20 \text{ deg} < \alpha < +20 \text{ deg} \\ -20 \text{ deg} < \beta < +20 \text{ deg} \\ 0.05 < Mach < 0.5 \end{aligned} \right\} \quad (2.2)$$

### 2.1.1.3 Wing-Body Aerodynamic Forces and Moments

Once the aerodynamic coefficients are represented in function form, static and dynamic contributions of the aerodynamic coefficients are written as follows.

Static contributions:

$$\left. \begin{aligned} C_{D,sta} &= C_D \\ C_{y,sta} &= C_{y\beta} \cdot \beta \cdot 180/\pi \\ C_{L,sta} &= C_L \\ C_{l,sta} &= C_{l\beta} \cdot \beta \cdot 180/\pi \\ C_{m,sta} &= C_m \\ C_{n,sta} &= C_{n\beta} \cdot \beta \cdot 180/\pi \end{aligned} \right\} \quad (2.3)$$

Dynamic contributions:

$$\left. \begin{aligned} C_{D,dyn} &= 0 \\ C_{y,dyn} &= C_{yp} \cdot p_s \cdot 180/\pi \cdot (b_{ref}/(2V_{air})) \\ C_{L,dyn} &= (C_{Lq} \cdot q_s + C_{L\dot{\alpha}} \cdot \dot{\alpha}) \cdot 180/\pi \cdot (\bar{c}/(2V_{air})) \\ C_{l,dyn} &= (C_{lp} \cdot p_s + C_{lr} \cdot r_s) \cdot 180/\pi \cdot (b_{ref}/(2V_{air})) \\ C_{m,dyn} &= (C_{mq} \cdot q_s + C_{m\dot{\alpha}} \cdot \dot{\alpha}) \cdot 180/\pi \cdot (\bar{c}/(2V_{air})) \\ C_{n,dyn} &= (C_{np} \cdot p_s + C_{nr} \cdot r_s) \cdot 180/\pi \cdot (b_{ref}/(2V_{air})) \end{aligned} \right\} \quad (2.4)$$

It is noted that, the DATCOM program gives coefficients in the stability axes system [100, 70]. In equation set 2.4,  $p_s, q_s, r_s$  represents angular velocity of the stability

axes with respect to the inertial frame (Earth) defined in the stability axes coordinate system. Derivation of  $\omega_{s/e}^s = [p_s, q_s, r_s]$  is given as following [86]. The sub and upper scripts  $b, s,$  and  $e$  in the equations represent the aircraft body, stability and Earth (inertial) frames, respectively.

$$\left. \begin{aligned}
 \omega_{b/s}^s &= \omega_{b/s}^b = [0, \dot{\alpha}, 0] \\
 \omega_{b/e}^b &= [p, q, r] \\
 \omega_{s/e}^b &= \omega_{s/b}^b + \omega_{b/e}^b = [p, q - \dot{\alpha}, r] \\
 \omega_{s/e}^s &= [p_s, q_s, r_s] = T_{sb} \omega_{s/e}^b \\
 T_{sb} &= \begin{bmatrix} \cos(\alpha) & 0 & \sin(\alpha) \\ 0 & 1 & 0 \\ -\sin(\alpha) & 0 & \cos(\alpha) \end{bmatrix} \\
 T_{bs} &= T_{sb}^T
 \end{aligned} \right\} \quad (2.5)$$

where  $T_{sb}$  is the transformation matrix from the aircraft body axes to the stability axes coordinate system.

Overall aerodynamic forces and moments of the wing-body are obtained in the stability axes coordinate system. However, our aim is to write the equations of motion in the aircraft body axes. Therefore, a transformation from the stability axes to the aircraft body axes is required. Moreover, the DATCOM sign convention for  $C_L$  and  $C_D$  is opposite to the aircraft body  $x$  and  $z$  axis. Therefore, to obtain body axes force terms,  $x$  and  $z$  components are multiplied with -1. Then, the aerodynamic forces and moments represented in the aircraft body axes coordinate system are obtained as follows using the stability to body axes transformation matrix  $T_{bs}$ .

$$F_{aero,forward}^b = T_{bs} \begin{bmatrix} -\bar{q} S C_{D,sta} \\ \bar{q} S (C_{y,sta} + C_{y,dyn}) \\ -\bar{q} S (C_{L,sta} + C_{L,dyn}) \end{bmatrix} \quad (2.6)$$

$$M_{aero,forward}^b = T_{bs} \begin{bmatrix} \bar{q}S(C_{l,sta} + C_{l,dyn})b_{ref} \\ \bar{q}S(C_{m,sta} + C_{m,dyn})\bar{c} \\ \bar{q}S(C_{n,sta} + C_{n,dyn})b_{ref} \end{bmatrix} \quad (2.7)$$

where static and dynamic coefficients are given in Equations 2.3 and 2.4,  $\bar{q}$ ,  $b_{ref}$ ,  $\bar{c}$ ,  $S$  are dynamic pressure, wing span, mean aerodynamic chord and wing area given in Tables 2.1 and 2.2.

### 2.1.2 Hover Flight: Estimation of Aerodynamic Resistance Force

In hover and low-speed flight near hover condition, it is reasonable to assume that the dominant aerodynamic effect is the resistance drag force in translational axes (horizontal, vertical, and sideward motion). Lift force and aerodynamic moments are considered negligible and not modeled at low-speed flight since the maximum speed is restricted to 10 m/s for horizontal motion and 5 m/s for vertical motion. Ground effect is also relevant for the hover flight. However, it is not modeled for the preliminary modeling since it requires more detailed and complex aerodynamic modeling.

Drag is estimated as a resistance force for each direction, and it is based on flat-plate for y and z directions; whereas, for x direction the aircraft is assumed to be a circular cylinder. Before estimating the drag forces, first, effective frontal areas are calculated roughly for each direction as follows.

$$\left. \begin{aligned} S_x &= \pi h_{fus}^2/4 \approx 3 \text{ m}^2 \\ S_y &= l_{fus} h_{fus} = 8 \text{ m}^2 \\ S_z &= l_{fus} h_{fus} + S \approx 10 \text{ m}^2 \\ h_{fus} &= 2 \text{ m} , \quad l_{fus} = 4 \text{ m} , \quad S = 2.7 \text{ m}^2 , \end{aligned} \right\} \quad (2.8)$$

where  $h_{fus}$ ,  $l_{fus}$  and  $S$  are the mean fuselage height, fuselage length and wing reference area, respectively (see Table 2.7).

Once the effective frontal areas are calculated, then drag force at low-speed flight is estimated as in Equation 2.9. Since the aircraft can move backwards and sideward in both direction, "sign" function is added to the equations to consider the direction of motion.

$$F_{aero,hover}^b = \begin{bmatrix} -sign(u) 0.5 \rho u^2 S_x C_{d,x} \\ -sign(v) 0.5 \rho v^2 S_y C_{d,y} \\ -sign(w) 0.5 \rho w^2 S_z C_{d,z} \end{bmatrix} \quad (2.9)$$

In Equation 2.9 it is more reasonable to use velocities that are normal to the frontal areas instead of the body velocities. However, the error introduced due to using the body velocities is considered negligible for the purpose of preliminary modeling.

The drag coefficients for y and z directions ( $C_{d,y}$  and  $C_{d,z}$ ) are for a rectangular plate and equal to 1.2; whereas, the drag coefficient of a circular cylinder, which is equal to 0.74, [67] is used for x direction.

To sum up, it is assumed that at low speeds, the dominant aerodynamic contribution is the drag force acting in the opposite direction of motion. Estimation of the drag force for each translational axes is given in Equation 2.9.

### 2.1.3 Complete Aerodynamic Model Considering the Transition

Once the aerodynamic models are generated for hover and forward flight, it is possible to merge them considering the transition between hover and forward flight. Regarding the merging coefficient, it is reasonable to use body x velocity ( $u$ ) as the decision parameter.  $u$  is selected instead of  $V_{air}$  since it is possible to move sideways in hover, which will contribute to  $V_{air}$  although the wing actually does not produce lift during the sideways motion.

As mentioned in Section 2.1.1.1, wing-induced aerodynamic forces are deemed effective above 0.05 Mach which is about 20 m/s at sea level conditions. For this reason, the forward flight model (wing-body aerodynamics) is more dominant after  $u = 20m/s$ , and below this value, the hover flight model has contributions to the

overall aerodynamic model. The transition from hover to forward flight starts at 10 m/s, half of the velocity that wing-related aerodynamic forces become dominant. It is noted that the hover model is active for negative body x and y velocities. To sum up, the merging coefficient  $k_{aero}$  is defined as follows.

$$\left. \begin{array}{l}
 \mathbf{if} \ (u \geq 10 \ \& \ u \leq 20) \\
 \quad k_{aero} = (20 - u)/10 \\
 \mathbf{elseif} \ u < 10 \\
 \quad k_{aero} = 1 \\
 \mathbf{else} \\
 \quad k_{aero} = 0 \\
 \mathbf{end}
 \end{array} \right\} \quad (2.10)$$

Finally, the complete aerodynamic model considering the transition flight is expressed in the following equation using the merging coefficient  $k_{aero}$ .  $F_{aero,forward}^b$ ,  $M_{aero,forward}^b$  and  $F_{aero,hover}^b$  are defined in Equations 2.6, 2.7, and 2.9, respectively.

$$\left. \begin{array}{l}
 F_{aero}^b = (1 - k_{aero}) F_{aero,forward}^b + k_{aero} F_{aero,hover}^b \\
 M_{aero}^b = (1 - k_{aero}) M_{aero,forward}^b
 \end{array} \right\} \quad (2.11)$$

## 2.2 Electric Ducted Fan(EDF) Modeling

In this section, the thrust, torque, and power characteristics of EDFs are estimated first. Second, total EDF number and their distribution are decided mainly considering the Thrust to Maximum Takeoff Weight ratio ( $T/W_{MTOW}$ ) and pitch moment balance at hover. Third, overall propulsion forces and moments generated by the EDFs are represented in the aircraft body coordinate system similar to the aerodynamic forces/-moments. Finally, actuator dynamics of EDFs are defined in detail, considering the rpm/thrust and tilting dynamics.

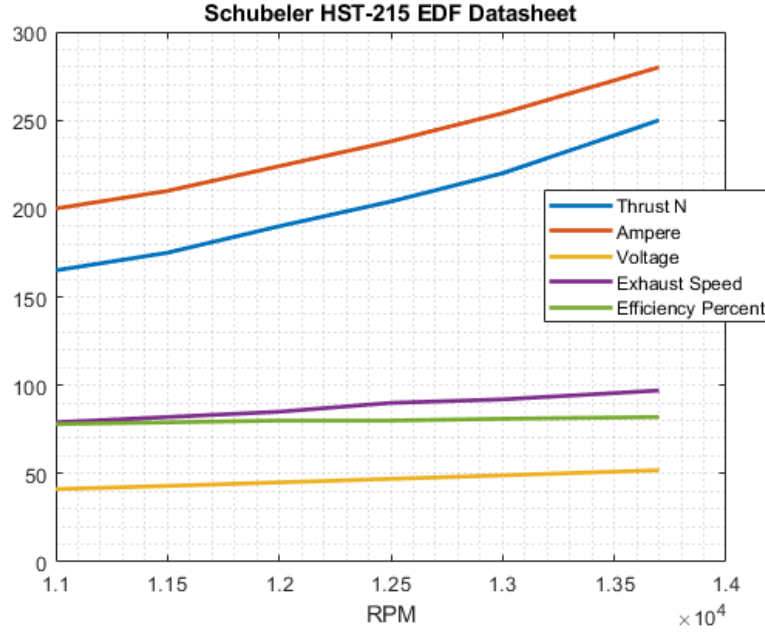


Figure 2.5: Schübeler HST-215 Electric Ducted Fan (EDF), data taken from [13].

### 2.2.1 Estimation of the Thrust and Torque Coefficients

In the DEP VTOL concept, it might be beneficial to use different EDFs for vertical and cruise flights by optimizing the design of EDFs for specific purposes such as higher efficiency in cruise or hover flight [90]. However, design optimization is not the focus of this thesis. Therefore, it is assumed that all EDFs are identical and have the same characteristics.

An off-the-shelf EDF product, named Schübeler HST-215 [13], fits the purpose of this study. A similar EDF is used in a NASA-founded DEP aircraft project [41]. To model the thrust, torque, and power characteristics of the Schübeler EDF, datasheet represented in Figure 2.5 is used [13]. Other parameters of the Schübeler HST-215 EDF are given in Table 2.3.

Relation between the thrust and rpm is approximated by up to third order polynomials, and it is seen that using an average  $C_T$  (Thrust coefficient) value gives thrust characteristics accurate enough (see Figure 2.6).

Equation 2.12 gives the thrust of each EDF based on the estimated thrust coefficient  $C_T$  and rpm.



Table 2.3: Parameters of the Schübeler HST-215 EDF.

Maximum torque, Nm	10
Maximum Power, kW	15.6
Mass, kg	3.4
Diameter, cm	21

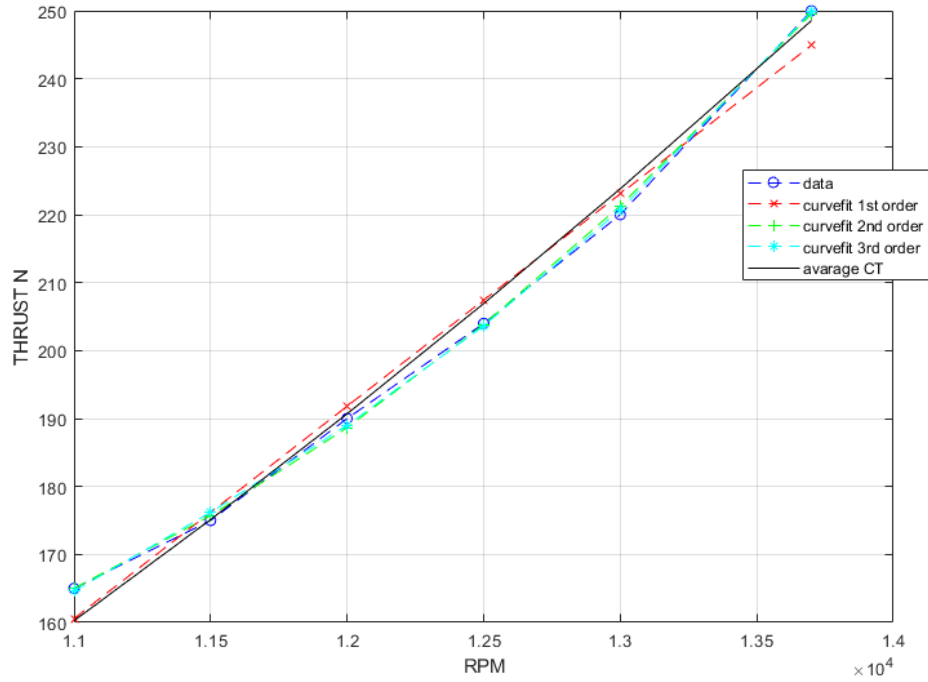


Figure 2.6: Schübeler HST-215 Electric Ducted Fan Thrust coefficient ( $C_T$ ) Estimation.

$$T = C_T (rpm \ 2\pi/60)^2 (N), \quad \text{where } C_T = 1.2032e - 04 \ Ns^2 \quad (2.12)$$

Since only the maximum torque data exist (see Table 2.3), the torque coefficient ( $C_Q$ ) is approximated using the maximum values. The relation between the thrust and torque is given as following.

$$Q = C_Q T (Nm), \quad \text{where } C_Q = 0.04 \ m \quad (2.13)$$

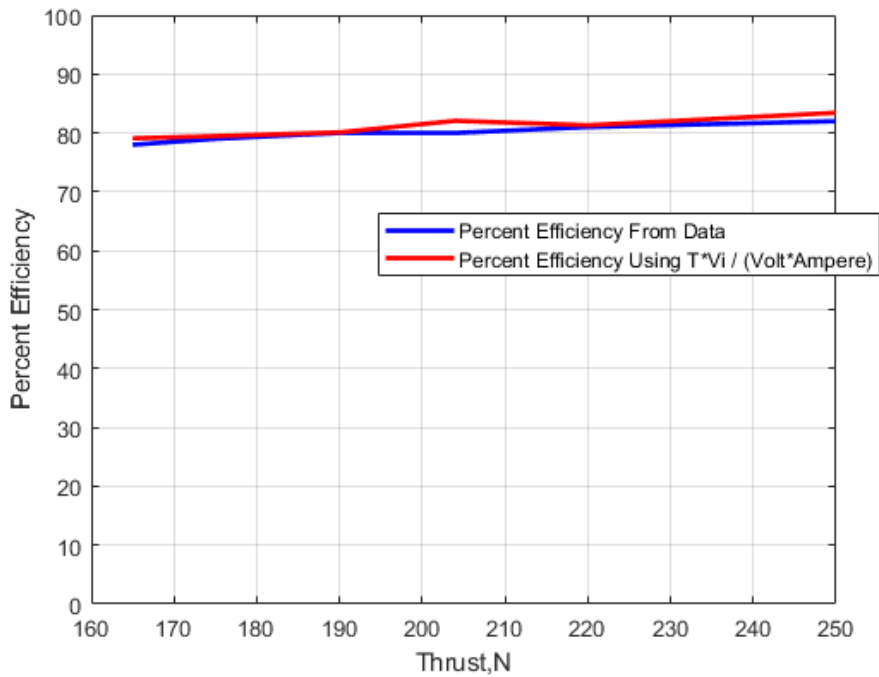


Figure 2.7: Efficiency values of Schübler EDF

As shown in Figure 2.5, the efficiency of Schübler EDF is quite high and close to % 80. Using the data given in Figure 2.5, the efficiency value is verified using the Momentum Theory [73]. Rotor efficiency or Figure of Merit (M) is defined as following [73].

$$M = \frac{\text{ideal induced power}}{\text{actual induced power}} = \frac{T V_i}{\text{Voltage Ampere}}, \quad V_i = \text{induced velocity} \quad (2.14)$$

where  $V_i$  is the induced velocity and approximately equals to half of the exhaust speed according to the Momentum Theory[73]. Equation (2.14) is applied to the data sheet of Schübler EDF given in Figure 2.5. The efficiency values are computed and compared with the efficiency value provided in the data-sheet. The comparison results given in Figure 2.7 illustrate that the data sheet values are consistent with the efficiencies obtained via the Momentum Theory (i.e., using the induced velocity).

### 2.2.2 Deciding on the Total Number of EDFs and Their Distribution

The aircraft has a maximum takeoff mass of 500 kg, and the corresponding maximum takeoff weight is 4905 N. To perform VTOL maneuvers and low speed hover flight safely, it is preferable to have thrust to maximum takeoff weight ratio ( $T/W_{MTOW}$ ) above 1.5. In the previous section, parameters of Schübeler EDF are given. The EDF can generate a maximum thrust above 250 N. It is assumed that the EDFs considered in this thesis generate a maximum thrust of 300 N, which is a little higher than the values provided by the data sheet. Then, 26 EDFs are required to have  $T/W_{MTOW}$  above 1.5 and also having an even number of total EDF considering the symmetric EDF distribution. With 26 EDFs, the thrust to maximum takeoff weight ratio is calculated as follows.

$$T/W_{MTOW} = \frac{26 \cdot 300N}{4905N} = 1.59 \quad (2.15)$$

The distribution of 26 EDFs between the front/canard and wing sections is done considering the pitch moment balance at hover. 8 EDFs are placed on the front sections, whereas 18 EDFs are on the wing sections. To achieve zero pitch moment at hover, x-lever arms ( $\Delta x$ ) of the front and wing section EDFs are chosen as 2.1 m and 0.85 m, respectively (see Figure 2.8). To simplify modeling and control effort, the total number of 26 EDFs are divided into 10 EDF sets where 4 of them are on the front sections and 6 sets are on the wing sections. There are 2 EDFs on the front EDF sets, whereas the wing EDF sets have 3 EDFs in total (see Table 2.4). Rpm/thrust and tilt angle of each EDF set are adjusted to control the aircraft via thrust vectoring for the entire flight envelope. EDFs on the right and left side of the aircraft rotate in different directions to have zero yaw moment induced by the EDF-generated torque. Table 2.4 gives the naming convention of EDF sets, turn directions, x and y lever arms (i.e.,  $\Delta x$  and  $\Delta y$ ), and control input naming for rpm and tilt angle of each EDF set. Rpm and tilt angle limits and dynamics are defined in Section 2.2.4 in detail.

Table 2.4: EDF sets definitions and parameters

Number & Name of the EDF set	Number of EDF in set $n_{edf}$	Turn direction $\sigma_{edf}$	cg X loc. in AC body axes $\Delta x_{edf}$ (m)	cg Y loc. in AC body axes $\Delta y_{edf}$ (m)	Tilt angle $\delta_{edf}$	Rpm $rpm_{edf}$
1, Front Left Tip, <i>flt</i>	2	CCW(+)	2.1	-1.1	$\delta_{flt}$	$rpm_{flt}$
2, Front Left Root, <i>flr</i>	2	CCW(+)	2.1	-0.5	$\delta_{flr}$	$rpm_{flr}$
3, Front Right Tip, <i>frt</i>	2	CW(-)	2.1	1.1	$\delta_{frt}$	$rpm_{frt}$
4, Front Right Root, <i>frl</i>	2	CW(-)	2.1	0.5	$\delta_{frl}$	$rpm_{frl}$
5, Wing Left Tip, <i>wlt</i>	3	CW(-)	-0.85	-2.95	$\delta_{wlt}$	$rpm_{wlt}$
6, Wing Left Middle, <i>wlm</i>	3	CW(-)	-0.85	-2.05	$\delta_{wlm}$	$rpm_{wlm}$
7, Wing Left Root, <i>wlr</i>	3	CW(-)	-0.85	-1.15	$\delta_{wlr}$	$rpm_{wlr}$
8, Wing Right Tip, <i>wrt</i>	3	CCW(+)	-0.85	2.95	$\delta_{wrt}$	$rpm_{wrt}$
9, Wing Right Middle, <i>wrm</i>	3	CCW(+)	-0.85	2.05	$\delta_{wrm}$	$rpm_{wrm}$
10, Wing Right Root, <i>wrr</i>	3	CCW(+)	-0.85	1.15	$\delta_{wrr}$	$rpm_{wrr}$

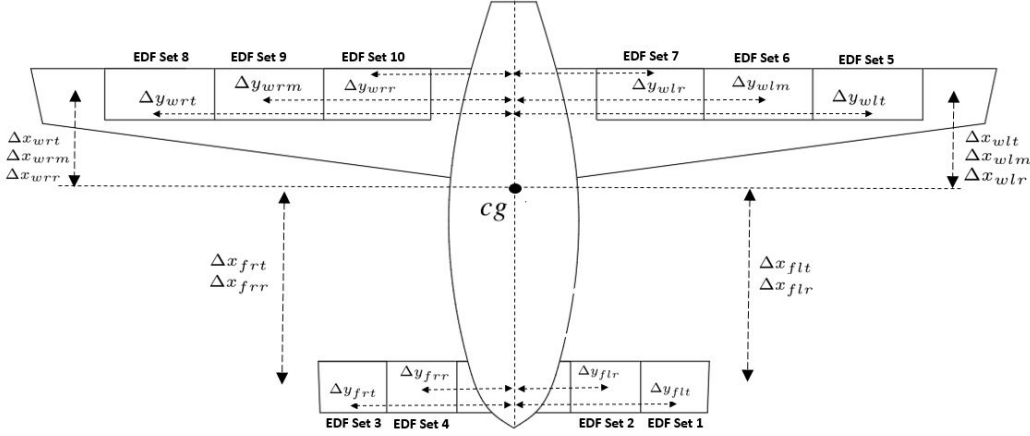


Figure 2.8: Top view of the aircraft showing EDF sets and their distribution.

### 2.2.3 EDF Propulsion Forces and Moments

The distribution of EDFs over the front and wing sections are defined in the previous section and illustrated in Figure 2.8. In this section, propulsion forces and moments generated by EDFs are defined in the aircraft body coordinate system.

Thrust and torque values are obtained in Equations 2.12 and 2.13), respectively. Then, force and moment of each EDF unit can be written in the EDF body coordinate system as follows.  $( )^m$  represents the body coordinate system of EDFs. For the torque equation,  $\sigma$  represents the turn direction which is either clockwise (CW) defined as

positive or counterclockwise (CCW) defined as negative (see Table 2.4).

$$F_{edf}^m = \begin{bmatrix} T \\ 0 \\ 0 \end{bmatrix} \quad (2.16)$$

$$M_{edf}^m = \sigma \begin{bmatrix} Q \\ 0 \\ 0 \end{bmatrix} \quad (2.17)$$

The above equations define thrust and torque generated by each EDF in the EDF body coordinate system ( $()^m$ ). As described in Table 2.4, 26 EDFs are distributed to 10 EDF sets over the front and wing sections. Then, propulsion forces and moments generated by each EDF set are given in Equations 2.18 and 2.19, respectively. Equations are written in the aircraft body coordinate system ( $()^b$ ) using the basic geometry and transformation matrix from the EDF body coordinate system to the aircraft body coordinate system ( $T_{bm}$ ). The thrust vector control illustrated in Figure 3.10 is used to generate the transformation matrix  $T_{bm}$ .

In Equation 2.17, the moment is defined with respect to the EDF's center of pressure, assuming that the EDF's center of pressure is the same as the EDF's center of gravity (cg). Therefore, the moment equation 2.19 involves two terms: transformation of EDF torque to the aircraft body coordinate system and moment contributions of EDF thrust vector at the aircraft cg.

$$F_{edf}^b = T_{bm} F_{edf}^m = \begin{bmatrix} \cos(\delta_{edf}) & 0 & \sin(\delta_{edf}) \\ 0 & 1 & 0 \\ -\sin(\delta_{edf}) & 0 & \cos(\delta_{edf}) \end{bmatrix} \begin{bmatrix} T_{edf} \\ 0 \\ 0 \end{bmatrix} n_{edf} = \begin{bmatrix} \cos(\delta_{edf}) T_{edf} \\ 0 \\ -\sin(\delta_{edf}) T_{edf} \end{bmatrix} n_{edf} \quad (2.18)$$

$$M_{edf}^b = T_{bm} M_{edf}^m + R_{EDF,cg/AC,cg} \times F_{edf}^b = \begin{bmatrix} \cos(\delta_{edf}) & 0 & \sin(\delta_{edf}) \\ 0 & 1 & 0 \\ -\sin(\delta_{edf}) & 0 & \cos(\delta_{edf}) \end{bmatrix} \begin{bmatrix} Q_{edf} \\ 0 \\ 0 \end{bmatrix} \sigma_{edf} n_{edf} \\ + \begin{bmatrix} \Delta x_{edf} \\ \Delta y_{edf} \\ \Delta z_{edf} \end{bmatrix} \times \begin{bmatrix} \cos(\delta_{edf}) T_{edf} \\ 0 \\ -\sin(\delta_{edf}) T_{edf} \end{bmatrix} n_{edf} \quad (2.19)$$

In the above equations,  $\Delta x_{edf}$ ,  $\Delta y_{edf}$  are the lever arms in x and y directions (cg location of each EDF set with respect to the aircraft cg) given in Table 2.4, and  $\Delta z_{edf}$  is taken as zero since it is deemed negligible. As described also in Table 2.4,  $n_{edf}$  and  $\sigma_{edf}$  are the number of EDF units in the corresponding set and the turn direction, respectively.

#### 2.2.4 EDF Actuator Dynamics

As mentioned previously, the aircraft do not have conventional control surfaces, and the tilt angle and rpm/thrust of each EDF set are adjusted to control the aircraft for the entire flight envelope. It is noted that rpm is related to thrust as given in Equation (2.12). Therefore, either rpm or trust can be used as a control input. Actuator dynamics (i.e., the tilt angle and thrust dynamics) are defined in this section considering the data sheet of Schübeler EDF and literature work regarding the same EDF.

Thrust dynamics are modeled based on a study [41] that concern similar Schübeler EDF used in this thesis. In this study, wind tunnel data of a Schübeler EDF is analyzed, and thrust dynamics are modeled by a 2nd order transfer function with a natural frequency of 18.85 rad/s and damping ratio of 1 [41]. Based on this data, actuator dynamics are assumed to be a little bit faster, and 2nd order transfer function with the natural frequency of 25 rad/s, and the damping ratio of 1 is used to model the thrust dynamics. The minimum and maximum thrust limits are 0 N and 300 N that corresponds to approximately 0 and 15000 rpm, respectively. The maximum limit is based on the EDF data sheet illustrated in Figure 2.5. Regarding the minimum thrust limit, achieving 0 rpm may not be possible in reality. Nevertheless, the aim is to define a reasonable minimum thrust limit considering the verification of the controller.

Regarding the tilting dynamics of EDFs, there is no exact reference value for the modeling. Therefore, assumptions are made considering the small size and mass of EDFs. Based on the data sheet given in Table 2.3, each EDF has 3.4 kg mass and 20 cm fan diameter. Therefore, it is reasonable to assume that hinge moments to rotate EDF sets will be very small. Then, tilting dynamics is modeled as a 2nd order transfer function with a natural frequency of 10 rad/s and a damping ratio of 1. Moreover, the rate limit of the tilting mechanism is taken as  $\pm 90$  deg/s. Minimum

and maximum position limits of the tilt angles are considered separately for the EDFs on the front and wing sections. Wing EDFs are deflected between 0 and 120 degrees. The minimum tilt angle is taken 0 degrees since EDFs are on the trailing edge of the wing. It is noted that EDFs are parallel to the wing surface when the tilt angle is 0 degrees. For the EDFs on the front sections, there is no fixed surface, so that the minimum limit is extended to -30 degrees, whereas the maximum limit is the same as wing EDFs (i.e., 120 degrees).

To conclude, the thrust and tilt angle dynamics are represented as 2nd order transfer functions given as follows. Natural frequency and damping ratio of the transfer functions, and position and rate limits are given in Table 2.5.

$$\frac{T}{T_{cmd}} = \frac{\omega_{n_T}^2}{s^2 + 2\zeta_T\omega_{n_T}s + \omega_{n_T}^2} \quad (2.20)$$

$$\frac{\delta}{\delta_{cmd}} = \frac{\omega_{n_\delta}^2}{s^2 + 2\zeta_\delta\omega_{n_\delta}s + \omega_{n_\delta}^2} \quad (2.21)$$

Table 2.5: Parameters of the thrust/rpm and the tilt angle actuator dynamics (note that relation between the thrust and rpm is defined in Equation (2.12)).

Control input	$\omega_n$	$\zeta$	Minimum	Maximum	Rate limit
$T$ for all EDFs	25 rad/s	1	0 N	300 N ( $\approx 15000$ rpm)	-
$\delta$ for front EDFs	10 rad/s	1	-30 deg	120 deg	$\pm 90$ deg/s
$\delta$ for wing EDFs	10 rad/s	1	0 deg	120 deg	$\pm 90$ deg/s

Moreover, the following Figure shows the block diagram of the overall actuator dynamics used in the 6-DOF simulation model.

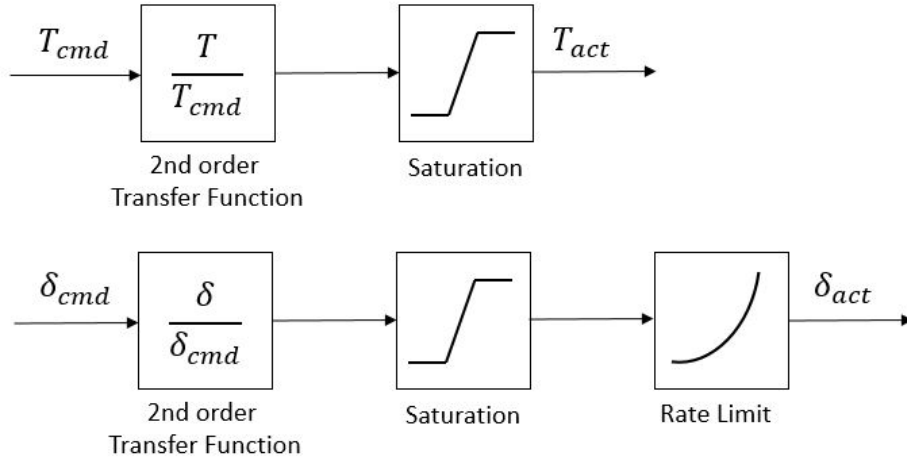


Figure 2.9: Block diagram of the actuator dynamics model.

### 2.3 Sensor Modeling

As explained briefly in the introduction chapter (Section 1.2), the INDI control approach implemented in this thesis is a sensor-based dynamic inversion method. The main advantage of the INDI compared to the NDI is the reduced model dependency to perform the dynamic inversion since INDI replaces the model information with the acceleration estimations obtained from the sensor data. Therefore, including a realistic sensor model into the simulation environment is crucial to verify the performance of the INDI controller. Data of a MEMS IMU sensor is taken to build the sensor model. Noise levels of a gyroscope and accelerometer are driven from the raw sensor data [23]. In addition, the sensor time delay is taken from a study that focuses on the effect of sensor delay on an INDI-based controller [74]. Sensor model parameters are summarized in the following table.

Table 2.6: Parameters of the MEMS IMU sensor model

	Gyroscope	Accelerometer
Noise level	1 deg/s	0.1 $m/s^2$
Time delay	10 milisec.	10 milisec.



Gyroscope and accelerometer measurements are filtered to improve the INDI controller performance. It is observed that a 2nd order low-pass filter is sufficient and effective to reduce the sensor noise. Details of the noise filtering and also the data-synchronization of the INDI controller are given in Section 3.3.2.3.

## 2.4 6-DOF Equations Of Motion

Aerodynamic and propulsion forces are formulated in the aircraft body axes in the previous sections via the component build-up modeling approach. In this section, 6-DOF Equations of Motion (EOM) are defined in the aircraft body coordinate system as follows [86].

$$\begin{bmatrix} \dot{u} \\ \dot{v} \\ \dot{w} \end{bmatrix} = (F_{aero}^b + F_{prop}^b + F_{grav}^b + F_{dist}^b)/m - \begin{bmatrix} p \\ q \\ r \end{bmatrix} \times \begin{bmatrix} u \\ v \\ w \end{bmatrix}$$

$$\text{with } F_{grav}^b = \begin{bmatrix} -g \sin(\theta) \\ g \sin(\phi) \cos(\theta) \\ g \cos(\phi) \cos(\theta) \end{bmatrix} \quad (2.22)$$

$$\text{and } F_{prop}^b = \sum_{n=1}^{10} F_{edf,n}^b = \begin{bmatrix} F x_{prop} \\ 0 \\ F z_{prop} \end{bmatrix}$$

$$\begin{bmatrix} \dot{p} \\ \dot{q} \\ \dot{r} \end{bmatrix} = J^{-1} (M_{aero}^b + M_{prop}^b + M_{dist}^b - \begin{bmatrix} p \\ q \\ r \end{bmatrix} \times J \begin{bmatrix} p \\ q \\ r \end{bmatrix}),$$

$$\text{with } J = \begin{bmatrix} I_x & 0 & 0 \\ 0 & I_y & 0 \\ 0 & 0 & I_z \end{bmatrix} \quad (2.23)$$

$$\text{and } M_{prop}^b = \sum_{n=1}^{10} M_{edf,n}^b = \begin{bmatrix} L_{prop} \\ M_{prop} \\ N_{prop} \end{bmatrix}$$

$F_{aero}^b$  and  $M_{aero}^b$  represent the overall aerodynamic forces and moments given in (2.11) considering the blending between hover and forward flight models.

Propulsion forces and moments generated by each EDF set ( $F_{edf}^b, M_{edf}^b$ ) are given in Equations (2.18) and (2.19), respectively. As described in Section 2.2.2, 10 EDF sets are introduced to reduce the modeling and control effort.  $\sum_{n=1}^{10} F_{edf,n}^b$  and  $\sum_{n=1}^{10} M_{edf,n}^b$  represent total contribution of 10 EDF sets where detailed parameters are given in Table 2.4. Note that the propulsion system can not generate side-force in the aircraft body axis (i.e.,  $F_{y_{prop}} = 0$  in Equation 2.22). Side motion is indirectly controlled via changing the aircraft attitude and direction of lift vector (i.e., adjusting the roll angle at hover flight and roll/yaw angles at forward flight, see Section 3.3.2.4 for details).

Disturbance forces and moments are also introduced into the equations as  $F_{dist}^b, M_{dist}^b$ . They are used to analyze the disturbance rejection characteristics of the controller (see Section 3.3.3.6).

In addition to the force and moment equations, kinematic and navigation equations are defined as follows.

$$\begin{bmatrix} \dot{\phi} \\ \dot{\theta} \\ \dot{\psi} \end{bmatrix} = \begin{bmatrix} p + \tan(\theta)(q\sin(\phi) + r\cos(\phi)) \\ q\cos(\phi) - r\sin(\phi) \\ (q\sin(\phi) + r\cos(\phi))/\cos(\theta) \end{bmatrix} \quad (2.24)$$

$$\begin{bmatrix} \dot{p}_N \\ \dot{p}_E \\ \dot{h} \end{bmatrix} = \begin{bmatrix} u(\cos(\theta)\cos(\psi)) + v(-\cos(\phi)\sin(\psi) + \sin(\phi)\sin(\theta)\cos(\psi)) + w(\sin(\phi)\sin(\psi) + \cos(\phi)\sin(\theta)\cos(\psi)) \\ u(\cos(\theta)\sin(\psi)) + v(\cos(\phi)\cos(\psi) + \sin(\phi)\sin(\theta)\sin(\psi)) + w(-\sin(\phi)\cos(\psi) + \cos(\phi)\sin(\theta)\sin(\psi)) \\ u\sin(\theta) - v\sin(\phi)\cos(\theta) - w\cos(\phi)\cos(\theta) \end{bmatrix} \quad (2.25)$$

In equation 2.25,  $p_N$  and  $p_E$  represent North and East position on Earth and  $h$  represents the sea level altitude.

Finally, the following relations give the airspeed, angle of attack, and angle of sideslip in terms of body velocities and also the flight path angle  $\gamma$ .

$$\left. \begin{aligned} V_\infty &= \sqrt{u^2 + v^2 + w^2} \\ \alpha &= \tan^{-1}(w/u) \\ \beta &= \sin^{-1}(v/V_\infty) \\ \gamma &= \theta - \alpha \end{aligned} \right\} \quad (2.26)$$

The flight dynamics model of the air-taxi is derived in this Chapter. The following table summarizes the general parameters of the air-taxi related the flight dynamics model.

Table 2.7: General parameters of the air-taxi

Parameter	Symbol	Value	Unit
Maximum take-off mass	$m$	500	$kg$
Inertia matrix	$J = \text{diag}(I_x, I_y, I_z)$	$\text{diag}(353, 732, 1017)$	$kgm^2$
Wing-span	$b_{ref}$	6.6	$m$
Mean aerodynamic chord	$\bar{c}$	0.45	$m$
Wing reference area	$S$	2.7	$m^2$
Fuselage Length	$l_{fus}$	4	$m$
Fuselage Mean Height	$h_{fus}$	2	$m$
EDF Thrust coefficient	$C_T$	1.2032e-04	$Ns^2$
EDF Torque coefficient	$C_Q$	0.04	$m$
Total number of EDF	-	26	-
Thrust to MTOW ratio	$T/W_{MTOW}$	1.59	-
Operation altitude	-	0-1000	$m$
Maximum speed	-	$\approx 100$	$m/s$
Cruise speed	-	$\approx 80$	$m/s$



## CHAPTER 3

### UNIFIED FLIGHT CONTROLLER: DESIGN, VERIFICATION AND DISCUSSION

The study aims to design a unified flight controller for the novel eVTOL air-taxi considering the full flight envelope mainly listed as: vertical take-off and landing, low-speed flight around hover, the transition between hover and high speed forward flight/cruise, forward flight with climb/descent and turns. Throughout the thesis, the term "unified flight controller" refers to the controller that is valid for the entire flight envelope. In this chapter, the unified flight controller is designed and verified via nonlinear simulations for several test scenarios, including robustness to modeling errors and disturbance rejection characteristics. Before going into the controller design, challenges/problems of the unified flight controller design and proposed design solutions and contributions are explained briefly.

#### 3.1 Challenges of the Unified Controller Design and Main Contributions

As mentioned in Section 1.2, the studied aircraft is classified as a long-range DEP eVTOL air-taxi with a fixed wing, and it has a unique configuration compared to other long range DEP eVTOL concepts studied in the literature. *The main difference compared to the other studies is that the air-taxi does not have any conventional control and stability surfaces (e.g., aileron, rudder, elevator, horizontal and vertical tail), and pure thrust vector control is used to achieve full envelope flight control. This design choice comes with several advantages considering the range/endurance and weight constraints of the eVTOL air-taxi concept in general.* First, aircraft is aerodynamically more efficient at high speed forward flight since horizontal/vertical tail do not

cause additional drag. A detailed study about the contribution of tail surfaces' drag contribution are not conducted in this thesis. However, it can be stated that no-tail design improves the aerodynamic efficiency especially in high speed cruise flight. Another advantage is the weight and space savings. Considering the weight constraints of eVTOL air-taxis due to the heavy battery systems, avoiding any additional weight is quite advantageous. Regarding the space savings, 18 EDFs are distributed over the trailing edge of the wing surfaces. Therefore, placement of the ailerons requires additional space. *To sum up, not having traditional control and stability surfaces improve aerodynamic efficiency, provide weight and space savings and gives design flexibility in general. On the other hand, flight control becomes more complex since benefits gained from control and stability surfaces do not exist. Details of the flight control related challenges are discussed in the next paragraph in conjunction with the flight dynamics modeling.*

The studied air-taxi configuration is unique. Therefore, aircraft data is not available in the literature to build the flight dynamics model for the entire flight envelope. Building a complete and high-fidelity flight dynamics model for the studied air-taxi is quite complex and requires significant modeling effort. Therefore, a preliminary flight dynamics model is generated in Chapter 2 via estimating the main effects at hover and forward flight and blending the hover and forward flight models to model the transition dynamics. *The preliminary flight dynamics model has significant nonlinearities, especially during the transition, although the model is build based on assumptions that simplify the modeling effort (e.g., aero-propulsion couplings in transition and ground effect at hover are not modeled, see Chapter 2). Another challenge regarding the unified controller design is the open-loop directional instability at forward flight due to the tailless design.* This is an expected result since the aircraft does not have any vertical stabilizing surface. Detailed discussion is given in Section 2.1.1.2. *Apart from the problems due to nonlinearities and open-loop instability, another challenging point for the unified controller design is related to the over-actuated system and highly coupled pure thrust vector control concept.* Full envelope flight control is achieved via adjusting the thrust vector of several EDFs (18 on the wings and 9 on the canards). The aim is to control the aircraft in 6 axis/channels (i.e., 3 translational axes and 3 rotational axis). Therefore, the system is highly over-actuated since

the number of control effectors/actuators is higher than the number of control axis/channels. Moreover, it is hard to decouple the control axis and actuators due to the pure thrust vector control concept. *The aircraft does not have any traditional control surfaces that are already decoupled (e.g., aileron to roll axis, elevator to pitch axis, rudder to yaw axis). Due to over-actuation and highly coupled pure thrust vector control, Control Allocation (CA) problem becomes complicated, especially in case of limited control authority (i.e., the actuator saturation). The commanded and physically achieved actuator states differentiate from each other in case of actuator saturation. Then, the aircraft could not track the commands in all channels while satisfying the stable flight. Actuator saturation may cause catastrophic results if the limited control authority is not allocated to critical channels such as the rotational axis. A common approach is prioritizing the rotational axis over the translational axis in case of actuator saturation. To apply this approach in a simple manner, the control axis and control effectors should be linked to each other via decoupling. For conventional aircraft, decoupled control surfaces simplify resolving problems due to the actuator saturation [47]. On the other hand, for the studied aircraft, mitigating the actuator saturation-related problems is complicated due to the highly coupled pure thrust vector control.*

***CHALLENGES:*** *To sum up, challenges for the unified controller design are listed as follows:*

- *Significant nonlinearities in the flight dynamics model especially for the transition dynamics.*
- *Open loop directional instability at forward flight/cruise due to tailless design.*
- *Over-actuated system with highly coupled pure thrust vector control concept. There is no conventional control surfaces such as aileron, rudder, elevator that are inherently decoupled. Therefore, Control Allocation (CA) problem becomes complicated in case of limited control authority (i.e., the actuator saturation).*

To observe the severity of nonlinearities, first a linear and model-based controller is designed for the cruise condition via common Linear Quadratic Regulator (LQR) approach. To design the LQR cruise controller, firstly the flight dynamics model

is trimmed and linearized at cruise design condition. The aim for the LQR design was analyzing the validity range of the linear controller away from the design/trim condition via nonlinear simulations. It is observed that, LQR controller is ineffective away from the cruise trim condition, and a gain-scheduling is necessary to design a unified flight controller via model-based LQR approach (see Section 3.2.3.6). Gain-scheduled LQR controller is a classical and proven method for the conventional aircraft, but design effort might increase significantly if several design/trim points are required to have a unified flight controller that works for the full flight envelope [76]. Considering the wide flight envelope of the air-taxi, the gain-scheduled LQR approach requires considerable design effort and highly dependent on the aircraft model which is hard/costly to generate accurately. Dynamic inversion based nonlinear controller approaches avoid gain-scheduling and simplifies the controller design [36]. On the other hand, classical nonlinear dynamic inversion (NDI) based controllers are highly dependent on the aircraft model [80].

*In this thesis, an emerging and promising dynamic inversion based control method called Incremental Nonlinear Dynamic Inversion (INDI) is used to resolve the flight control challenges described above. INDI approach use sensor data instead of the aircraft model to perform the dynamic inversion, and mainly depends on the time-scale separation principle explained in Section 3.3.2.2 [80, 74]. Therefore, modeling dependency reduce significantly compared to the classical NDI approach [80, 74]. Detailed introduction and literature review about the INDI approach will be given in Section 3.3.1. To minimize the modeling dependency of the controller and reduce the controller design effort, the sensor-based nonlinear control method INDI is applied to the problem. INDI controller is formulated considering the coupling problems of thrust vector control concept and designed to build a unified controller framework valid for the entire flight envelope. To verify the design for the full flight envelope, the unified controller is tested via nonlinear simulations considering several flight conditions including the robustness to model parameters and disturbance rejection characteristics (see Section 3.3.3).*

***CONTRIBUTION 1: To conclude, one of the contribution of the thesis is design and verification of the INDI based unified flight controller for the novel eVTOL air-taxi that is not studied before to the best of author's knowledge.***



*As mentioned previously, over-actuation and highly coupled pure thrust vector control are other challenging points for the unified controller design. For over-actuated systems, it is common to use "Control Allocation (CA)" methods to allocate the control authority considering specific objectives [47]. The INDI controller aims to generate the desired translational and rotational accelerations (or forces and moments respectively) on the aircraft level. Therefore, the INDI controller can be seen as a high-level (i.e., the aircraft level) motion controller. Then, the CA generates the physical level actuator commands to achieve the desired acceleration commands generated by the INDI. This design approach gives flexibility for the over-actuated/redundant control systems [47]. However, the role of CA becomes critical in case of the limited control authority (i.e., the actuator saturation). The CA algorithm needs to allocate the limited control authority properly to guarantee stable flight. In case of actuator saturation, the commanded and physically achieved actuator states differentiates. Then, the rotational and translational commands generated by the high level motion controller (i.e., the INDI controller) can not tracked well. Therefore, actuator saturation might cause catastrophic stability problems. As a common approach, CA prioritizes rotational axis over the translational axis to track the rotational acceleration commands accurately in case of actuator saturation [77, 56]. If the control channels/axis and control effectors/actuators can be decoupled, then relating each other becomes straightforward and CA can be designed easily to resolve the actuator saturation related problems. For conventional aircraft configurations, control effectors and control axis are inherently decoupled (i.e, aileron to roll axis, elevator to pitch axis, rudder to yaw axis) [47], and the control problem is not over-actuated in general. Therefore, relating the control axis and physical actuator commands is straightforward. By this way, classical saturation mitigation approaches (e.g., anti-wind up schemes) can be applied as an extension to the controller to resolve problems due to the actuator saturation. However, for the studied air-taxi, conventional control surfaces does not exist and pure thrust vector control is used to achieve full envelope flight control. Couplings of pure thrust vector control complicates the CA design which has a vital role of guaranteeing stable flight in case of limited control authority.*

Considering these challenges, an effective CA algorithm is designed to properly allocate the control authority and guarantee stable flight in case of actuator saturation.

Simulation results show that, the role of the CA algorithm becomes critical for specific flight conditions that results in limited control authority (see Sections 3.3.3.3 and 3.3.3.6).

***CONTRIBUTION 2: To conclude, another contribution of the thesis is resolving the actuator saturation related problems via proper CA design considering the challenges due to highly coupled pure thrust vector control approach.***

Challenges regarding the unified flight controller design and the main contributions of the study are given in this section. As mentioned previously, before going into the nonlinear and sensor-based unified controller design via INDI approach, a cruise controller is designed using the classical linear and model-based control approach "Linear Quadratic Regulator (LQR)" in the next section.

## **3.2 LQR Controller Design**

In this section, a linear controller is designed at cruise trim condition via the common LQR approach. The LQR controller is tested via nonlinear simulations to analyze the severity of nonlinearities in the flight dynamics model. *Results show that the LQR controller is valid in the proximity of cruise condition, but gain-scheduling is required to design a unified LQR-based controller that works for the entire flight envelope.*

LQR controller is designed to track attitude  $(\phi, \theta, \psi)$  and body velocity  $(u, v, w)$  commands. Instead of body velocities, an outer loop can be designed to track air velocity and flight path angle. However, for the purpose of this thesis, an outer loop is not considered necessary. The critical point for the LQR design is the selection/tuning of the state and input weight matrices. To reduce the design effort, the control input size is reduced as a first step of the design. Then, cruise trim condition is found considering the reduced control input definitions and 6-DOF EOM given in Section 2.4. A two-step optimization approach is used to find the desired cruise trim condition. Once the trim point is found, the EOM is linearized at the cruise trim condition, and the linearized state space form is obtained. Then, the LQR controller is designed using the linearized state space equations. To minimize the tuning effort, the state and input weight matrices are non-dimensionalized, considering the maximum desired devia-

tion from the trim condition. The LQR is tested via nonlinear simulations, and basic maneuvers such as climb/descent and coordinated turns are performed.

*LQR controller works satisfactorily at the cruise condition. However, if the aircraft states are away from the trim condition, the LQR controller cause instability. It is concluded that to design an LQR-based unified controller that works for the entire flight envelope, classical gain-scheduled design approach is required as expected. Gain-scheduling effort depends on the severity of nonlinearities in the flight dynamics model. In Chapter 2, the flight dynamics model is generated focusing on the main effects, and some of the nonlinearities are not modeled (e.g., aero-propulsion couplings in transition, the ground effect at hover, etc.). Therefore, for a high fidelity model, the gain-scheduling effort might increase significantly considering the additional nonlinearities emerging in the flight dynamics model. To resolve the problems due to nonlinearities and model dependency, a nonlinear and sensor-based flight controller is designed via the INDI approach after the LQR controller design (see Section 3.3).*

### 3.2.1 Reduced Size Control Input Definitions

As described in Section 2.2.2, air-taxi has 26 EDFs distributed over the wing and front sections. There are two control inputs which are the rpm/thrust and tilt angle for each EDF. Therefore, the number of total control inputs for the system is 52. To simplify the controller design, EDFs are combined into 10 EDF sets, and the same rpm and tilt angles are applied to the EDFs on the same set. Definition of EDF sets and their visualization are given in Table 2.4 and Figure 2.8, respectively. With this simplification, the control input size is reduced to 20 (i.e., 10 set with 2 control inputs). To further reduce the control input size, tilt angles are also defined the same for the EDF sets on the wing-left, wing-right, front-left, and front-right sections. Therefore, there are 4 tilt angle inputs and 10 rpm inputs that reduce the control input size to 14. The control inputs used for the LQR controller design are visualized in Figure 3.1.

The reduced size control input vector is given in Equation (3.1) and the name of each input is defined in Table 2.4 with a difference that  $\delta_{fl}$ ,  $\delta_{fr}$ ,  $\delta_{wl}$ ,  $\delta_{wr}$  represent the

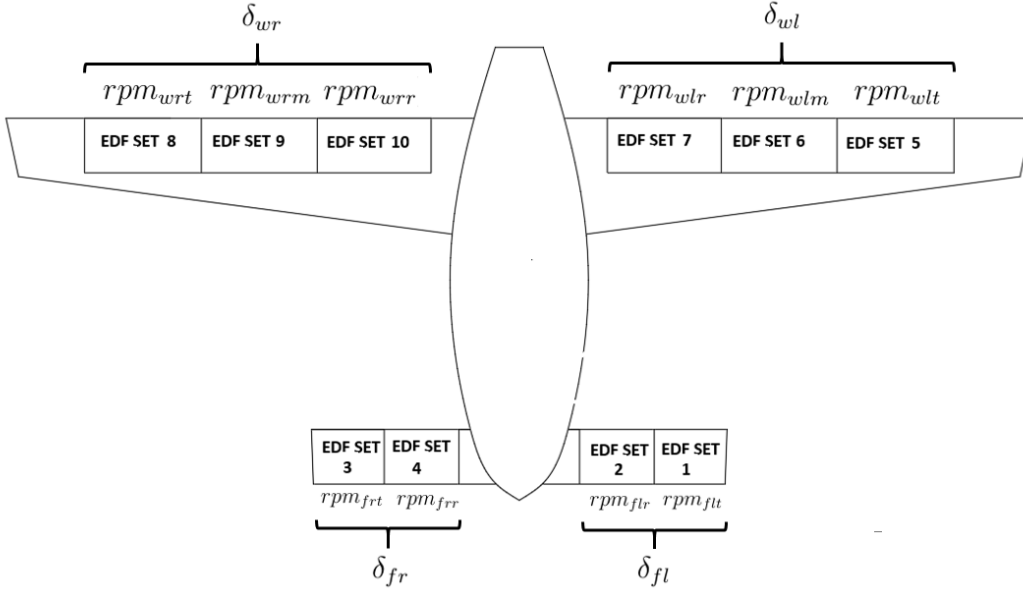


Figure 3.1: Reduced size control inputs for the LQR cruise controller design, top view.

front-left, front-right, wing-left, and wing-right EDF set tilt/deflection angle, respectively (see Figure 3.1).

$$U = [\delta_{fl} \ rpm_{flt} \ rpm_{flr} \ \delta_{fr} \ rpm_{frt} \ rpm_{frr} \ \delta_{wl} \ rpm_{wlt} \ rpm_{wlm} \ rpm_{wlr} \ \delta_{wr} \ rpm_{wrt} \ rpm_{wrm} \ rpm_{wrr}]^T \quad (3.1)$$

Once the control input vector is defined, the aircraft is trimmed & linearized at the design point as a first step of the LQR cruise controller design. The following section gives details of the trim algorithm and linear state space model generation.

### 3.2.2 Trim & Linearization

Finding trim points for aircraft is an optimization problem in general. *For a unique aircraft concept, the optimization problem might be hard to solve since a prior knowledge about the aircraft dynamics simplifies the trim point search (e.g., via defining initial/starting points properly). The studied eVTOL aircraft has several control in-*

*puts and does not have conventional control surfaces. Therefore, finding desired trim points is more complicated compared to conventional aircraft, as expected.*

Flight dynamics model is generated in MATLAB/Simulink environment based on the 6-DOF EOM defined in Section 2.4. Simulink has built-in trim functions (e.g., "findop" function) that can be used to simply find the desired trim conditions. However, it is observed that Simulink's trim algorithm may not find a feasible solution for a broad range trim point search (i.e., a wide range of flight envelope) if a good starting point is not defined. For this reason, a simplified trim algorithm is build to find a good starting guess, and then Simulink's built-in trim algorithms are used to find the feasible trim points.

Once the starting points are found, the main trim function is applied using the Simulink's built-in "findop" function, which zeroizes the time derivatives of states given through Equations (2.22) - (2.25) while satisfying the input, state, and output constraints defined by the user. The "Gradient-Descent" method is used in the trim optimization algorithm. Initial points are defined based on the "Simplified Trim Algorithm" given in the next section. *It is noted that trim points can be found easily for hover. However, the definition of initial points becomes critical to find a feasible solution for the forward flight conditions.*

### **3.2.2.1 Simplified Trim Algorithm**

The simplified trim algorithm solves the following constrained quadratic optimization problem via MATLAB's "fmincon" function. The aim is to minimize the total forces and moments acting on the aircraft cg. Lower and upper bounds are defined to have a feasible solution. The result of the simplified trim algorithm is used as an initial point for the "Main Trim Algorithm" given in the next section. The simplified algorithm is generated only for the forward flight since finding the trim points is straightforward for the hover flight.

$$\left. \begin{array}{l}
\text{minimize}_U \quad J(U) = (F^b)^T(F^b) + (M^b)^T(M^b) \\
\text{subject to} \quad U_{lb} < U < U_{ub} \\
F^b = F_{aero,forward}^b + F_{grav}^b + \sum_{i=1}^{10} F_{edf,i}^b \\
M^b = M_{aero,forward}^b + \sum_{i=1}^{10} M_{edf,i}^b \\
\text{with initial conditions} \quad U_0
\end{array} \right\} \quad (3.2)$$

Net aerodynamic forces & moments at forward flight ( $F_{aero,forward}^b$  &  $M_{aero,forward}^b$ ) are defined in Equations (2.6) and (2.7). As mentioned previously, simplified trim algorithm is generated for the cruise flight so that the aerodynamic model of only forward flight is used in the optimization. Net propulsion forces & moments ( $F_{edf,i}^b$  &  $M_{edf,i}^b$ ) are found for each EDF set based on Equations (2.18), (2.19), and Table 2.4.

Since the aim of the simplified trim algorithm is only finding initial points for the main trim algorithm, some simplifications are performed. 10 set of EDFs are divided into 2 parts which are front and wing EDF sets, so that the rpm and tilt angles of EDF sets for  $i = 1 : 4$  (front EDF sets) and for  $i = 5 : 10$  (wing EDF sets) are equal (see Figure 3.1). By this way, only 4 control inputs (i.e., the wing rpm and tilt angles and the canard rpm and tilt angles) are used in the simplified trim algorithm.

*Constraints on the control inputs ( $U_{lb}$  and  $U_{ub}$ ) depends on the actuator dynamics given in Table 2.5, and also the flight condition considered for the trim. For example, in cruise flight it is aimed to have trim tilt angles close to zero since large tilt angles will cause additional drag force.*

To conclude, according to Equations 2.22 and 2.23, if the cost function  $J$  in Equation 3.2 is minimized then the derivatives of body angular rates ( $p, q, r$ ) and velocities ( $u, v, w$ ) will approach to zero, and the trim condition will be found. In the next Section the "Main Trim Algorithm" is described in details.

### 3.2.2.2 Main Trim Algorithm

The overall trim point is found via "findop" function of MATLAB/Simulink, which uses the nonlinear flight dynamics model generated based on the 6-DOF EOM defined in Section 2.4. The "Gradient Descent" method is used in the optimization algorithm, and the solution of the simplified trim algorithm described in the previous section is used as an initial guess. Trim state and input vectors are defined as follows.

$$\begin{aligned}x_{trim} &= [\phi \ \theta \ \psi \ p \ q \ r \ u \ v \ w]^T \\U_{trim} &= [\delta_{fl} \ rpm_{flt} \ rpm_{flr} \ \delta_{fr} \ rpm_{frr} \ rpm_{frr} \ \delta_{wl} \ rpm_{wlt} \ rpm_{wlm} \ rpm_{wlr} \\&\delta_{wr} \ rpm_{wrt} \ rpm_{wrm} \ rpm_{wrr}]^T \\U_{lb} &< U_{trim} < U_{ub}\end{aligned}\tag{3.3}$$

To trim the aircraft at specific flight conditions, some of the states are set as "fixed" and others are set "free" in the configuration settings of the "findop" function.

Once the overall trim point is found, then the nonlinear 6-DOF EOM given through Equations (2.22) - (2.25) are linearized at the trim/equilibrium points.

### 3.2.2.3 Linearization

As described previously, it is desired to track attitude( $\phi, \theta, \psi$ ) and velocity commands( $u, v, w$ ) in LQR controller. Then, the linear state-space representation is defined as follows with  $A, B, C$  being the state, input and output matrices, respectively.

$$\begin{aligned}
\Delta\dot{x} &= A\Delta x + B\Delta U, \quad y = C\Delta x + D\Delta U \\
\Delta x &= x - x_{trim}, \quad \Delta U = U - U_{trim} \\
x &= [\phi \ \theta \ \psi \ p \ q \ r \ u \ v \ w]^T \\
U &= [\delta_{fl} \ rpm_{flt} \ rpm_{flr} \ \delta_{fr} \ rpm_{frr} \ rpm_{frr} \ \delta_{wl} \ rpm_{wlt} \ rpm_{wlm} \ rpm_{wlr} \\
&\quad \delta_{wr} \ rpm_{wrt} \ rpm_{wrm} \ rpm_{wrr}]^T
\end{aligned} \tag{3.4}$$

Once trim points are found via the "Main Trim Algorithm", MATLAB's "linearize" command is used to generate the linear state space matrices described above.

### 3.2.3 Design of the LQR Cruise Controller

In this section LQR controller is designed for the cruise condition. The controller can track attitude and velocity commands. Verification tests are performed via nonlinear simulations, including basic maneuvers such as climb/descent and coordinated turns at cruise flight. Moreover, the validity of the linear controller away from the design condition is analyzed using the nonlinear simulation model. In the following sections, first cruise trim point is found, and linear state space form is obtained at the trim condition. Then, the LQR controller is designed, and nonlinear simulation results are analyzed considering the feasibility of the linear controller design for the full flight envelope.

#### 3.2.3.1 Trim Point Search

Cruise trim point is found using the trim algorithm described in Section 3.2.2. In cruise flight, it is desired to fly at an angle of attack which is high but not close to the stall region. Therefore, the angle of attack value is fixed first, and the airspeed is changed in between the cruise speed range until a solution is found. If a solution does not exist for the specific angle of attack, then the angle of attack value is decreased, and the same procedure is applied iteratively. The trim algorithm starts trim point search at 8 degrees angle of attack and stops at 2 degrees with 1 degree decrements.



It is also beneficial to fly at small tilt angles since EDFs cause additional drag at high tilt angles (see Figure 3.10). For this reason, tilt angles of the front and wing EDFs are constrained by 30 and 20 degrees, respectively. Then, lower/upper bounds ( $U_{lb}, U_{ub}$ ) and initial values ( $U_0$ ) of the control input vector (see Equation 3.1) are chosen as follows considering also the actuator limits given in Table 2.5.

$$\begin{aligned}
U_{lb} &= [-\pi/6 \ 2000 \ 2000 \ -\pi/6 \ 2000 \ 2000 \ 0 \ 2000 \ 2000 \ 2000 \\
&0 \ 2000 \ 2000 \ 2000]^T \\
U_{ub} &= [\pi/6 \ 15000 \ 15000 \ \pi/6 \ 15000 \ 15000 \ \pi/9 \ 15000 \ 15000 \ 15000 \\
&\pi/9 \ 15000 \ 15000 \ 15000]^T \\
U_0 &= [0.4616 \ 8719 \ 8719 \ 0.4616 \ 8719 \ 8719 \ 0.0816 \ 3714 \ 3714 \ 3714 \\
&0.0816 \ 3714 \ 3714 \ 3714]^T
\end{aligned}
\tag{3.5}$$

As explained earlier, the aircraft has a unique configuration so that it is hard to find a good starting point for the trim point search. To solve this problem, "Simplified Trim Algorithm" described in Section 3.2.2.1 finds the first guess for the trim point search and this initial point is fed into the "Main Trim Algorithm" (Section 3.2.2.2). Following equation gives results of the "Main Trim Algorithm" for cruise considering the desired trim conditions on aircraft states and control inputs described above.

$$\begin{aligned}
U_{trim} &= [0.5153 \ 8214 \ 8214 \ 0.5153 \ 8214 \ 8214 \ 0.0780 \ 4238 \ 4238 \ 4238 \\
&0.0780 \ 4238 \ 4238 \ 4238]^T \\
x_{trim} &= [\phi \ \theta \ \psi \ u \ v \ w \ p \ q \ r]^T = [0 \ 0.0698 \ 0 \ 77.8 \ 0 \ 5.44 \ 0 \ 0 \ 0]^T \\
V_{\infty trim} &= 78, \ \alpha_{trim} = 0.0698 = 4 \text{ deg}, \ \beta_{trim} = 0, \\
J &= 0.0278
\end{aligned}
\tag{3.6}$$

It is seen that, the aircraft can be trimmed at 4 deg angle of attack and 78 m/s cruise airspeed at sea level altitude satisfying the constraints on the control inputs. In the

next section, nonlinear flight dynamics model is linearized at the cruise trim condition.

### 3.2.3.2 Linearized Model

As mentioned in previous sections, the nonlinear flight dynamics model is built on MATLAB/Simulink based on the 6-DOF EOM given in Section 2.4. The nonlinear model is linearized at the cruise trim condition given in Equation (3.6). Then, the state space matrices are found as follows considering the state space representation given in Equation (3.4).

$$A = \begin{bmatrix} 0 & 0 & 0 & 1 & 0 & 0.070 \\ 0 & 0 & 0 & 0 & 1 & 0 \\ 0 & 0 & 0 & 0 & 0 & 1.002 \\ 0 & 0 & 0 & -4.427 & 0 & 0.473 \\ 0 & 0 & 0 & 0 & -2.613 & 0 \\ 0 & 0 & 0 & -0.220 & 0 & -0.035 \\ 0 & -9.786 & 0 & 0 & -5.354 & 0 \\ 9.786 & 0 & 0 & 5.429 & 0 & -77.810 \\ 0 & -0.684 & 0 & 0 & 76.560 & 0 \\ & & & & 0 & 0 & 0 \\ & & & & 0 & 0 & 0 \\ & & & & 0 & 0 & 0 \\ & & & & 0 & 0.030 & 0 \\ & & & & -0.003 & 0 & -0.318 \\ & & & & 0 & -0.336 & 0 \\ & & & & -0.045 & 0 & 0.192 \\ & & & & 0 & -0.111 & 0 \\ & & & & -0.053 & 0 & -2.593 \end{bmatrix}$$

$$B = \begin{bmatrix} 0 & 0 & 0 & 0 & 0 & 0 & 0 \\ 0 & 0 & 0 & 0 & 0 & 0 & 0 \\ 0 & 0 & 0 & 0 & 0 & 0 & 0 \\ 0.6825 & 0.0001 & 0 & -0.6825 & -0.0001 & 0 & 1.2330 \\ 0.8888 & 0.0001 & 0.0001 & 0.8888 & 0.0001 & 0.0001 & -0.2469 \\ -0.1503 & 0 & 0 & 0.1503 & 0 & 0 & -0.0419 \\ -0.3510 & 0.0001 & 0.0001 & -0.3510 & 0.0001 & 0.0001 & -0.0332 \\ 0 & 0 & 0 & 0 & 0 & 0 & 0 \\ -0.6197 & 0 & 0 & -0.6197 & 0 & 0 & -0.4254 \\ 0 & 0 & 0 & 0 & 0 & 0 & 0 \\ 0 & 0 & 0 & 0 & 0 & 0 & 0 \\ 0 & 0 & 0 & 0 & 0 & 0 & 0 \\ 0 & 0 & 0 & -1.2330 & 0 & 0 & 0 \\ 0 & 0 & 0 & -0.2469 & 0 & 0 & 0 \\ 0.0001 & 0.0001 & 0 & 0.0419 & -0.0001 & -0.0001 & 0 \\ 0.0001 & 0.0001 & 0.0001 & -0.0332 & 0.0001 & 0.0001 & 0.0001 \\ 0 & 0 & 0 & 0 & 0 & 0 & 0 \\ 0 & 0 & 0 & -0.4254 & 0 & 0 & 0 \end{bmatrix}$$

$$C = \text{diag}([1, 1, 1, 1, 1, 1, 1, 1, 1]), \quad D = \text{zeros}(9, 14) \quad (3.7)$$

### 3.2.3.3 Analyzing the Open Loop Dynamics

It is preferable to investigate the open loop dynamics to observe the stability characteristics of the open loop system. For this purpose, eigenvalues of the  $A$  matrix are calculated via MATLAB as follows. Controllability and observability are also checked before moving into the LQR controller design.

Pole	Damping	Frequency (rad/seconds)	Time Constant (seconds)
0.00e+00	-1.00e+00	0.00e+00	Inf
2.21e-02	-1.00e+00	2.21e-02	-4.52e+01
-2.03e-02 + 4.22e-02i	4.34e-01	4.68e-02	4.92e+01
-2.03e-02 - 4.22e-02i	4.34e-01	4.68e-02	4.92e+01
-4.43e+00	1.00e+00	4.43e+00	2.26e-01
5.04e+00	-1.00e+00	5.04e+00	-1.99e-01
-5.20e+00	1.00e+00	5.20e+00	1.92e-01
-2.60e+00 + 4.93e+00i	4.67e-01	5.58e+00	3.84e-01
-2.60e+00 - 4.93e+00i	4.67e-01	5.58e+00	3.84e-01

Figure 3.2: Eigenvalues of the open loop system linearized at cruise trim condition.

*According to the eigenvalues, open loop dynamics is unstable and stable eigenvalues have very low damping values. It is noted that the aircraft does not have a vertical tail, so that the directional stability condition can not satisfied in design ( $C_{n,\beta} < 0$ , see Figure 2.1). For conventional fixed-wing aircraft, cruise trim condition generally results in stable open loop dynamics, and controller is designed to improve stability characteristics/robustness and steady-state response. For our case, the control problem is more challenging due to the directional instability. Detailed discussion about the directional instability is given in Section 2.1.1.2.*

Before moving into the LQR controller design, it must be checked whether the system is controllable or not. The controllability matrix has a rank of 9, which equals to the rank of  $A$  matrix. Therefore, the system does not have any uncontrollable states.

### 3.2.3.4 LQR Controller Design

LQR is an optimal control approach that has been used widely for the aircraft flight control [86, 58, 93, 34, 59, 37]. It is a classical linear control approach that uses the linearized aircraft model in the design. Therefore, it can be referred as a model-based linear control approach. It is noted that, the INDI approach used in this thesis is a nonlinear and sensor-based control method, and it has quite different characteristics compared to the classical LQR approach. Details of the INDI method will be given in section 3.3.1 after analyzing the LQR cruise controller's performance.

In classical LQR control, an optimal time-invariant gain matrix is found to regulate the system around the design point [17]. However, our aim is to track attitude and velocity commands while also rejecting disturbances that make the system away from the trim condition. For optimal tracking purposes, LQR can be extended, and an optimal gain matrix is found as a function of the desired trajectory [19, 54]. However, in practical applications, it is hard to use an optimal gain matrix that changes dynamically based on the desired trajectory. At this point, it is stated that an offline calculated optimal gain matrix can be used for tracking purposes if desired commands are slowly changing [19]. Since the offline calculated optimal gain matrix is used for the tracking problem, the controller becomes sub-optimal. However, this approach works pretty well if desired commands are generated via a command filter that avoids sudden changes/discontinuities in the commands [19, 88].

To find the sub-optimal LQR gain ( $K$  matrix) for tracking purposes, the cost function given in Equation (3.8) is minimized. LQR gain can be found offline via solving the Algebraic Riccati Equation (ARE). MATLAB's "lqr" command is used to find the  $K$  matrix. Since our aim is to track altitude and velocity commands, the control law includes the error between the actual aircraft state ( $x$ ) and desired aircraft state/trajectory ( $x_d$ ). Critical part is generating desired trajectory ( $x_d$ ) properly considering the physics of the problem such that the sub-optimal controller works properly for tracking purpose.

$$J = \int_0^{\infty} (\Delta x)^T Q \Delta x + (\Delta U)^T R \Delta U dt \quad (3.8)$$

$$U = \Delta U + U_{trim} = -K(x - x_d) + U_0 \quad (3.9)$$

In LQR controller design, the challenging part is selection/tuning of the state and input weight matrices ( $Q$  and  $R$ ). The tuning process might be tedious when the control input and/or state vector size is large. Considering this point, control input size is reduced to 14 in Section 3.2.1. Another approach to simplify the tuning process is using normalized weights that non-dimensionalize the cost function.

For the normalization, maximum desired/allowable values are defined for each state

and control input. Table 3.1 gives the normalization factor for the cruise case.

Table 3.1: Normalization factors used for the tuning of  $Q$  and  $R$  Matrices.

Maximum Desired Deviation from Trim (for the States)	Value	Maximum Desired Deviation from Trim (for the Control Inputs)	Value
$\phi_{max}$	15 $\pi/180$ rad	$\delta_{fl_{max}}, \delta_{fr_{max}}$	$\pi$ rad
$\theta_{max}$	5 $\pi/180$ rad	$\delta_{wl_{max}}, \delta_{wr_{max}}$	$\pi/2$ rad
$\psi_{max}$	30 $\pi/180$ rad	$rpm_{flt_{max}}, rpm_{flr_{max}}$	13000 rpm
$p_{max}$	30 $\pi/180$ rad	$rpm_{frr_{max}}, rpm_{frr_{max}}$	13000 rpm
$q_{max}$	10 $\pi/180$ rad	$rpm_{wlt_{max}}, rpm_{wlm_{max}}, rpm_{wlr_{max}}$	13000 rpm
$r_{max}$	60 $\pi/180$ rad	$rpm_{wrt_{max}}, rpm_{wrm_{max}}, rpm_{wrr_{max}}$	13000 rpm
$u_{max}$	5 m/s		
$v_{max}$	2 m/s		
$w_{max}$	2 m/s		

In Table 3.1, the values defined for states and control inputs represent the maximum allowable deviations from the cruise trim condition (given in Equation 3.6) considering also the actuator limits given in Table 2.5. Using the normalization factors given in Table 3.1,  $Q$  and  $R$  matrices are defined as follows.

$$Q = W_{Q/R} \text{diag}([Q_\phi/\phi_{max}^2, Q_\theta/\theta_{max}^2, Q_\psi/\psi_{max}^2, Q_p/p_{max}^2, Q_q/q_{max}^2, Q_r/r_{max}^2, Q_u/u_{max}^2, Q_v/v_{max}^2, Q_w/w_{max}^2])$$

$$R = \text{diag}([R_{\delta_{fl}}/\delta_{fl_{max}}^2, R_{rpm_{flt}}/rpm_{flt_{max}}^2, R_{rpm_{flr}}/rpm_{flr_{max}}^2, R_{\delta_{fr}}/\delta_{fr_{max}}^2, R_{rpm_{frr}}/rpm_{frr_{max}}^2, R_{\delta_{wl}}/\delta_{wl_{max}}^2, R_{rpm_{wlt}}/rpm_{wlt_{max}}^2, R_{rpm_{wlm}}/rpm_{wlm_{max}}^2, R_{rpm_{wlr}}/rpm_{wlr_{max}}^2, R_{\delta_{wr}}/\delta_{wr_{max}}^2, R_{rpm_{wrt}}/rpm_{wrt_{max}}^2, R_{rpm_{wrm}}/rpm_{wrm_{max}}^2, R_{rpm_{wrr}}/rpm_{wrr_{max}}^2]) \quad (3.10)$$

Normalization factors simplify the tuning of  $Q$  and  $R$  matrices considerably. First, all elements of  $Q$  and  $R$  matrices are taken as 1. Then, the main weight  $W_{Q/R}$  that represents the weight of states over control is adjusted. Finally,  $R$  matrix is tuned via nonlinear simulations to achieve control inputs that do not violate actuator dynamics. As can be seen in Equation (3.11), to give more priority to rpm control, related weights are lowered to 0.15, and weights of wing tilt angles are increased to 5 to

give less priority to tilting of wing EDFs. Based on the nonlinear simulations, it is seen that there is no need to tune state matrix  $Q$  thanks to the normalization factors. Only the weight of pitch response  $Q_\theta$  is increased to 3, and all the other weights of  $Q$  matrix are not tuned and left as 1.

$$Q = 0.1 \text{diag}( [1/\phi_{max}^2, 3/\theta_{max}^2, 1/\psi_{max}^2, 1/p_{max}^2, 1/q_{max}^2, 1/r_{max}^2, \\ 1/u_{max}^2, 1/v_{max}^2, 1/w_{max}^2 ] )$$

$$R = \text{diag}( [1/\delta_{flt_{max}}^2, 0.15/rpm_{flt_{max}}^2, 0.15/rpm_{flr_{max}}^2, \\ 1/\delta_{fr_{max}}^2, 0.15/rpm_{frt_{max}}^2, 0.15/rpm_{frr_{max}}^2, \\ 5/\delta_{wl_{max}}^2, 0.15/rpm_{wlt_{max}}^2, 0.15/rpm_{wlm_{max}}^2, 0.15/rpm_{wlr_{max}}^2, \\ 5/\delta_{wr_{max}}^2, 0.15/rpm_{wrt_{max}}^2, 0.15/rpm_{wrm_{max}}^2, 0.15/rpm_{wrr_{max}}^2 ] ) \quad (3.11)$$

Once the  $Q$  and  $R$  matrices are tuned, the LQR gain matrix  $K$  is found as follows using MATLAB's "lqr" command. Note that the overall LQR control law for tracking purposes is given in Equation 3.9.

$$K = \begin{bmatrix} 2.27 & 10.46 & 1.00 & 0.77 & 3.25 \\ 15686.37 & 82668.35 & 9360.23 & 4728.91 & 27539.76 \\ 8224.29 & 82668.35 & 4737.41 & 2521.32 & 27539.76 \\ -2.27 & 10.46 & -1.00 & -0.77 & 3.25 \\ -15686.37 & 82668.35 & -9360.23 & -4728.91 & 27539.76 \\ -8224.29 & 82668.35 & -4737.41 & -2521.32 & 27539.76 \\ 0.12 & -0.07 & 0.06 & 0.04 & -0.03 \\ -11980.37 & -7508.73 & -1384.20 & -5034.02 & -1839.17 \\ -7926.26 & -7508.73 & -779.40 & -3364.18 & -1839.17 \\ -3872.15 & -7508.73 & -174.60 & -1694.34 & -1839.17 \\ -0.12 & -0.07 & -0.06 & -0.04 & -0.03 \\ 11980.37 & -7508.73 & 1384.20 & 5034.02 & -1839.17 \\ 7926.26 & -7508.73 & 779.40 & 3364.18 & -1839.17 \\ 3872.15 & -7508.73 & 174.60 & 1694.34 & -1839.17 \\ & & -1.08 & -0.07 & 0.11 & 0.02 \\ & & 18670.24 & 485.27 & -1665.29 & 271.33 \\ & & 7994.42 & 485.27 & -706.38 & 271.33 \\ & & 1.08 & -0.07 & -0.11 & 0.02 \\ & & -18670.24 & 485.27 & 1665.29 & 271.33 \\ & & -7994.42 & 485.27 & 706.38 & 271.33 \\ & & -0.04 & 0.00 & 0.00 & 0.00 \\ & & 46544.64 & 639.89 & -4377.98 & 22.29 \\ & & 32232.74 & 639.89 & -3030.17 & 22.29 \\ & & 17920.83 & 639.89 & -1682.35 & 22.29 \\ & & 0.04 & 0.00 & 0.00 & 0.00 \\ & & -46544.64 & 639.89 & 4377.98 & 22.29 \\ & & -32232.74 & 639.89 & 3030.17 & 22.29 \\ & & -17920.83 & 639.89 & 1682.35 & 22.29 \end{bmatrix}$$

### 3.2.3.5 Analyzing the Closed Loop Dynamics

To analyze the closed loop dynamics, eigenvalues of the closed loop system (i.e.,  $A - BK$ ) are given in Figure 3.3.

As shown in Figure 3.2, open loop dynamics were unstable and also stable poles had low damping characteristics. Whereas, closed loop system poles given in Figure 3.3 are all stable and have much better transient response characteristics.



Pole	Damping	Frequency (rad/TimeUnit)	Time Constant (TimeUnit)
-7.79e+00 + 5.53e+00i	8.15e-01	9.55e+00	1.28e-01
-7.79e+00 - 5.53e+00i	8.15e-01	9.55e+00	1.28e-01
-5.23e+00	1.00e+00	5.23e+00	1.91e-01
-1.19e+00	1.00e+00	1.19e+00	8.39e-01
-6.29e-02	1.00e+00	6.29e-02	1.59e+01
-8.17e+00 + 4.63e+00i	8.70e-01	9.39e+00	1.22e-01
-8.17e+00 - 4.63e+00i	8.70e-01	9.39e+00	1.22e-01
-6.21e-01 + 5.80e-02i	9.96e-01	6.24e-01	1.61e+00
-6.21e-01 - 5.80e-02i	9.96e-01	6.24e-01	1.61e+00

Figure 3.3: Eigenvalues of the closed loop system for cruise condition.

To conclude, the linear analysis (i.e., the closed loop eigenvalues) shows that the LQR controller should have satisfactory transient response in cruise flight. In the next section, the performance of the LQR controller is tested via nonlinear simulations considering the basic maneuvers at cruise and the validity range of the linear controller.

### 3.2.3.6 Nonlinear Simulation Results

To check the performance of the LQR cruise controller, nonlinear simulation tests are performed. The tracking performance of the controller is analyzed at cruise condition for basic maneuvers such as climb, descent, and turns. In addition, the cruise controller is tested away from the cruise condition to observe the linear controller's validity range. It is noted that command generators are used to satisfy the LQR tracking controller's requirements explained in Section 3.2.3.4.

First, climb and descent maneuvers are tested at cruise commanding flight path angle (FPA) indirectly via applying pitch angle commands ( $\theta_{cmd}$ ). As given in Equation 3.6, the trim angle of attack and pitch angle was found as 4 degrees at 78 m/s cruise airspeed. To perform climb and descent maneuvers at cruise,  $\pm 5$  degree pitch angle commands are applied. At steady state, angle of attack transients disappear and 5 degree flight path angles are achieved as shown in 3.4. Control inputs are also given in Figure 3.5. As expected, rpm values increase and decrease to climb and descend, respectively. Moreover, minor adjustments are observed in tilt angles. Changes in

wing tilt angles are very small compared to the canards since the input weight matrix  $R$  is adjusted accordingly in the controller design (see Equation 3.11).

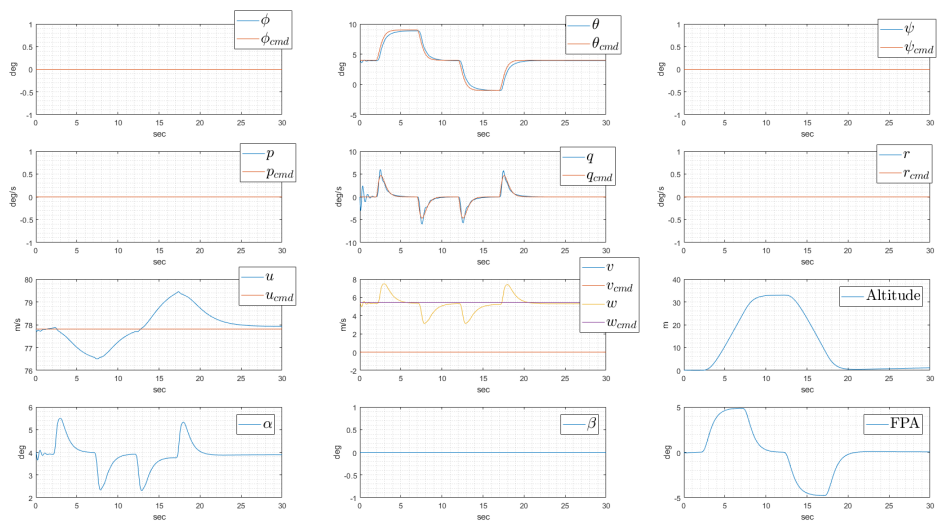


Figure 3.4: Tracking performance of the LQR cruise controller for climb and descent maneuvers at cruise, state response.

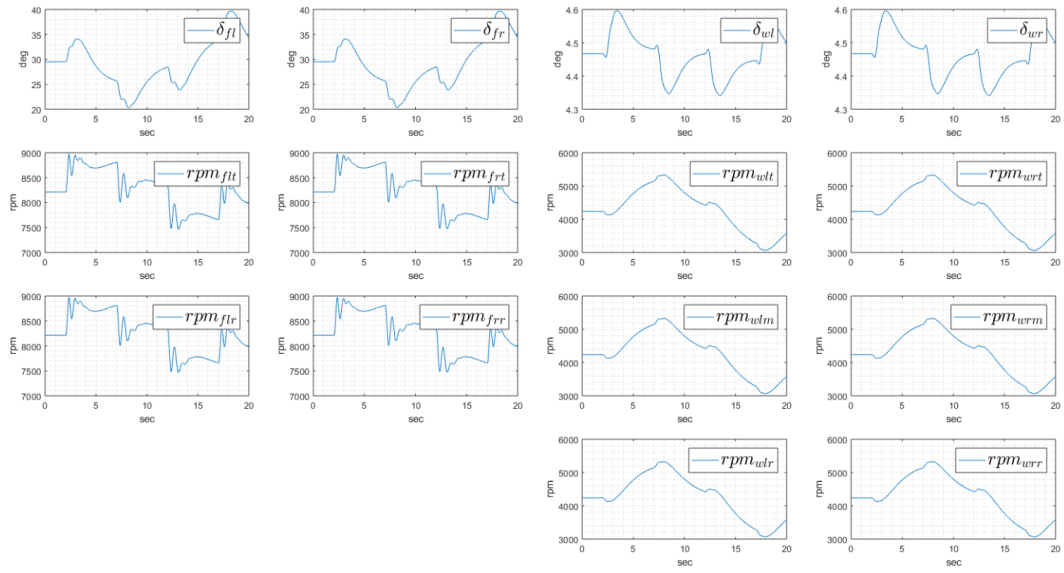


Figure 3.5: Tracking performance of the LQR cruise controller for climb and descent maneuvers at cruise, control inputs.

Coordinated turn maneuver at cruise conditions is also tested by commanding roll

angle and the corresponding yaw angle rate given as follows [86].

$$\dot{\psi}_{cmd} = \tan(\phi) g \cos(\theta) / V_{\infty} \quad (3.12)$$

Aircraft states and control inputs during the coordinated turn are given in Figures 3.6 and 3.7, respectively. Positive and negative 30 degree roll angle commands are applied at cruise condition. Aircraft tracks the roll angle and corresponding yaw rate commands as desired. Altitude loss is observed during the turn maneuvers. This is an expected result and can be improved by designing an outer loop controller that commands flight path angle accordingly. The aim of designing the linear LQR controller is to analyze the overall behavior of the aircraft. Therefore, outer loop controller is not designed for the LQR cruise controller. Regarding the control inputs during the turns, asymmetric control inputs are observed between the left and right side of the aircraft as expected (Figure 3.7).

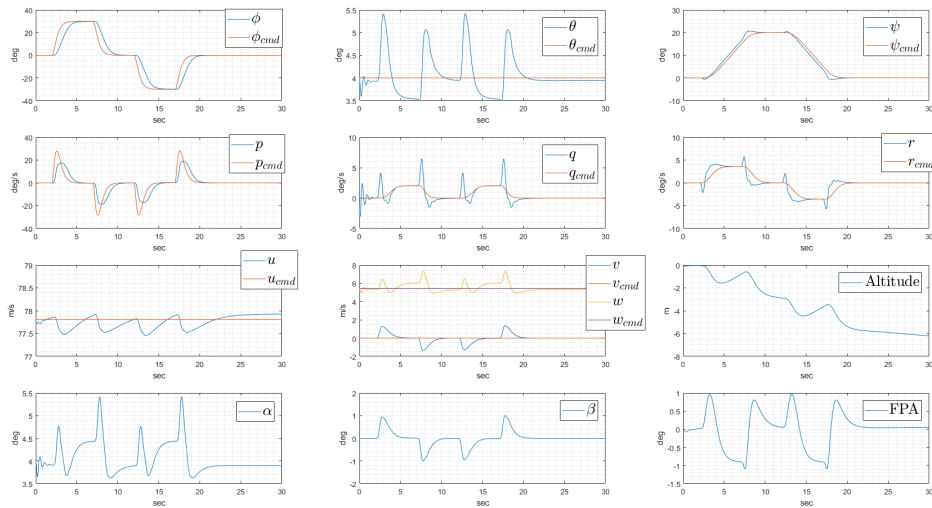


Figure 3.6: Tracking performance of the LQR cruise controller for coordinated turn maneuvers at cruise, state response.

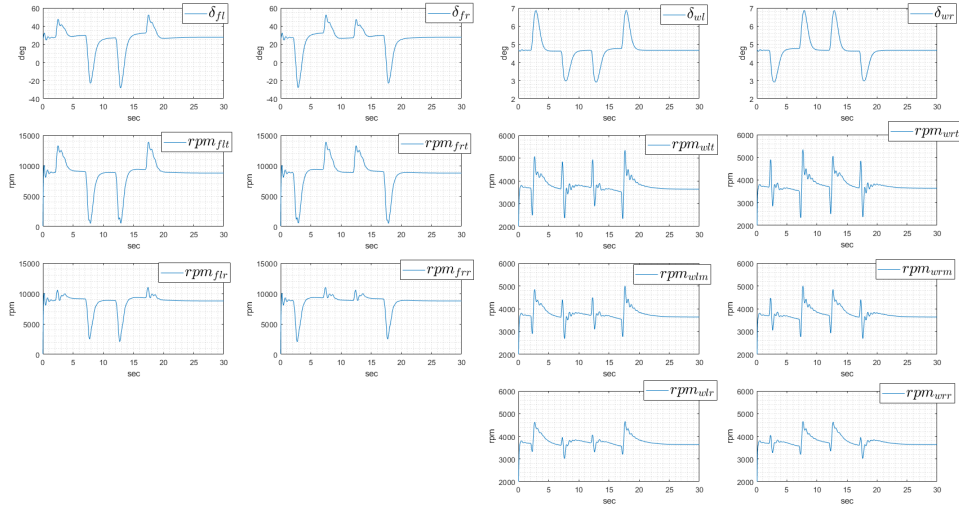


Figure 3.7: Tracking performance of the LQR cruise controller for coordinated turn maneuvers at cruise, control inputs.

To sum up, the LQR cruise controller’s performance is satisfactory considering the climb/descent and coordinated turn maneuvers at cruise condition.

*As mentioned previously, it is desired to analyze the LQR cruise controller’s validity away from the design condition. The aim of this analyze is to investigate the design effort of a unified flight controller via LQR-based linear control approach for the wide flight envelope of the air-taxi. LQR controller is designed at cruise condition (airspeed of 78 m/s) and it is expected to work properly near the trim condition. As illustrated in Section 2.1.1.2, there exist nonlinearities in the aerodynamic coefficients with respect to the airspeed for the forward flight model. Therefore, the LQR cruise controller is tested at high speed conditions to check the validity of the LQR cruise controller. To check the dependency of the controller with respect to the airspeed only, any other commands are not applied. Results given in Figures 3.8 and 3.9 show that when the airspeed is above 96 m/s, closed loop system shows unstable behavior and oscillations are observed both on the states and the actuator commands. To achieve satisfactory response at high speeds, it is required to redesign the LQR controller at high speed trim point. Considering also the transition between hover to cruise and visa-versa, it is required to design LQR controller at numerous trim points*

since nonlinearities in transition region are significant. Therefore, to cover the entire flight envelope, gain-scheduled design is inevitable for the studied air-taxi. It is also noted that, the flight dynamics model of the novel air-taxi generated in this thesis is a preliminary model, and some of the nonlinearities are not modeled due to high complexity (e.g., aero-propulsion couplings, ground effect, etc.). Therefore, considering a high fidelity flight dynamics model, it is expected that the gain-scheduling parameters would not be only for the airspeed, and additional scheduling will be required due to the severe nonlinearities especially in the transition regimes. Therefore, design of a unified flight controller via linear model-based approaches would require much more effort and performance may not be satisfactory due to the severity of nonlinearities.

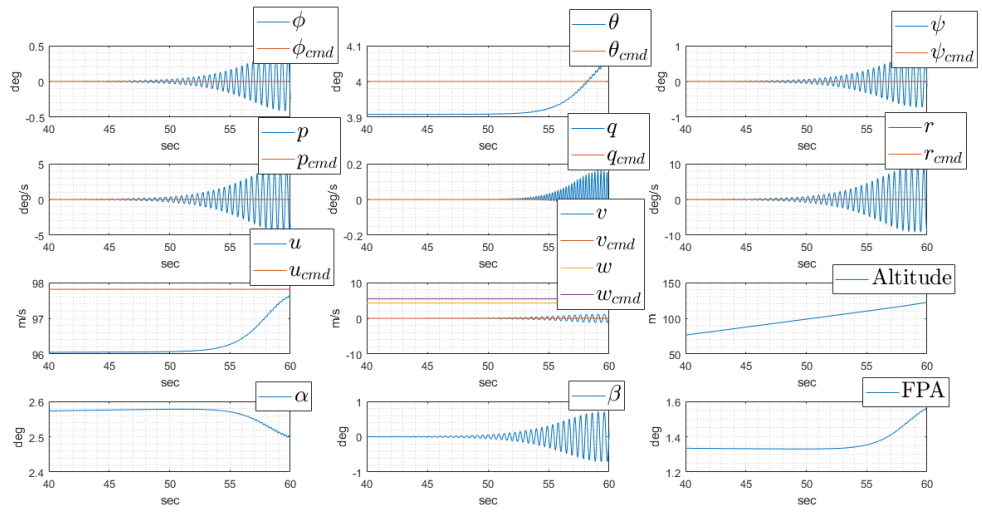


Figure 3.8: LQR cruise controller performance away from the cruise design/trim condition (18 m/s away from the cruise trim airspeed), state response.

### 3.2.4 Conclusion for the LQR based Unified Controller Design

To conclude, the LQR based cruise controller works as expected near the cruise design condition. However, considering the wide flight envelope of the aircraft, gain scheduling is required to design a unified controller that works for the entire flight envelope. Considering the severe nonlinearities of the flight dynamics model explained in Section 3.1, significant design effort is needed for the classical gain scheduled LQR design. Therefore, a nonlinear and less model dependent control approach is consid-

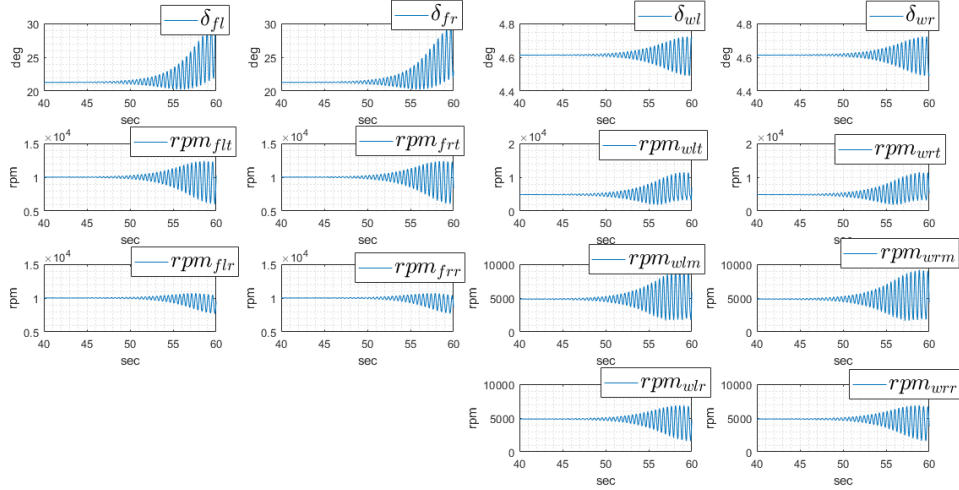


Figure 3.9: LQR cruise controller performance away from the cruise design/trim condition (18 m/s away from the cruise trim airspeed), control inputs.

*ered to be more advantageous compared to the linear and model-based approaches regarding the unified controller design.*

A nonlinear and sensor-based controller based on the emerging INDI approach is designed and verified in the next section. Moreover, a "Control Allocation(CA)" algorithm is integrated into the INDI controller considering the problems due to limited control authority and over-actuation (see Section 3.1 for details).

### 3.3 Unified Incremental Nonlinear Dynamic Inversion (INDI) Controller Design with Integrated Control Allocation (CA)

In this section INDI controller is designed considering the wide operational flight envelope of the eVTOL air-taxi (i.e., vertical takeoff, transition to forward flight, high speed forward flight/cruise, transition to hover flight and vertical landing). Then, CA is designed and integrated into the INDI controller taking into account the incremental approach. Once the unified flight controller (INDI+CA) is designed and implemented into the MATLAB simulation environment, the unified controller is tested via nonlinear simulations for several flight conditions. Disturbance rejection performance and sensitivity to model parameters are also analyzed. Finally, results are discussed and

concluding remarks are given about the overall characteristics of the designed controller. Before moving into the unified controller design, a literature review about the INDI and CA methods are given in the next section. *It is noted that the challenges regarding the unified controller design and the main contributions of the thesis have already discussed thoroughly in Section 3.1.*

### **3.3.1 Literature Review of the INDI and CA Methods**

Classical gain-scheduled flight control approach requires linearized aircraft models at several design points (i.e., the linearized trim conditions) [36, 76]. Depending on the severity of nonlinearities in aircraft dynamics, number of design points might increase significantly to cover the entire flight envelope [76]. Although gain-scheduling proved itself as a successful and reliable control approach for a wide range of air vehicles, controller performance may not be satisfactory for extreme flight conditions with significant nonlinearities (e.g., near stall or high angle of attack maneuvers) [36, 84, 76]. Nonlinear Dynamic Inversion (NDI) has emerged as an alternative to the classical gain-scheduling control approach in late 1980s [36, 53, 84, 60]. NDI use aircraft model to perform the feedback linearization, and theoretically it can handle all the modeled nonlinearities in a generalized framework [80]. NDI gives better performance compared to the classical gain-scheduling approaches especially in extreme flight conditions [84]. However, NDI is highly sensitive to modeling errors, and high-fidelity modeling might require considerable effort especially for the unique aircraft concepts like the one studied in this thesis [80, 65].

With the improvements in the sensor technology in recent years, incremental form of NDI called "Incremental Nonlinear Dynamic Inversion (INDI)" became popular, and emerged as an extension of the classical NDI approach [80, 78, 89, 43, 99, 37, 55]. INDI is the incremental form of NDI, but due to the nature of sensor-based approach it has considerably different characteristics compared to the NDI [80, 65]. *The basic difference and advantage of the INDI is replacing the model information with the sensor data to perform the dynamic inversion thanks to the time-scale separation principle [80, 97]. Acceleration estimations from the sensor data reflect the model information dynamically such that any unmodeled dynamics, including the disturbances*

*and failures, already included into the dynamic inversion [80, 97, 96]. Sensor-based approach of INDI makes it less model dependent so that the sensitivity to modeling errors is greatly reduced compared to the model-based classical NDI [80, 74, 55, 96]. INDI's reduced dependency on aircraft model is a crucial advantage, especially considering the flight control of a novel aircraft such as the topic of this study (i.e., a unique eVTOL air-taxi).*

INDI approach is dependent on the acceleration measurements that is in general used as translational acceleration  $(\dot{u}, \dot{v}, \dot{w})$  and rotational acceleration  $(\dot{p}, \dot{q}, \dot{r})$  feedback in the control loop [80]. Therefore, accurate estimation of acceleration from sensor data is crucial for the INDI controller [74, 80], and noise filtering is required in general to have better INDI controller performance [74, 82]. Another critical factor for the INDI controller is the data-synchronization [80]. In general, the filtering introduces delay in the loop that is also needed to be considered as part of the data-synchronization. Both the noise filtering and data synchronization are discussed in detail as part of the INDI controller design in Section 3.3.2.3.

As mentioned, INDI is a relatively new control approach and emerged in late nineties as an extension of the NDI [83, 20]. It has gained popularity in recent years thanks to the robustness properties since very low sensitivity to modeling errors and inherent robustness to disturbances/failures are quite promising characteristics [97, 74, 75]. In the beginning, INDI's less model dependent nature became the main focus of the research [83, 20, 31]. Then, INDI's sensitivity to sensor measurements and accurate estimation of acceleration feedback are studied in the following years [80, 74, 98]. Stability of INDI-based controllers which might encourage real time implementation of INDI are also investigated in literature [94, 98, 81, 74]. In a recent study, an analytical stability analysis is performed for an INDI-based controller, and stability margins are investigated considering the sample-time [94]. Another recent research focus on stability analysis of INDI controller that is specifically formulated without using the time-scale separation principle of INDI [98]. It can be concluded that, stability analysis of INDI-based controllers might gain attention in the following years since there is still room to investigate. Sensor based nature of INDI makes it questionable on real time application due to the noise and delay problems of the measurement system. At this point, research going on German Aerospace Center (DLR) is valuable since



they applied INDI control approach successfully on a large scale Cessna type aircraft [65, 43]. Another research project held in Delft University focus on the real time implementation of INDI on MAVs, and improved disturbance rejection characteristics of INDI are verified via flight tests [82]. There are also other works in literature showing the effectiveness of INDI based controllers via flight tests. [89, 79, 80]. Successful real-time implementations motivated the author to research on INDI based flight controller. Taking into account the flight control challenges defined in Section 3.1, the INDI method is considered as an effective approach to design the unified flight controller for the novel eVTOL air-taxi.

*As described in Section 3.1, another challenge for the unified flight controller design is allocation of the control authority properly considering the over-actuated system and highly coupled pure thrust vector control concept. In case of actuator saturation, it is critical to allocate the limited control authority accordingly to guarantee safe flight throughout the wide flight envelope. To resolve actuator saturation effectively, relation between control axis and control effectors need to be formulated. However, resolving the actuator saturation is more complex for the coupled thrust vector control compared to the conventional aircraft with inherently decoupled dynamics (i.e., aileron to roll axes, elevator to pitch axis, rudder to yaw axis) [47].*

For over-actuated systems, Control Allocation (CA) methods are used in literature to effectively allocate the control effort to redundant actuators [45]. A common approach is dividing regulation and allocation tasks such that a high level controller generates a virtual control effort in aircraft level (e.g., force & moment or acceleration commands) and a separate CA algorithm allocate the available control authority to generate the desired virtual control effort [47, 45].

In literature, CA approaches for different type of applications are described and compared in details [47, 63, 35, 28]. Simple methods such as explicit ganging, pseudo inverse, daisy chaining are easy to implement; however, their performance is not always satisfactory if actuator saturation (position or rate limits) are present [63]. On the other hand, defining the CA as an optimization problem is an effective way to handle actuator saturation [47, 63, 92, 91]. In real-time implementation, on-line optimization based iterative solution methods has been a questionable option considering

the hard certification requirements of the flight control software [35]. However, this view has changed thanks to the improvements in computer technology and more efficient algorithms [28]. Constrained optimization methods with fast solvers emerged as an effective way of handling actuator limits in CA problem [63, 28, 44]. A paper about optimization based CA methods gives a very detailed and useful discussion considering the real time application of optimization-based CA approaches in flight control systems [28]. The paper mainly focus on two optimization-based CA approach named "direct allocation" and "mixed optimization" [28]. The "mixed-optimization" formulation includes minimization of both the error between desired and achieved commands (i.e., the error minimization) and the control effort (i.e, the control minimization) [63, 28]. There are also "error-minimization" and "control-minimization" approaches which separates error and control minimization tasks [63, 28]. The "mixed-optimization" approach is used in this thesis since it covers both minimization tasks in the same formulation (see Section 3.3.2.7).

As described in Section 3.1, resolving actuator saturation is quite critical to satisfy stable flight for the wide flight envelope of the air-taxi. Therefore, CA is defined as a constrained optimization problem taking into account the CA literature survey given in the previous paragraph. CA is designed considering the incremental nature of the INDI controller and highly coupled pure thrust vector control approach.

Literature survey of the INDI and CA methods are given in this section focusing on the advantageous features of the INDI and chosen CA approach for our control problem. In the next section, the unified INDI+CA flight controller design will be given in detail, and the controller will be verified via nonlinear simulations for several test cases including full envelope flight control, disturbance rejection, sensitivity to model parameters, criticality of CA in case of actuator saturation, etc.

### **3.3.2 The Unified INDI+CA Controller Design**

INDI is incremental form of the nonlinear dynamic inversion. In this form, controller computes the control input increments at each time step using the system states at the previous time step [56]. The main difference between the NDI and INDI is that the INDI is a sensor-based approach and for this reason it is much more tolerant to mod-

eling errors and disturbances since model information is replaced with sensor data during the dynamic inversion [80]. INDI is based on time-scale separation principle which will be explained in details during the derivation. To illustrate the difference between the NDI and INDI the following example is given.

For example, to design an attitude controller via the classical NDI, angular accelerations are derived from the model and inverted to obtain the desired control inputs. In INDI, the same attitude controller is designed using angular acceleration measurements instead of accelerations derived from the model, and at each time step incremental control inputs are computed using the error between the desired and measured angular accelerations [80]. *In INDI, the dynamic inversion is based on sensor measurements instead of the model information. Therefore, model dependency is significantly reduced for the INDI controller. However, using sensor measurements in the dynamic inversion comes with other problems such as noise filtering, synchronization of time delays, etc. [50] which will be discussed throughout the derivation.*

In the following sections, first the control inputs will be defined specifically considering the unified controller structure. Then, the unified INDI controller will be formulated and designed. Finally, the CA algorithm will be designed and integrated into the INDI controller.

### **3.3.2.1 Definition of the Control Inputs**

Before going into the formulation of the INDI control law, control inputs used in the derivation are defined first. Our aim is controlling both rotational and translational channels in the same framework. To achieve this, an aircraft level virtual control input ( $v_{INDI}$ ) including the total forces and moments generated by the propulsion system is defined in Equation (3.13). Note that the full envelope flight control is achieved via pure thrust vector control which adjust the forces and moments generated by the propulsion system. The propulsion forces and moments are defined in the aircraft body axis in Equations 2.22 and 2.23. Therefore, it is easier to relate them with the thrust vector control also defined in the aircraft body axis (see Figure 3.10).

Although rpm and tilt angle are the physical actuator commands, thrust is used in-

stead of rpm for simplification since thrust and rpm are related by a constant (see Equation 2.12). Then, it is possible to decouple the thrust vector via defining the thrust components on the body axis ( $x_b$  and  $z_b$ ) as given in Figure 3.10. In Equation (3.13), the INDI control input ( $U_{INDI}$ ) is defined considering the decoupled thrust vector components on the aircraft body axis ( $x_b$  and  $z_b$ ).

$$\begin{aligned}
v_{INDI} &= [L_{prop} \quad M_{prop} \quad N_{prop} \quad Fz_{prop} \quad Fx_{prop}]^T \\
U_{INDI} &= [T_{x,fl} \quad T_{x,fr} \quad T_{x,wl} \quad T_{x,wr} \quad T_{z,fl} \quad T_{z,fr} \quad T_{z,wl} \quad T_{z,wr}]^T \\
v_{INDI} &= T_{v,INDI} U_{INDI} \\
U_{INDI} &= T_{v,INDI}^{-1} v_{INDI}, \quad T_{v,INDI}^{-1} = T_{v,INDI}^T (T_{v,INDI} T_{v,INDI}^T)^{-1}
\end{aligned}$$

$$\begin{bmatrix} L_{prop} \\ M_{prop} \\ N_{prop} \\ Fz_{prop} \\ Fx_{prop} \end{bmatrix} = \begin{bmatrix} 0 & 0 & 0 & 0 & \Delta y_{fl} & -\Delta y_{fr} & \Delta y_{wl} & -\Delta y_{wr} \\ 0 & 0 & 0 & 0 & \Delta x_{fl} & \Delta x_{fr} & -\Delta x_{wl} & -\Delta x_{wr} \\ \Delta y_{fl} & -\Delta y_{fr} & \Delta y_{wl} & -\Delta y_{wr} & 0 & 0 & 0 & 0 \\ 0 & 0 & 0 & 0 & -1 & -1 & -1 & -1 \\ 1 & 1 & 1 & 1 & 0 & 0 & 0 & 0 \end{bmatrix} \begin{bmatrix} T_{x,fl} \\ T_{x,fr} \\ T_{x,wl} \\ T_{x,wr} \\ T_{z,fl} \\ T_{z,fr} \\ T_{z,wl} \\ T_{z,wr} \end{bmatrix}$$

$$\begin{aligned}
\Delta x_{fl} &= 2.1m, \quad \Delta y_{fl} = (\Delta y_{flt} + \Delta y_{flr})/2 = (-1.1m - 0.5m)/2 = -0.8m \\
\Delta x_{fr} &= 2.1m, \quad \Delta y_{fr} = (\Delta y_{flt} + \Delta y_{flr})/2 = (1.1m + 0.5m)/2 = 0.8m \\
\Delta x_{wl} &= -0.85m, \quad \Delta y_{wl} = (\Delta y_{wlt} + \Delta y_{wlm} + \Delta y_{wlr})/2 = (-2.95m - 2.05m - 1.15m)/3 = -2.05m \\
\Delta x_{wr} &= -0.85m, \quad \Delta y_{wr} = (\Delta y_{wrt} + \Delta y_{wrm} + \Delta y_{wrr})/2 = (2.95m + 2.05m + 1.15m)/3 = 2.05m
\end{aligned}$$

(3.13)

Once the aircraft level virtual control input ( $v_{INDI}$ ) and the decoupled INDI control input ( $U_{INDI}$ ) are defined, it is required to formulate the transformation/mapping between these two control input vectors. The transformation matrix  $T_{v,INDI}$  is a function of lever arms only and given in Equation (3.13) (see Figures 3.11 and 3.10).

To reduce the number of control inputs, EDF sets are combined and defined as 4 sections named as front left ( $fl$ ), front right ( $fr$ ), wing left ( $wl$ ) and wing right ( $wr$ ), see Figure 3.11. With this simplification, in Equation (3.13), the y lever arms of each section represent the mean values of the individual lever arms given in Table 2.4;

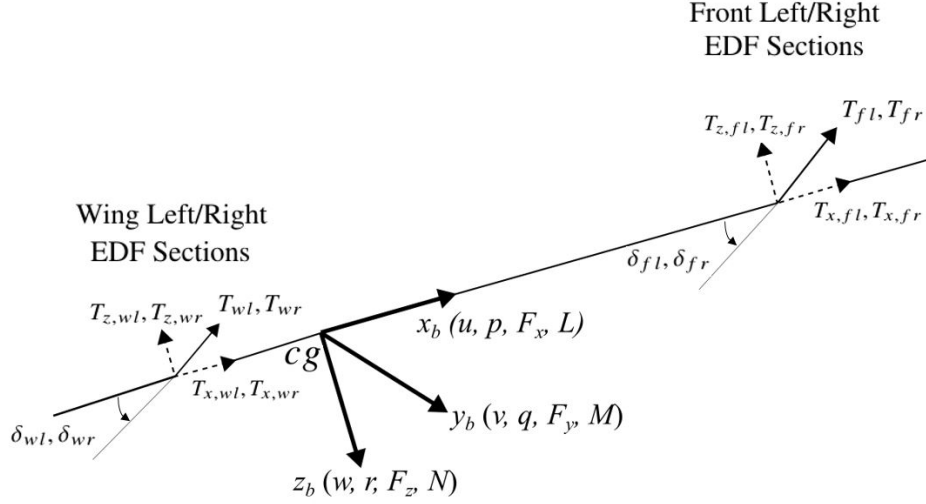


Figure 3.10: Thrust vectoring and control input visualization for the INDI controller, side-view of the aircraft.

whereas,  $x$  lever arms do not change. To sum up, only the basic geometry (i.e., the lever-arm information) is needed to generate the transformation matrix  $T_{v,INDI}$ .

It is also required to define the actuator level control inputs/commands which are the thrust ( $T$ ) and tilt angle ( $\delta$ ) commands for each EDF. In Equation (3.14), control inputs on actuator level ( $U$ ) is defined and relation between the decoupled INDI control input ( $U_{INDI}$ ) is given using the thrust vector control illustrated in Figure 3.10. In addition, it is desired to represent the actuator states considering the actuator dynamics defined in Section 2.2.4 (Figure 2.9).  $U_{act}$  is also defined in Equation (3.14) for this purpose. Note that the INDI controller's output on actuator level ( $U$ ) might be out of the actuator limits, defined in Table 2.5, which results in actuator saturation. In this case, the CA reallocates the limited control authority appropriately to guarantee stable flight taking into account the actuator limits. Separate definition of  $U$  and  $U_{act}$  are mainly used to analyze the CA performance (see Section 3.3.3.6).

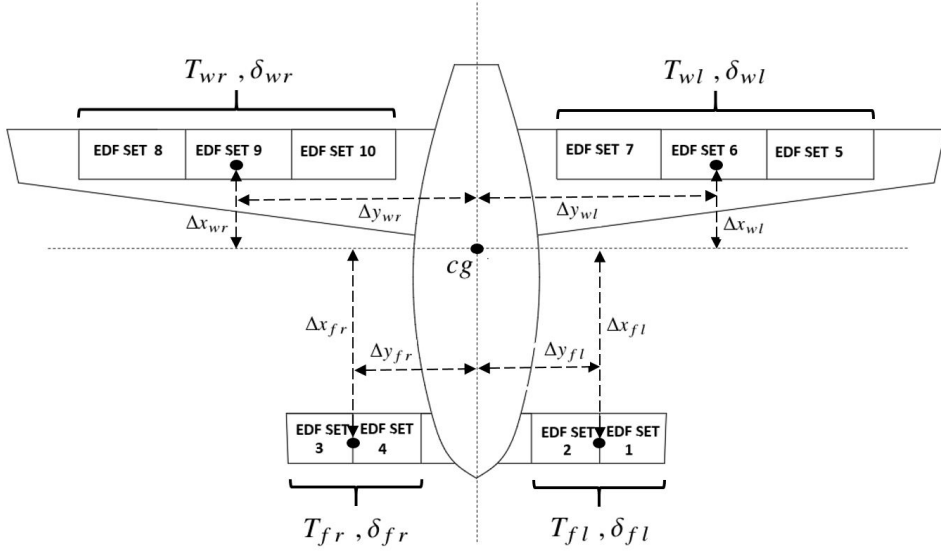


Figure 3.11: Combination of EDF sets to 4 sections: front left(*fl*), front right(*fr*), wing left(*wl*) and wing right(*wr*) for the INDI controller design, top-view.

$$T_x = \sin(\pi/2 - \delta) T$$

$$T_z = \cos(\pi/2 - \delta) T$$

$$T = \sqrt{T_x^2 + T_z^2}$$

$$U = \begin{bmatrix} T_{fl} & T_{fr} & T_{wl} & T_{wr} & \delta_{fl} & \delta_{fr} & \delta_{wl} & \delta_{wr} \end{bmatrix}^T \quad (3.14)$$

$$U_{act} = \begin{bmatrix} T_{fl,act} & T_{fr,act} & T_{wl,act} & T_{wr,act} & \delta_{fl,act} & \delta_{fr,act} & \delta_{wl,act} & \delta_{wr,act} \end{bmatrix}^T$$

### 3.3.2.2 Formulation of the INDI Control Law

In the previous section, the virtual, INDI and actuator level control inputs are defined. In this section, the incremental INDI control law will be formulated using the predefined control inputs.

First, the 6-DOF Equations of Motion (EOM) given in Equations (2.22) and (2.23) are rewritten in the following form.

$$\begin{bmatrix} \dot{u} \\ \dot{v} \\ \dot{w} \end{bmatrix} = 1/m (F_{aero}^b + F_{grav}^b) - \begin{bmatrix} p \\ q \\ r \end{bmatrix} \times \begin{bmatrix} u \\ v \\ w \end{bmatrix} + 1/m \begin{bmatrix} F_{x_{prop}} \\ 0 \\ F_{z_{prop}} \end{bmatrix} \quad (3.15)$$

$$\begin{bmatrix} \dot{p} \\ \dot{q} \\ \dot{r} \end{bmatrix} = J^{-1}(M_{aero}^b - \begin{bmatrix} p \\ q \\ r \end{bmatrix} \times J \begin{bmatrix} p \\ q \\ r \end{bmatrix}) + J^{-1} \begin{bmatrix} L_{prop} \\ M_{prop} \\ N_{prop} \end{bmatrix} \quad (3.16)$$

The propulsion forces and moments are explicitly written to insert the virtual control input ( $v_{INDI}$ ) into the EOM. Based on the virtual control input definition given in Equation (3.13), it is possible to define the EOM in a control-affine form by rewriting Equations (3.15) and (3.16). Since our aim is tracking attitude and velocity commands, state vector ( $x$ ) includes the body angular accelerations and linear accelerations on the body x and z directions. As mentioned previously, linear acceleration on the body y direction is not included since propulsion force is not directly generated on this direction. In Equation (3.17),  $f(x)$  represents the aerodynamic forces and moments, gravitational force and also the cross coupling terms. To sum up, the nonlinear EOM is rewritten in control-affine form as follows.

$$\begin{aligned} \dot{x} &= f(x) + g \cdot v_{INDI} \\ x &= [p \quad q \quad r \quad w \quad u]^T \\ v_{INDI} &= [L_{prop} \quad M_{prop} \quad N_{prop} \quad F_{z_{prop}} \quad F_{x_{prop}}]^T \\ g &= \begin{bmatrix} 1/I_x & 0 & 0 & 0 & 0 \\ 0 & 1/I_y & 0 & 0 & 0 \\ 0 & 0 & 1/I_z & 0 & 0 \\ 0 & 0 & 0 & 1/m & 0 \\ 0 & 0 & 0 & 0 & 1/m \end{bmatrix} \end{aligned} \quad (3.17)$$

Then, the first-order Taylor series approximation of Equation (3.17) is written. Taylor

series approximation is based on the previous values of states and virtual control inputs which are represented with a subscript "0" in the following equation.

$$\begin{aligned} \dot{x} \approx \dot{x}_0 + \frac{\partial[f(x)+g \cdot v_{INDI}]}{\partial x} \Big|_{x=x_0, v_{INDI}=v_{INDI,0}} (x - x_0) + \\ \frac{\partial[f(x)+g \cdot v_{INDI}]}{\partial v_{INDI}} \Big|_{x=x_0, v_{INDI}=v_{INDI,0}} (v_{INDI} - v_{INDI,0}) \end{aligned} \quad (3.18)$$

*The key assumption of the INDI control is the time scale separation principle [50], which assumes that the change in states are very small compared to the change in control inputs in a single time-step. This assumption is based on very small time increments and fast actuator dynamics [50, 80, 75]. According to the actuator dynamics defined in Section 2.2.4, EDFs have very fast rpm/thrust dynamics based on the wind-tunnel data. In addition, the tilting dynamics is assumed to be fast considering very small EDF weight/size (see Table 2.3). Considering the fast actuator dynamics of EDFs, it is reasonable to assume that if time-step is small enough, then the change in states would be negligible compared to the change in control inputs. Regarding the small time-step requirement, simulation tests are performed at 100 Hz which is a common approach for the closed loop flight dynamics simulations. 100 Hz cycle/update rate is achievable considering the current flight control boards and sensors [12, 48, 69, 101]. To conclude, the time-scale separation principle of the INDI approach fits well to the control problem of novel eVTOL air-taxi.*

Applying the time-scale separation principle simplifies the Taylor series expansion given in Equation (3.18) as follows.

$$\begin{aligned} \dot{x} \approx \dot{x}_0 + g \cdot (v_{INDI} - v_{INDI,0}) = \dot{x}_0 + g \cdot \Delta v_{INDI} \\ \text{with assumption } (x - x_0) \ll (v_{INDI} - v_{INDI,0}) \end{aligned} \quad (3.19)$$

Then, the required virtual control input increment at each time step is obtained by inverting Equation (3.19).

$$\Delta v_{INDI} = g^{-1}(\dot{x}_{req} - \dot{x}_0) \text{ , where } \dot{x} = \dot{x}_{req} \quad (3.20)$$



According to Equation (3.20), the incremental virtual control input  $\Delta v_{INDI}$  depends on the following terms.

- $\dot{x}_0$  which is the state derivatives obtained from the current and previous values of sensor outputs.
- $\dot{x}_{req}$  representing the required state derivatives which are calculated based on the model independent linear controller in the next section.
- $g^{-1}$  which is the inverse of  $g$  matrix that is function of mass and inertia only (see Equation (3.17)).

INDI control input increment ( $\Delta U_{INDI}$ ) is obtained in Equation (3.21) using the inverse of transformation matrix ( $T_{v,INDI}$ ) mapping the virtual and INDI control inputs given in Equation (3.13). Since  $T_{v,INDI}$  is not full rank, inverse is found via pseudo-inverse approach. Note that the transformation from the virtual to INDI control input only uses lever arm information which is purely geometric. Lever arm information is a direct input to the controller, and it can be updated in case of detected failures or any other corrections.

$$\begin{aligned}\Delta U_{INDI} &= T_{v,INDI}^{-1} \Delta v_{INDI} \\ T_{v,INDI}^{-1} &= T'_{v,INDI} (T_{v,INDI} T'_{v,INDI})^{-1}\end{aligned}\tag{3.21}$$

*At this point, it can be seen that the INDI control law use sensor outputs to replace the model information. That is why INDI is a sensor-based control approach, and only required model information is the  $g$  and  $T_{v,INDI}$  matrices containing only the mass, inertia and lever arm information. This is the main advantage of INDI compared to the classical NDI which is much more dependent on the aircraft model due to the model-based dynamic inversion.*

Combining Equations (3.20) and (3.21), the INDI control input increment ( $\Delta U_{INDI}$ ) is defined more explicitly as follows.

$$\Delta U_{INDI} = T_{v,INDI}^{-1} g^{-1} (\dot{x}_{req} - \dot{x}_0)\tag{3.22}$$

Equation (3.22) gives the INDI control input increment at each time step. It is required to use previous time INDI control input ( $U_{INDI,0}$ ) to find the overall INDI control input ( $U_{INDI}$ ) given in the following equation.

$$U_{INDI} = U_{INDI,0} + \Delta U_{INDI} \quad (3.23)$$

$U_{INDI,0}$  includes the effects of actuator dynamics since it is taken from the previous time step. It is reminded that  $\dot{x}_0$  represents the rotational and translational acceleration obtained from the sensor measurements. A noise filter is applied to the sensor outputs to improve the controller's performance. To satisfy the data-synchronization, noise filter applied to the sensor measurements are also applied to the INDI controller output (see Figure 3.12). Details of the noise filtering and data synchronization are explained in the next section.

### 3.3.2.3 Filtering Sensor Noise & Data Synchronization

The incremental INDI control law is given in Equation (3.22), and  $\dot{x}_0$  represents the state derivatives (i.e., the rotational and translational accelerations) obtained from the sensor measurements. As explained previously, the main difference and advantage of INDI is replacing the sensor measurement with the model information (i.e., the nonlinear flight dynamics model) to perform the dynamic inversion. This significantly minimizes the model dependency of dynamic inversion and makes the INDI more robust against the modeling errors compared to the NDI. However, using sensor measurements to calculate the state derivatives requires filtering of the noise. The following low-pass filter is applied on sensor measurements to reduce the noise level. It is reminded that the sensor dynamics is modeled using the data of a MEMS IMU sensor and the details are given in Section 2.3.

$$H_f = \frac{\omega_{n_f}^2}{s^2 + 2\zeta_f\omega_{n_f}s + \omega_{n_f}^2} \quad (3.24)$$

The parameters of the low-pass filter is taken from a study focusing on INDI-based controller design [56]. The natural frequency ( $\omega_{n_f}$ ) is 80 rad/s, and the damping ratio

$(\zeta_f)$  is equal to 1. Based on the simulation results given in Section 3.3.3, adjusting the parameters of the noise filter is not required to achieve the desired controller performance. Therefore, it can be concluded that the designed INDI controller is not highly sensitive to the noise filter design. On the other hand, performance might be improved with better filter characteristics which is not the focus of this study.

The low-pass filter comes with additional delay in the loop. Therefore, synchronization of the signals becomes critical [80]. To achieve the synchronization of the control inputs, the same noise filter is also applied to the INDI control input given in Equation (3.23). By this way the data-synchronization problem is resolved which is also illustrated in the high level block diagram of the overall controller given in Figure 3.12.

### 3.3.2.4 Linear Controller: Required State Derivatives

Based on Equation (3.22), the required state derivatives ( $\dot{x}_{req}$ ) can be considered as the reference/desired condition in the incremental control law. Required state derivatives can be generated based on the kinematic relations given in Equation 2.24. Then, the required state derivatives are obtained as follows using a PD (Proportional Derivative) linear controller structure considering the state vector defined in Equation (3.17).

$$\left. \begin{aligned} \dot{x}_{req} &= \begin{bmatrix} \dot{p}_{req} & \dot{q}_{req} & \dot{r}_{req} & \dot{w}_{req} & \dot{u}_{req} \end{bmatrix}^T \\ \dot{p}_{req} &= (\phi_{cmd} - \phi)K_\phi + (\dot{\phi}_{cmd} - \dot{\phi})K_{\dot{\phi}} \\ \dot{q}_{req} &= (\theta_{cmd} - \theta)K_\theta + (\dot{\theta}_{cmd} - \dot{\theta})K_{\dot{\theta}} \\ \dot{r}_{req} &= (\psi_{cmd} - \psi)K_\psi + (\dot{\psi}_{cmd} - \dot{\psi})K_{\dot{\psi}} \\ \dot{w}_{req} &= (w_{cmd} - w)K_w + (\dot{w}_{cmd} - \dot{w})K_{\dot{w}} \\ \dot{u}_{req} &= (u_{cmd} - u)K_u + (\dot{u}_{cmd} - \dot{u})K_{\dot{u}} \end{aligned} \right\} \quad (3.25)$$

*Note that the linear controller design does not depend on the aircraft model and only uses the kinematic relations. Therefore, tuning of the linear controller is quite*

straightforward and does not require any gain-scheduling to cover the wide flight envelope of the air-taxi. The linear controller can be considered as an outer loop controller that generates the reference acceleration commands to the inner loop INDI controller. To conclude, the model independent characteristics of the INDI controller is maintained in the outer loop linear controller design.

The Euler angle and body velocity commands used in Equation (3.25) are generated as follows using a command generator.

$$\left. \begin{aligned}
 \phi_{cmd} &= \phi_{cmd,manual} + \phi_{cmd,nav,hover} \\
 \text{with, } \phi_{cmd,nav,hover} &= (v_{cmd} - v)K_v + (\dot{v}_{cmd} - \dot{v})K_{\dot{v}} \\
 \theta_{cmd} &= \theta_{cmd,manual} + \theta_{cmd,fpa} \\
 \psi_{cmd} &= \psi_{cmd,manual} + \psi_{cmd,coord,turn} \\
 w_{cmd} &= w_{cmd,manual} + w_{cmd,nav,hover} + w_{cmd,fpa} \\
 \text{with, } w_{cmd,nav,hover} &= (h_{cmd} - h)K_h + (\dot{h}_{cmd} - \dot{h})K_{\dot{h}} \\
 u_{cmd} &= u_{cmd,manual} + u_{cmd,fpa}
 \end{aligned} \right\} \quad (3.26)$$

Details of the command generation function will be given in the next section. In this section, generation of the navigation commands will be explained briefly.

Equation (3.25) does not include  $\dot{v}_{req}$  which is related to the side-motion. As mentioned previously, EDFs do not directly generate forces in the body y direction. However we want to control the aircraft in 6-DOF. Controlling the side-motion (y position) is performed via generating navigation command in roll angle ( $\phi_{cmd,nav,hover}$ ) at low speed using the feedback in body y-velocity ( $v$ ).  $\phi_{cmd,nav,hover}$  is limited to  $\pm 30$  degrees to avoid rpm/thrust saturation due to large bank angle commands at low speeds. At high speed forward flight, it is possible to generate manual roll angle command ( $\phi_{cmd,manual}$ ) and the corresponding yaw angle command ( $\psi_{cmd,coord,turn}$ ) to perform the coordinated turn (see Equation 3.12).

Similarly, to control the altitude ( $h$ ) at low speed, the vertical velocity command

$w_{cmd,nav,hover}$  is generated using the feedback in altitude. To control the flight path angle ( $\gamma$ ) and also angle of attack ( $\alpha$ ) at high speed, combination of  $\theta_{cmd,fpa}$ ,  $w_{cmd,fpa}$ ,  $u_{cmd,fpa}$  is commanded considering the relations given in Equation (2.26).

As mentioned previously, the linear controller is based on the kinematic relations and does not depend on the aircraft model. Therefore, tuning of the controller is simply performed and the controller gains are given Tables 3.2 and 3.3.

Table 3.2: Linear controller gains.

Gain	Value	Gain	Value	Gain	Value	Gain	Value	Gain	Value
$K_\phi$	3	$K_\theta$	3	$K_\psi$	1.5	$K_w$	1.5	$K_u$	1.5
$K_{\dot{\phi}}$	5	$K_{\dot{\theta}}$	5	$K_{\dot{\psi}}$	3	$K_{\dot{w}}$	0.5	$K_{\dot{u}}$	0.5

Table 3.3: Linear controller gains for the navigation commands.

Gain	Value	Gain	Value
$K_h$	0.5	$K_v$	5
$K_{\dot{h}}$	1	$K_{\dot{v}}$	3

In this Section, the required state derivatives ( $\dot{x}_{req}$ ) are obtained using a linear PD controller structure and these derivatives are used in the incremental control law given in Equation (3.22) as the reference/desired state conditions. The linear controller uses several types of commands (defined in Equation 3.26) considering the wide flight envelope of the air-taxi. In the next section, the command generator function will be explained briefly.

### 3.3.2.5 Command Generator

The command generator is designed considering the unified controller design for the full flight envelope of the air-taxi. The main formulation for the command generation is given in Equation 3.26. In this section, details will be provided considering the commands at different flight conditions, mainly blending of the commands between the low speed hover flight and high speed forward flight.

As mentioned in Section 3.3.2.4, to control the side-motion, a roll angle command named  $\phi_{cmd,nav,hover}$  is generated at low speed flight.  $\phi_{cmd,nav,hover}$  is valid until 20 m/s ground speed since side-motion is directly related to the bank angle at low speeds. Similarly, to control the altitude at low speeds, a vertical speed command ( $w_{cmd,nav,hover}$ ) is generated.  $w_{cmd,nav,hover}$  is effective until 50 m/s airspeed. Above 50 m/s airspeed, flight path angle is commanded via applying a combination of commands. Combined pitch angle and body velocity commands,  $\theta_{cmd,fpa}$ ,  $w_{cmd,fpa}$ ,  $u_{cmd,fpa}$  are applied at high speeds to control the flight path angle and also the angle of attack indirectly.

Moreover, after a certain airspeed it is desired to perform coordinated turns and this requires a yaw rate command given in Equation (3.12).  $\psi_{cmd,coord,turn}$  represents the corresponding yaw angle command required for the coordinated turn. The coordinated turn command is effective above 20 m/s airspeed.

Manual commands defined in Equation 3.26 are the direct commands that can be applied manually without restrictions on the flight regime. Several simulation tests are performed using the manual commands. For example, transition between hover and forward flight is achieved by manually applying body x-velocity command  $u_{cmd>manual}$ .

Command generator is also used to smooth and limit the commands. Second order transfer functions and saturation blocks are included to generate the commands considering the desired dynamics. Blending of the commands for different flight conditions are performed satisfying the smooth transition of commands (i.e., discontinuities are avoided).

### 3.3.2.6 Overall INDI Controller Structure

Formulation of the INDI controller is explained in the previous sections and the incremental control law is given in Equation 3.22. Moreover, the overall INDI control law used in simulations is given in Equation 3.23, which is found by adding the incremental control law to the output of the INDI controller at the previous time step. The overall block diagram of the INDI controller is illustrated in Figure 3.12.

First, the command generator block outputs the total commands defined in Equation

3.26, considering the smoothing and desired command dynamics. Then, the linear controller generates the required accelerations ( $\dot{x}_{req}$ ) using the error between the commands and sensor outputs (see Equation (3.25)). Note that the linear controller use kinematic relations only and independent of the aircraft dynamic model.

The critical part of the INDI controller design is estimating accelerations (i.e., the state derivatives,  $\dot{x}_0$ ) which replace the aircraft model information in the dynamic inversion. To estimate the angular and translational accelerations, gyroscope and accelerometer measurements are used, respectively. The sensor dynamics included into the simulation model is explained in Section 2.3. Gyroscope and accelerometer measurements are filtered by a low pass filter ( $H_f$ , Equation 3.24) and the state derivatives are calculated.

At this point, it is important to remember that the INDI controller is sample based and synchronization is very important due to the incremental dynamic inversion at each time step. To satisfy synchronization of the control input and sensor measurements, the filter  $H_f$  used for acceleration estimations is also applied to the control inputs (Figure 3.12,  $U_{INDI}$ ). Once the accelerations are estimated, the required accelerations and estimated accelerations are fed into the INDI controller to generate the incremental control input  $\Delta U_{INDI}$ .

According to Figure 3.12,  $\Delta U_{INDI}$  is calculated using the following information (see Equation 3.22).

- inverse of matrix  $T_{v,INDI}$  which contains only the lever arm information
- inverse of  $g$  matrix which contains only the mass and inertia information
- error between the required accelerations ( $\dot{x}_{req}$ ) and estimated accelerations ( $\dot{x}_0$ ).

*To conclude, the only modeling dependency of the INDI controller are the mass, inertia and lever arms (mainly the geometry information) of the aircraft. The rest of the modeling information is replaced with sensor data and this is the main advantage of the INDI approach. If the time scale separation principle explained in Equation (3.18) is valid, then it is possible to perform dynamic inversion incrementally using the acceleration estimations. The inherent robustness to modeling errors is verified*

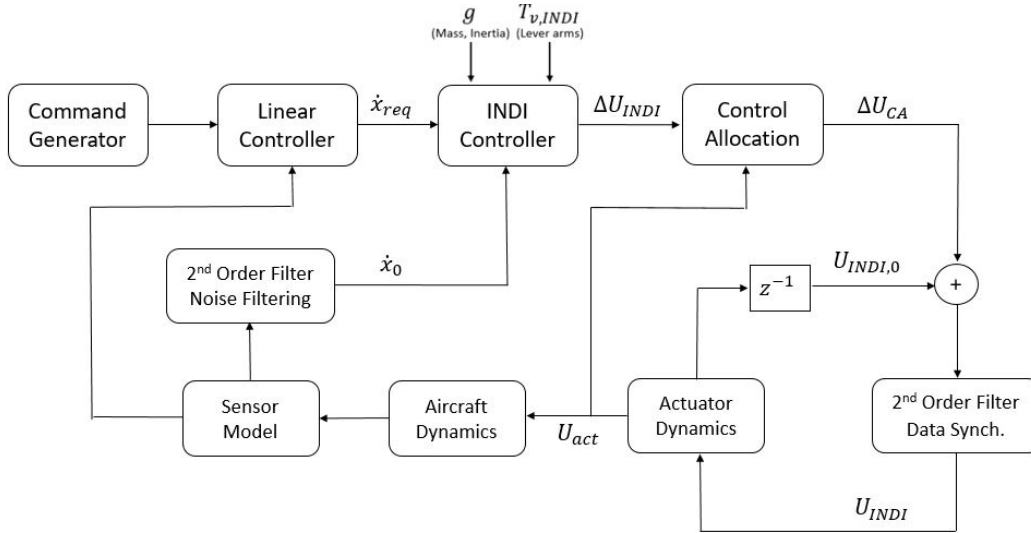


Figure 3.12: High level block diagram of the INDI controller with integrated CA.

via nonlinear simulations applying error in the drag coefficient, see Section 3.3.3.7.

As shown in Figure 3.12, the INDI controller calculates control input increments at each time step and this incremental value is added to the previous time control input ( $U_{INDI,0}$ ) to obtain the overall control input  $U_{INDI}$ .

CA block is also illustrated in Figure 3.12. As mentioned in Section 3.1, CA has a vital role of allocation of the limited control authority properly in case of actuator saturation. An optimization based CA algorithm is designed and integrated into the INDI controller. Details of the CA design is given in the next section.

### 3.3.2.7 Control Allocation Design & Integration into the INDI controller

As mentioned in Section 3.1, the system is over-actuated and the aircraft use pure thrust vector control which is highly coupled. Therefore, the CA problem in case of actuator saturation becomes more complicated since a direct relation between control channels/axis and control effectors/actuators does not exist. In conventional aircraft with primary control surfaces elevator, aileron and rudder, it is a common method to decouple the aircraft dynamics in the longitudinal and lateral channels. Then, the actuator saturation related problems can be resolved easily using the decoupled dy-



*namics and classical saturation resolving methods (e.g. the anti-wind up schemes) [47]. For example, elevator is directly related to the longitudinal pitch dynamics and aileron/rudder are related to the lateral roll and yaw dynamics, respectively. Then, saturation of elevator is related to the pitch dynamics-commands and the same approach is valid for roll/yaw dynamics if small couplings between roll and yaw motion are neglected. To conclude, applying the classical saturation resolving methods are not straightforward to implement for the over-actuated and highly coupled pure thrust vector control of the studied air-taxi.*

Proper design of CA becomes critical for specific flight conditions that result in limited control authority (i.e., the actuator saturation). CA must guarantee stable flight via prioritizing rotational channels when the INDI controller generates actuator commands that are beyond the physical actuator limits. *To illustrate, assume that the pilot is applying a vertical speed command to climb at hover flight. Vertical speed command at hover is generated by increasing thrust/rpm at all EDFs. Then, a strong disturbance/wind-gust occurs, and banks the air-taxi significantly. To reject the disturbance on bank angle, some of the EDFs increase rpm further and eventually hit the maximum rpm limit. If the pilot still applies the vertical speed command, then available control authority will not be sufficient to both track the vertical speed command and reject the bank angle disturbance. In other words, there will be an error between the INDI controller's actuator commands and physically achieved actuator states (see  $U$  and  $U_{act}$  in Equation 3.14). A good pilot might realize the problem and release the vertical speed command to provide control authority. Then, actuators will not hit the rpm limit and control authority will be available to reject the bank angle disturbance. The pilot instinctively prioritizes rotational control over the translational control. However, this puts more burden on the pilot and a systematic way of handling actuator saturation is desired considering the wide flight envelope. Considering the transition regions, thrust vector control is highly coupled and the pilot may not give the correct decision to resolve the actuator saturation and guarantee stable flight for all cases. This example scenario is tested via nonlinear simulations in Section 3.3.3.6 to verify the CA design. It is observed that the CA significantly improves the disturbance rejection characteristics and plays a vital role of guaranteeing stable flight in case of limited control authority.*

Literature review about the CA approaches are given in Section 3.3.1. A constrained optimization based CA algorithm is designed since performance of the simple CA methods are not satisfactory in case of actuator saturation [63]. The constrained optimization problem is defined as follows in "mixed-optimization" formulation such that the cost function includes both the "error-minimization" and the "control-minimization" [63, 28]. The active-set algorithm described in [44] is used to solve the optimization problem (see Appendix A).

$$\left. \begin{array}{l}
 \text{minimize} \\
 \Delta U_{CA} \\
 \text{subject to} \\
 \text{with initial conditions}
 \end{array} \right\} \begin{array}{l}
 \Delta U_{CA} = [\Delta T_{x,fl} \quad \Delta T_{x,fr} \quad \Delta T_{x,wl} \quad \Delta T_{x,wr} \quad \Delta T_{z,fl} \quad \Delta T_{z,fr} \quad \Delta T_{z,wl} \quad \Delta T_{z,wr}]^T \\
 J(\Delta U_{CA}) = \|W_u (\Delta U_{CA} - \Delta U_{des})\|^2 + \gamma \|W_v (T_{v,INDI} \cdot \Delta U_{CA} - \Delta v_{INDI})\|^2 \\
 \Delta U_{CA,min} < \Delta U_{CA} < \Delta U_{CA,max} \\
 \Delta U_{INDI}
 \end{array} \quad (3.27)$$

Since INDI is an incremental controller, cost function  $J(\Delta U_{CA})$  is also written in incremental form.  $\Delta v_{INDI}$  is incremental form of the virtual control input defined in Equation (3.17) and  $W_v$  is the state weight matrix that is adjusted accordingly to prioritize specific channels. Therefore, the second part of the cost function is related to the controller's tracking performance of virtual force/moment commands (i.e., the "error-minimization" [63, 28]). If more weight is put on the first and second diagonal entries of  $W_v$  matrix, then more control effort will be applied to minimize the error between desired and obtained roll and pitch moments ( $L, M$ ). State weight matrix is chosen as  $W_v = \text{diag}(1000, 1000, 100, 50, 50)$ . The priority order is as follows: roll/pitch dynamics, yaw dynamics and horizontal/vertical translational dynamics. The prioritization order might differ in different flight conditions. For example, in hover keeping the aircraft heading is not considered more important than keeping the altitude or in cruise keeping the aircraft heading might be more important during coordinated turns compared to losing altitude since the aircraft is directionally unstable at high speeds due to negative  $C_{n\beta}$  value (see Equation (2.1)). The selected  $W_v$  matrix represents a generalized prioritization order and the same matrix is used in the verification tests given in Section 3.3.3. The first part of the cost function is related to the "control-minimization" [63, 28].  $\Delta U_{des}$  represents the desired control input increment and it is taken as zero ( $\Delta U_{des} = \text{zeros}(8, 1)$ ) to find solutions close to the INDI controller's

output. In other words, discontinuities in the control input commands are avoided via defining the desired control input increment vector as zero. Also note that the initial search point for the algorithm is the output of the INDI controller  $\Delta U_{INDI}$  given in Equation (3.22).  $W_u$  is the control input weight matrix and it is used to put more control effort on specific control channels such as applying more rpm/thrust control instead of tilting the EDFs to achieve desired states or putting more effort on the wing EDFs compared to front EDFs, etc.. For the sake of simplicity, weights are not applied on specific control channels and  $W_u$  matrix has diagonal elements of 1,  $W_u = diag(1, 1, \dots, 1)$ . Finally, the value of  $\gamma$  is chosen as 0.0001 and it is used to tune the cost function if needed.

According to Equation 3.27, the algorithm minimizes the cost function while satisfying the constraints on control input increment. Therefore, the lower and upper bounds ( $\Delta U_{CA,min}$ ,  $\Delta U_{CA,max}$ ) need to be evaluated at each time step. Since the incremental control input ( $\Delta U_{CA}$  in Equation 3.27) is decoupled on x and z directions, the lower and upper bounds need to be evaluated considering the decoupled INDI control input. In other words, the physical actuator limits (i.e., the rpm and tilt angle limits) are mapped into the incremental decoupled thrust limits. Algorithm 1 is written to perform the mapping. The algorithm evaluates the remaining control authority (i.e.,  $\Delta U_{CA,min}$  and  $\Delta U_{CA,max}$ ) considering the thrust vector control given in Figure 3.10 (Equation 3.14). In the algorithm,  $\delta_{i,min}$ ,  $T_{i,min}$  and  $\delta_{i,max}$ ,  $T_{i,max}$  are the physical actuator limits defined in Table 2.5, and  $T_{x,i,act}$ ,  $T_{z,i,act}$  represent the x and z components of the thrust vector considering the actuator limits. *To sum up, constraints of the CA problem are evaluated considering the incremental and decoupled INDI formulation. Mapping the physical actuator limits to the decoupled incremental thrust limits is the most crucial step of the CA integration into the INDI structure.*

The CA problem is solved online at each time step with 100 Hz (0.01 sec) cycle time. To limit the computational effort, maximum iteration number is set to 50. Verification of the INDI+CA unified controller is performed via nonlinear simulations given in the next section. Simulations are performed on a 1.8 Ghz Intel Core CPU computer. As a common fact, online optimization is not a desired option in flight control for the real-time implementation considering the hard certification requirements. A detailed analysis about the computational effort is not performed for the scope of this study

---

**Algorithm 1** Evaluation of the minimum and maximum incremental CA control inputs, i.e.,  $\Delta U_{CA,min}$  and  $\Delta U_{CA,max}$  in Equation 3.27

---

```

1: for i=1:4 do      ▷ i corresponds to the subscript: 1=(fl), 2=(fr), 3=(wl), 4=(wr)
2:
3:    $T_{x,i,min} = \sin(\pi/2 - \delta_{i,max}) \sqrt{T_{x,i,act}^2 + T_{z,i,act}^2}$ 
4:    $T_{z,i,min} = \cos(\pi/2 - \delta_{i,min}) \sqrt{T_{x,i,act}^2 + T_{z,i,act}^2}$ 
5:
6:   if  $T_{z,i,act} > T_{i,max}$  then
7:      $T_{x,i,max} = T_{i,min}$ 
8:   else
9:      $T_{x,i,max} = \sqrt{T_{i,max}^2 - T_{z,i,act}^2}$ 
10:  end if
11:
12:  if  $T_{x,i,act} > T_{i,max}$  then
13:     $T_{z,i,max} = T_{i,min}$ 
14:  else
15:     $T_{z,i,max} = \sqrt{T_{i,max}^2 - T_{x,i,act}^2}$ 
16:  end if
17:
18:   $\Delta T_{x,i,min} = T_{x,i,min} - T_{x,i,act}$ 
19:   $\Delta T_{z,i,min} = T_{z,i,min} - T_{z,i,act}$ 
20:   $\Delta T_{x,i,max} = T_{x,i,max} - T_{x,i,act}$ 
21:   $\Delta T_{z,i,max} = T_{z,i,max} - T_{z,i,act}$ 
22:
23: end for

```

---

and can be the topic of future studies. However, it can be stated that the CA problem can be easily solved online with the today's computer technology. An extensive comparison study about the computational requirements of active-set algorithm with other approaches can be found in literature [44].

To sum up, the Control Allocation(CA) finds the incremental control input using the output of the INDI controller as an initial guess. To clarify, the INDI controller is the first step in the control loop and the CA is the second and final step to generate the overall control input considering the actuator limits and control axis prioritization. The overall block diagram of the INDI controller with integrated CA algorithm is given in Figure 3.12. Verification of the INDI controller and CA algorithm via nonlinear simulation model will be given in the next section. Several test cases are analyzed considering the wide-flight envelope of the air taxi. Robustness and disturbance rejection properties are also analyzed. In addition, the CA performance is tested for specific flight conditions (see Sections 3.3.3.3, 3.3.3.6). It is observed that the role of CA is critical in case of severe actuator saturation (i.e., limited control authority).

### **3.3.3 Nonlinear Simulation Results**

In this section, the unified controller is verified for several test cases via nonlinear simulation model build in MATLAB/Simulink. Flight dynamics model generated in Section 2 is used to represent the open-loop flight dynamics.

First, the unified controller is tested considering the full flight envelope of the air-taxi given as follows: vertical take-off, low speed hover flight, transition to forward flight, climb, cruise flight, descent, transition to hover flight and vertical landing.

Second, to show the criticality of the CA in case of limited control authority (i.e. the actuator saturation), disturbance rejection tests are done injecting severe wind-disturbance to the model. To analyze the performance of the CA design, tests are performed disabling the CA block in the loop (see Figure 3.12). When the CA is disabled, the pure INDI law given in Equation (3.23) is used in the controller. To clarify, when the CA algorithm is not active, only the simple pseudo-inverse approach

is applied for the allocation (see Equation 3.21), and the actuator saturation related problems are not resolved effectively. Simulations show that the CA plays a vital role to handle saturation related stability problems (Sections 3.3.3.3).

Third, the INDI controller's sensitivity to model parameters are analyzed. As mentioned in Section 3.3.2.2, the INDI approach significantly reduce the modeling dependency compared to the classical NDI. As a reminder, the INDI controller is only dependent on the mass, inertia and lever arm information. Therefore, the INDI controller is expected to be highly robust against the modeling errors other than the mass, inertia and lever-arms. To verify this, transition from hover to forward flight tests are performed applying significant error in the drag coefficient. It is observed that, the INDI controller's inherent robustness to modeling errors is as expected and quite promising (see Section 3.3.3.7. In addition, robustness to the model dependent parameters (i.e., the mass and inertia) are also tested in Section 3.3.3.8 to analyze the sensitivity. Based on the results, significant errors in mass and inertia can be handled by the controller. Therefore, accurate modeling of the mass and inertia is not required to have desired controller response.

To illustrate the results, three plots are used for each test scenario. First plot gives the aircraft state response and commands. Second plot shows the required accelerations ( $\dot{x}_{req}$ ) and acceleration estimations obtained from the sensors ( $\dot{x}_0$ ) used in the INDI control law (Equation 3.20). Third plot illustrates the actuator states including both the direct output of the controller and actuator states considering the actuator dynamics with subscript "act" (see Equation 3.14). Note that simulations are performed applying different types of commands given in Equation 3.26. Details of the command generation function is described in Section 3.3.2.5.

To observe the CA algorithm's computational properties, the "CA Iteration Number" is also given in the plots. If the "CA Iteration Number" is above 1, then the CA algorithm overwrites the INDI controller's output (see Figure 3.12) to find the optimum allocation iteratively considering the actuator limits and channel prioritization described in Section 3.3.2.7.

### 3.3.3.1 Vertical Take-off, Hover & Low Speed Flight

First, the unified controller is tested for hover & low speed flight condition. The test case is explained as following. Some commands are applied simultaneously to observe the controller’s response during the coupled dynamics.

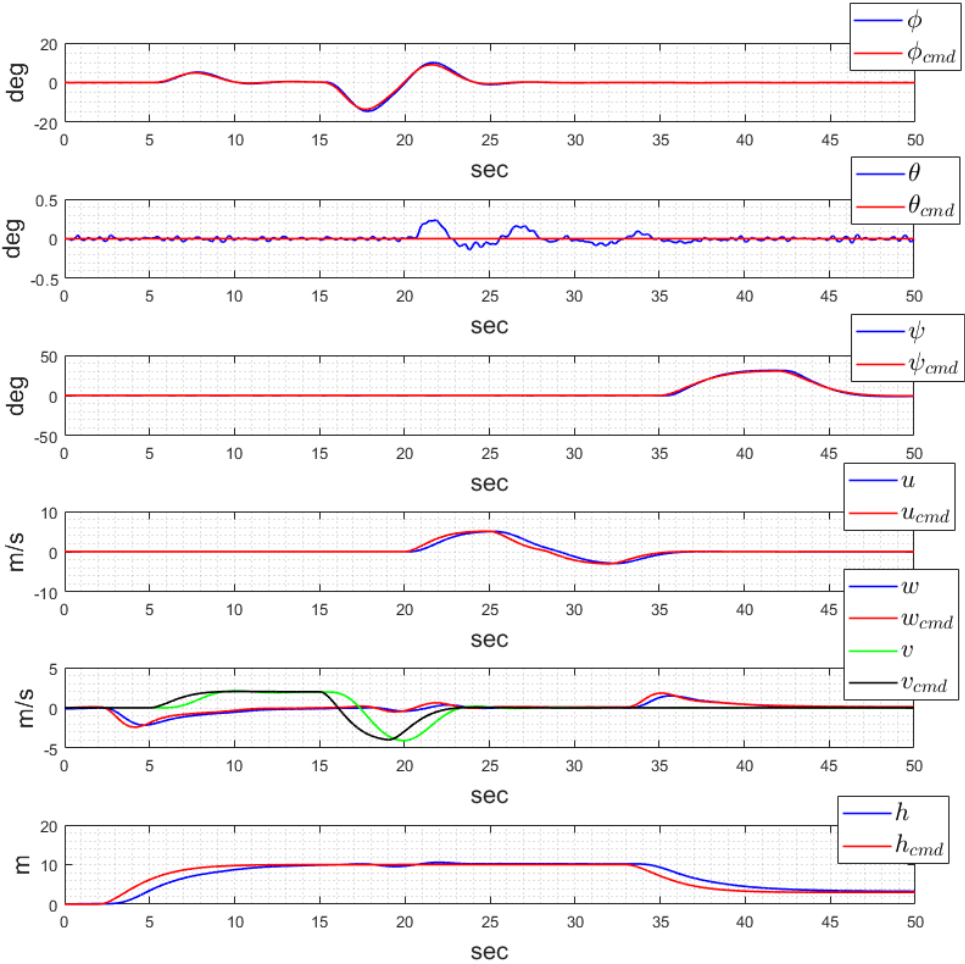


Figure 3.13: Hover & low speed flight test results, state response.

1. At 3 seconds, 10 m. altitude command ( $h_{cmd}$ ) is applied, and the controller tracks the corresponding vertical velocity command ( $w_{cmd}$ ). Similarly, at 35 seconds vertical landing command is applied.
2. Between 7 and 25 seconds, positive and negative side velocity is commanded

( $v_{cmd}$ ) to achieve side-ward translational motion via generating corresponding roll angle command ( $\phi_{cmd}$ )

3. Between 20 and 35 seconds, forward and backward motion is tested via applying velocity command in the body x-direction ( $u_{cmd}$ )

4. Between 35 and 45 seconds, aircraft heading is changed by commanding yaw angle ( $\psi_{cmd}$ )

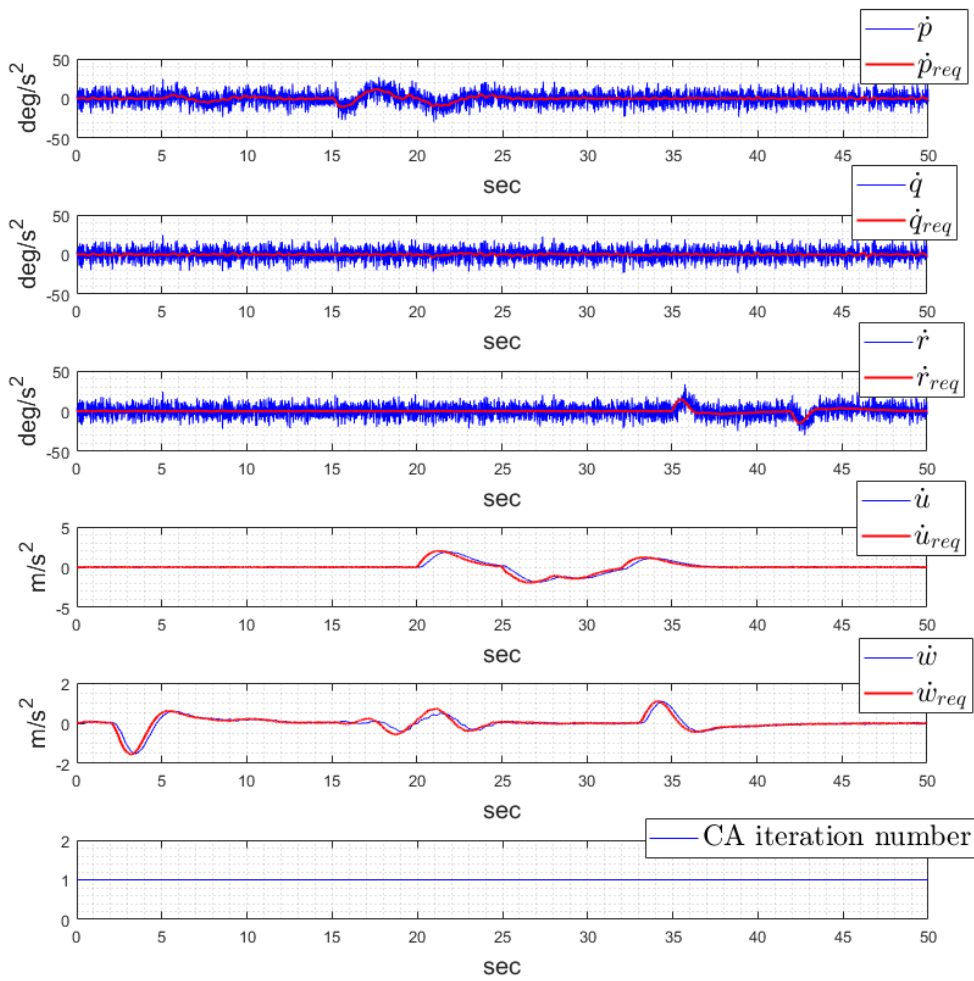


Figure 3.14: Hover & low speed flight test results, required and obtained state derivatives.

**1. Analyses of the Altitude Response:**



According to Figure 3.13, 10 m. altitude is commanded at 3 seconds, and the aircraft tracks the corresponding vertical speed command ( $w_{cmd}$ ). In between 10 and 35 seconds, several commands are applied in other channels. The aircraft keeps the 10 m. altitude during the forward, side-ward motions and also the heading change. Note that the command generator applies approximately  $2m/s^2 \approx 0.2g$  maximum vertical acceleration command (Figure 3.14,  $\dot{w}_{req}$ ). According to Figure 3.14,  $w_{cmd}$  is tracked well and the aircraft holds altitude ( $h$ ) while other commands cause disruptive effects on the vertical channel.

Regarding the control inputs, it is expected to increase only thrust and not changing tilt angles to gain altitude. Results given in Figure 3.15 is consistent with the expectation. Thrust levels increase around  $100N$  on the canard EDFs and  $200N$  on the wing EDFs to gain altitude. 1/2 ratio in thrust increment between the canard and wing EDFs is to achieve zero pitch disturbance while gaining altitude since x-lever arms( $\Delta x$ ) of the front and wing EDFs has an approximate ratio of 1/2 as given in Equation (3.13).

## 2. Analyses of the Side Motion:

To perform side-ward motion at low speeds, positive and negative side velocity commanded between 7 and 25 seconds. As mentioned, EDFs do not generate side force directly. Therefore, thrust direction is changed via applying a navigational bank angle command ( $\phi_{cmd,nav,hover}$ ) at low speeds based on Equation (3.26).

As shown in Figure 3.13,  $v_{cmd}$  and the corresponding  $\phi_{cmd,nav,hover}$  are tracked well. There exist a small delay in tracking of the side velocity command. This result is expected since side velocity is not directly controlled and result of change in thrust vector direction. Linear navigational controller gains  $K_v, K_{\dot{v}}$  can be increased to reduce the delay in side velocity command tracking if necessary (Table 3.3).

Roll rate tracking performance of the controller is given Figure 3.14. Required roll rate  $\dot{p}_{req}$  is tracked accurately despite the significant sensor noise.

To change the roll angle at low speeds, thrust levels are changed oppositely on the right and left sections of the aircraft and no change in the tilt angles are expected. The required change in thrust is very small to achieve the desired roll rates. On the other

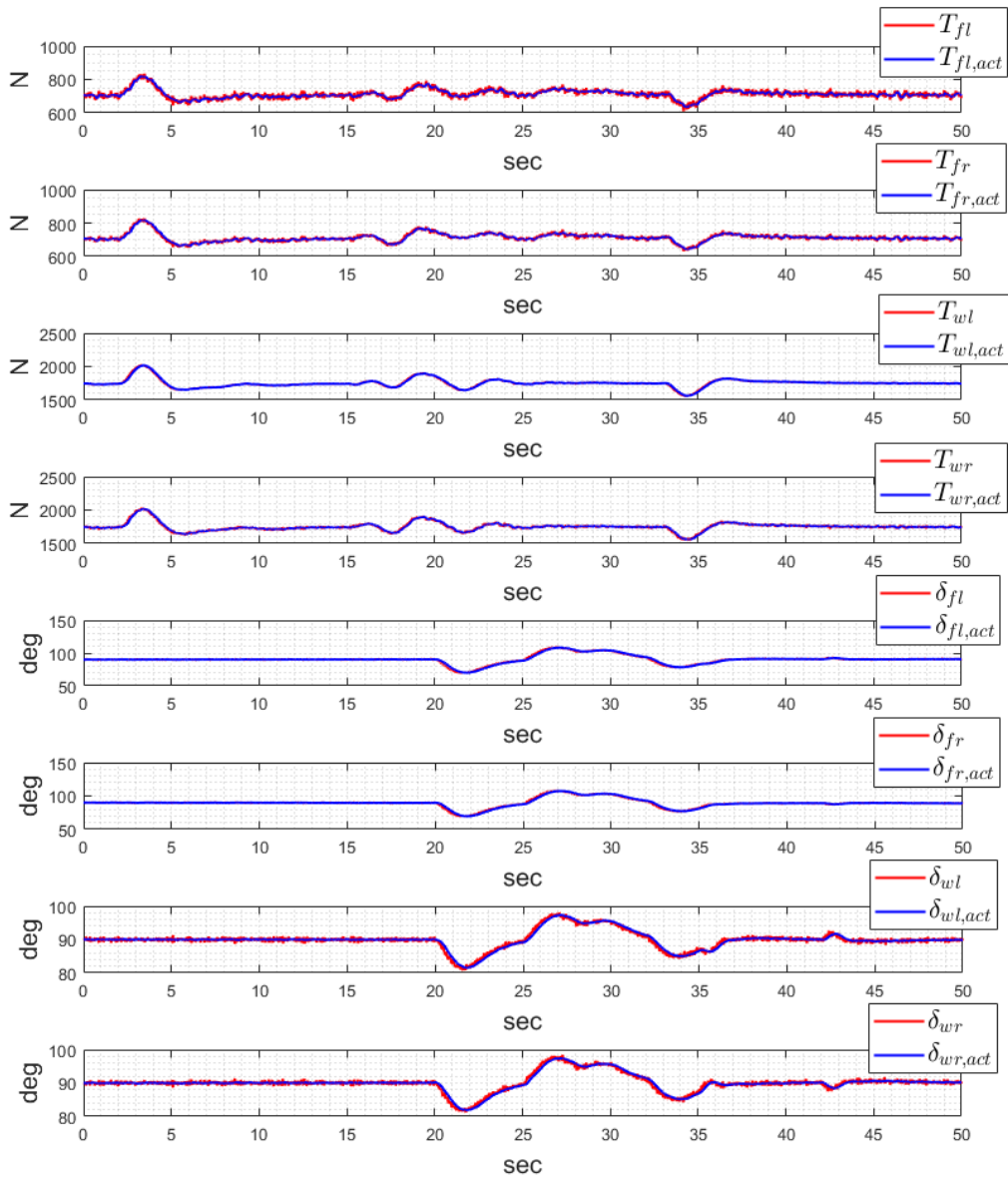


Figure 3.15: Hover & low speed flight test results, actuator states.

hand, to keep the altitude during the side-motion thrust must be increased significantly since thrust vector is not aligned with the gravity. Therefore, the asymmetric change in thrust between the right and left sections can not be observed directly in Figure 3.15 since it illustrates the total thrust command. Tilt angles are kept same during the side-motion as expected.

### 3. Analyses of the Forward and Backward Motion:

Translational motion in the body x direction is obtained via commanding body x-velocity ( $u_{cmd}$ ). The same command is also used to perform the transition easily and also to control the angle of attack indirectly in forward flight.

Based on Figure 3.13,  $\pm 5m/s$  forward velocity command is applied between 20 and 35 seconds, and the required state derivative ( $\dot{u}_{req}$ ) is tracked well (Figure 3.14). To accelerate in forward direction, it is expected to tilt EDFs in negative direction to use some of the thrust for forward acceleration. Similarly, to decelerate, tilt angles need to increase. Note that at hover tilt angles are 90 degrees. These two outcome can be seen on the actuator states given in Figure 3.15 between 20 and 35 seconds.

### 4. Analyses of the Heading Response:

To change the aircraft heading,  $\pm 30deg$  yaw angle is commanded between 35 and 45 seconds (Figure 3.13). The INDI controller tracks the required body yaw rate ( $\dot{r}_{req}$ ) to achieve the desired heading. According to Figure 3.14, yaw rate tracking performance is satisfactory.

To change the aircraft heading at hover, tilt angles of the right and left EDFs change asymmetrically. This result can be seen at 43 seconds of actuator states plot (Figure 3.15) when the negative heading command is applied. It is observed that approximately 4-5 degree changes on the wing EDFs are enough to achieve the desired heading command, and tilt angle changes on the front EDFs are much more smaller. Since change in tilt angles are very small, additional thrust required to keep the altitude is very small.

#### 3.3.3.2 Transition From Hover to Cruise Flight

*Transition from hover to forward flight is one of the most critical flight regime regarding the flight control due the coupled thrust vector control and severe nonlinearities during the transition (see Section 3.1). Note that nonlinearities occur in the aerodynamic model during the transition due to the blending between the hover and forward flight models explained in Section 2.1.3.*

EDFs on both front and wing sections are tilted forward to accelerate the aircraft. Rpm/thrust is also adjusted to keep both pitch attitude and altitude at desired level while accelerating the aircraft to high speed forward flight.

It is reminded that, to design the LQR controller in Section 3.2, aircraft is trimmed at cruise condition with 78 m/s airspeed and 4 degree angle of attack. Detailed trim data including the trim actuator states for cruise condition is given in Equation (3.6). Actuator states are given in terms of rpm and tilt angle in Equation (3.6) and to be consistent with the INDI structure trim actuator states are represented as thrust and tilt angle using the relation between rpm and thrust given in Equation (2.12). Then, the cruise trim data is expressed in terms of the INDI actuator states as following.

$$\begin{aligned}
 U &= \left[ T_{fl} \ T_{fr} \ T_{wl} \ T_{wr} \ \delta_{fl} \ \delta_{fr} \ \delta_{wl} \ \delta_{wr} \right]^T \\
 &= [356 \ 356 \ 213 \ 213 \ 0.52 \ 0.52 \ 0.08 \ 0.08]^T \\
 x_{trim} &= [\phi \ \theta \ \psi \ u \ v \ w \ p \ q \ r]^T = [0 \ 0.07 \ 0 \ 78 \ 0 \ 5.5 \ 0 \ 0 \ 0]^T \quad (3.28) \\
 V_{\infty trim} &\approx 78 \text{ m/s}, \quad \alpha_{trim} \approx 0.07 = 4 \text{ deg}, \quad \beta_{trim} = 0
 \end{aligned}$$

According to the trim data at 78 m/s, the front EDFs generate total of 356 N at both left and right sections and tilt angle is around 29 degrees (0.52 rad); whereas, the wing EDFs generate total of 213 N at both left and right sections with tilt angle of approximately 4.5 degrees (0.08 rad).

Based on the trim data, the aim is to accelerate the aircraft to 78 m/s airspeed and also achieving 4 degree angle of attack once 78 m/s airspeed is reached.

To sum up, the following commands are applied to perform the transition maneuver and achieving the predefined cruise flight conditions.

1. Altitude command is applied at 2 seconds to climb 40 meters.
2. 45 degree heading is commanded at 5 seconds to change the aircraft heading while climbing.

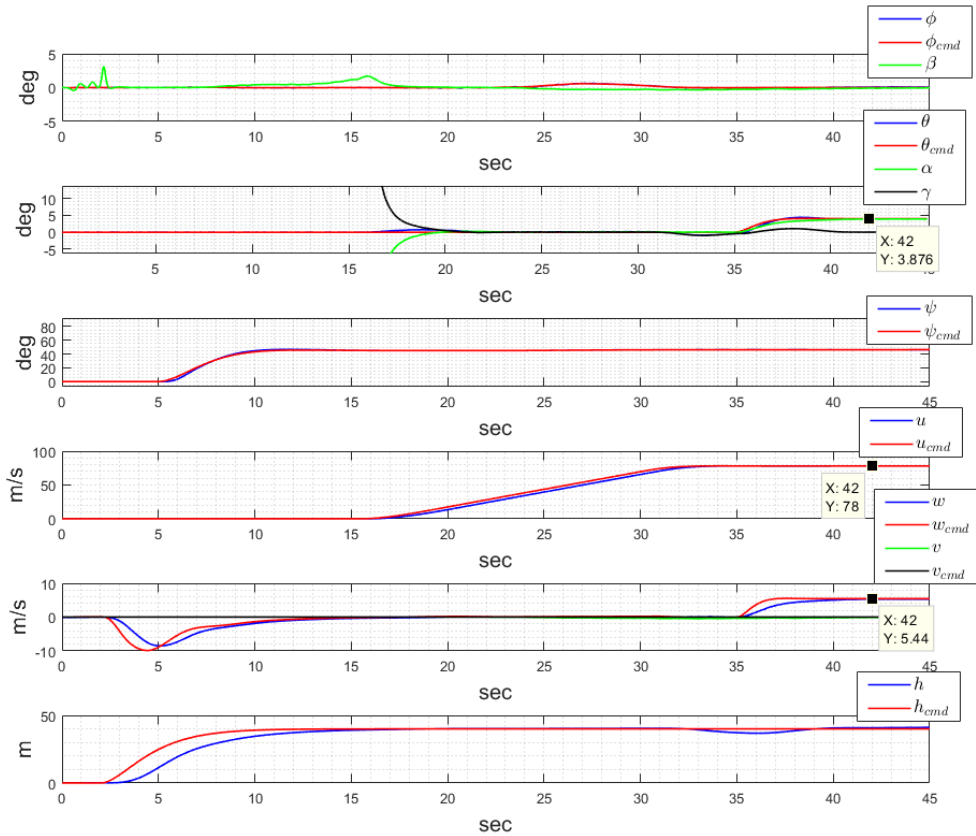


Figure 3.16: Hover to cruise transition test results, states.

3. Between 15 and 35 seconds the body x velocity ( $u$ ) is commanded to achieve 78 m/s cruise airspeed.

4. At 35 seconds, 4 degree  $\theta_{cmd}$  and corresponding 5.5 m/s  $w_{cmd}$  are applied simultaneously to achieve 4 degree trim angle of attack with zero flight path angle.

Figure 3.16 shows the state response of the transition tests. The aircraft climb to 40 meters at first and orients its heading to 45 degrees before accelerating. 78 m/s is reached at 35 seconds with an approximate acceleration of 5 m/s which can be seen on Figure 3.17,  $\dot{u}$  plot.

According to the actuator states plot given in Figure 3.18, both front and wing section EDFs' tilt angle decrease after 15 seconds to provide thrust for the forward acceleration. During the forward acceleration, thrust levels are increased on both front and

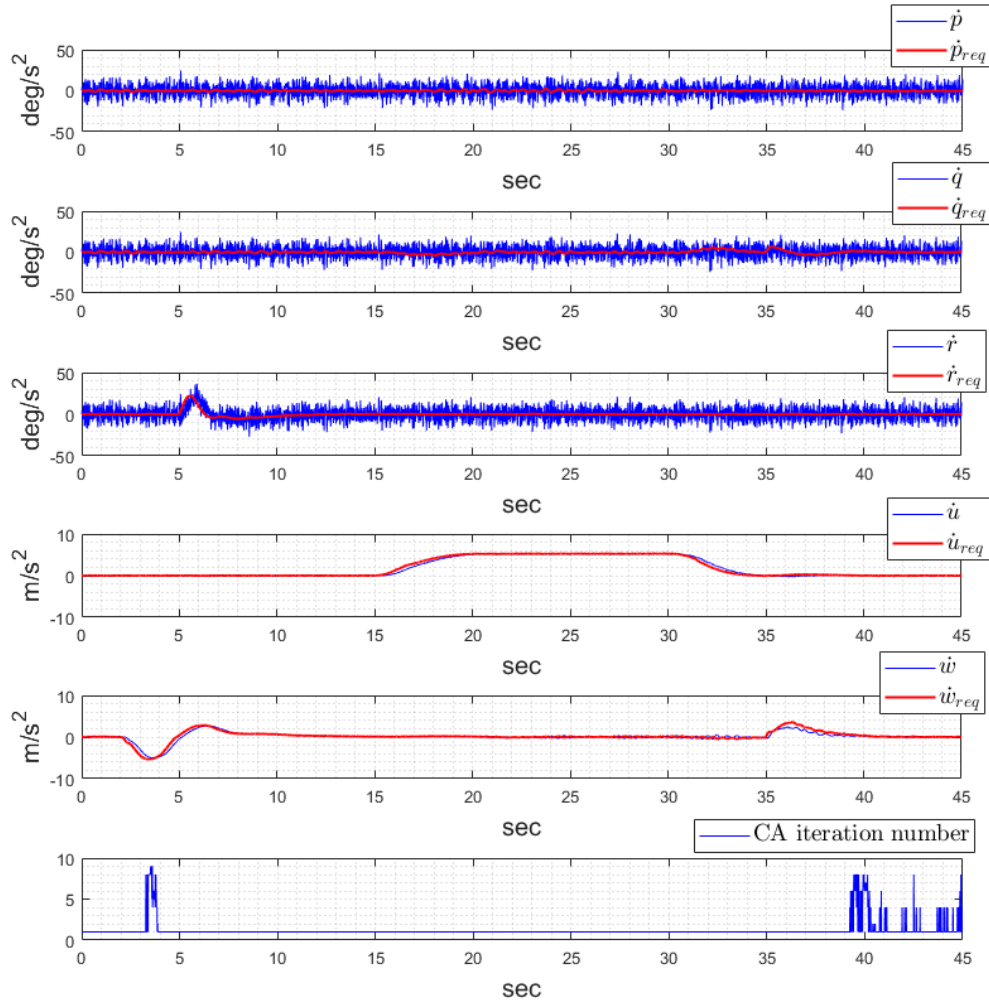


Figure 3.17: Hover to cruise transition test results, required and obtained state derivatives.

wing EDFs to keep desired altitude. Thrust increase at the front EDFs are higher compared to the wing EDFs. This is an expected result since with the increasing airspeed lift generated by the wings increase and generate positive pitch moment. To balance the lift generated pitch moment, the front EDFs generate more thrust.

At 30 seconds, forward acceleration command is pulled back and EDFs increase tilt angle as expected to lower the forward acceleration (between 30 and 35 seconds of Figure 3.18).

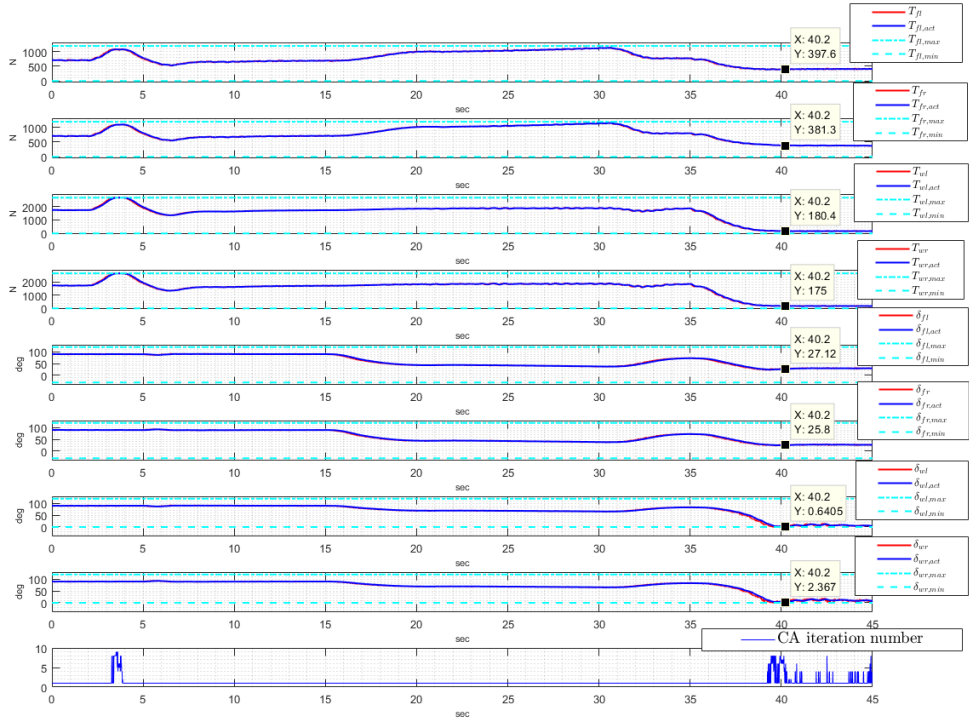


Figure 3.18: Hover to cruise transition test results, actuator states.

The INDI controller is designed to control the body angular rates and velocities, see Equations (3.17) and (3.25). Therefore, it is possible to control the angle of attack and flight path angle indirectly using the relations given in Equation (2.26). To achieve 4 degree trim angle of attack, combined 4 degree  $\theta_{cmd}$  and 5.5 m/s  $w_{cmd}$  are applied at 35 seconds. (Figure 3.16). Desired trim values are reached with small loss in the altitude (2-3 m.). Based on Figure 3.16), trim states are achieved with very small errors such as;  $\alpha_{trim} = 3.87 \text{ deg}$ ,  $w_{trim} = 5.44 \text{ m/s}$ ,  $u_{trim} = 78 \text{ m/s}$ ,  $\beta_{trim} \approx 0 \text{ deg}$ ,  $\gamma_{trim} \approx 0 \text{ deg}$ , compared to the trim data given in Equation (3.28).

It is also important to analyze the actuator states at the cruise trim condition, and to check consistency with the linearized model cruise trim data given in Equation (3.28). Based on Figure 3.18, thrust values at trim are 381 and 397 N for the front EDFs, and 180 and 175 N for the wing EDFs. Moreover, tilt angles at trim are 27.1 and 25.8 degrees for the front EDFs, and 0.6 and 2.3 degrees for the wing EDFs. Although there exist small differences in the trim actuator states compared to the linearized

model trim data given in Equation (3.28), the trend is the same. It is expected to have minor discrepancy in the trim actuator states since the nonlinear simulation model includes additional effects (e.g., couplings, sensor noise, delays, etc.) that are not represented in the linearized trim data.

Performance of the CA algorithm is also analyzed. The last plot of Figure 3.18 shows the CA iteration number, more explicitly whether the CA algorithm is actively working or not. At 3 seconds, an aggressive  $-5 \text{ m/s}^2$  (approx. 0.5g) vertical acceleration command ( $\dot{w}_{req}$ , Figure 3.17) is applied. The INDI controller's output violates the maximum rpm/thrust limit for the wing EDFs while tracking the vertical acceleration command. At this point, the CA algorithm becomes active and allocates the limited control authority prioritizing the rotational channels (mainly the pitch moment channel for this case) over the translational channels (vertical motion). In other words, the CA overwrites the INDI controller's output considering the actuator limits and prioritization order (see Figure 3.12). Then, the vertical acceleration command is not tracked accurately since the remaining control authority is used to guarantee stable flight. The CA algorithm allocates the limited control authority properly and generates the actuator states considering the maximum thrust limits (3rd and 4th plots of Figure 3.18 between 3-5 seconds, output of the CA and physically limited actuator states overlaps). Similarly, after 38 seconds the INDI controller's outputs are lower than the minimum tilt angle limits for the wing EDFs (7th and 8th plots of Figure 3.18). The CA algorithm again becomes active and allocate the limited control authority as expected. To analyze the criticality of the CA, the same transition test is performed without activating the CA block and using the direct outputs of the INDI controller (see next Section 3.3.3.3). Results show that, without proper CA design, the aircraft can not achieve desired cruise condition since the INDI controller's outputs are out of actuator limits. *To conclude, the CA design described in Section 3.3.3.2 works properly and has a vital role in case of limited control authority.*

The CA performance is also investigated considering the real time implementation. According to the last plot of Figure 3.18, the maximum "CA Iteration Number" are below 10 when the CA is active. Therefore, the CA algorithm finds the optimal solution very fast. Moreover, the CA algorithm does not cause discontinuities/sudden jumps in the actuator states which is crucial for the real time implementation.



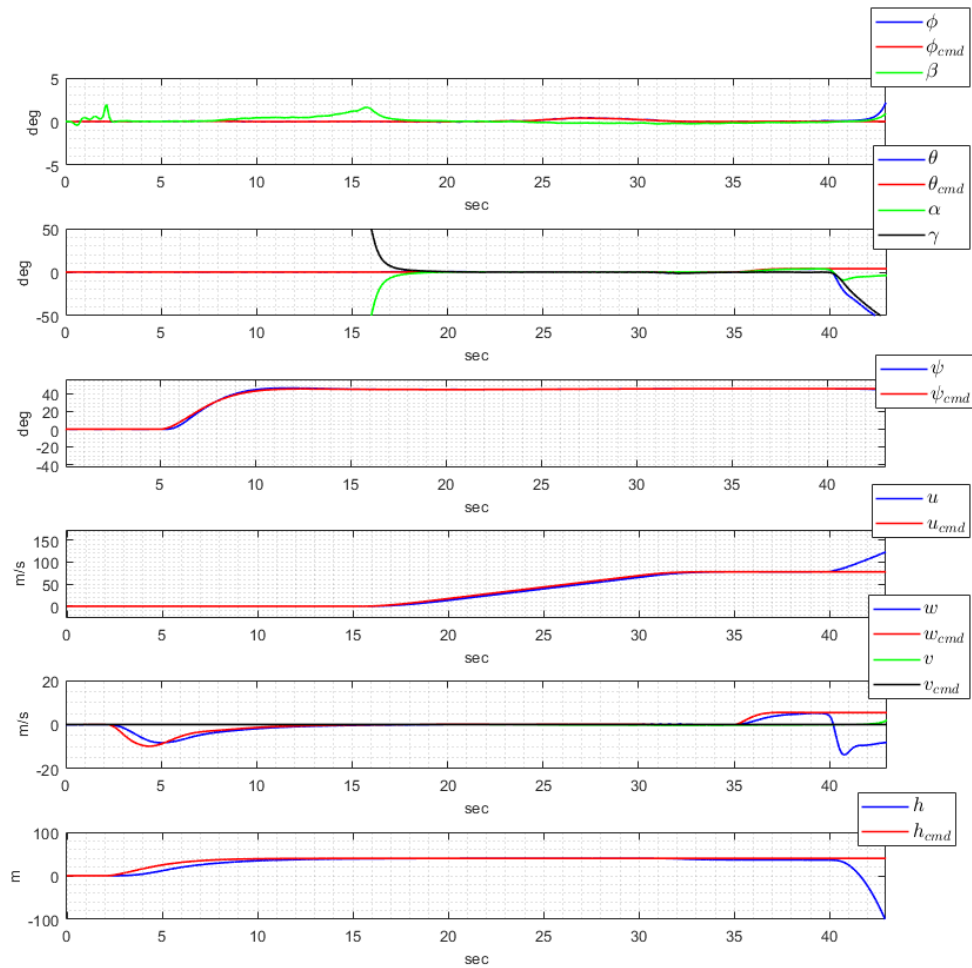


Figure 3.19: Hover to cruise transition test results without the Control Allocation, states.

### 3.3.3.3 Importance of the CA: Hover to Cruise Transition without the CA

The hover to cruise transition test case is performed with disabling the CA algorithm and using the direct output of the INDI controller given in Equation (3.23) (see Figure 3.12). More explicitly, actuator saturation is not considered in the control allocation and only the pseudo-inverse approach used in the INDI formulation is considered for the allocation (see Equation 3.21).

Results are given in Figures 3.19, 3.20 and 3.21. Based on the results, actuator saturation are not observed up to 40 seconds, and the INDI controller's performance is

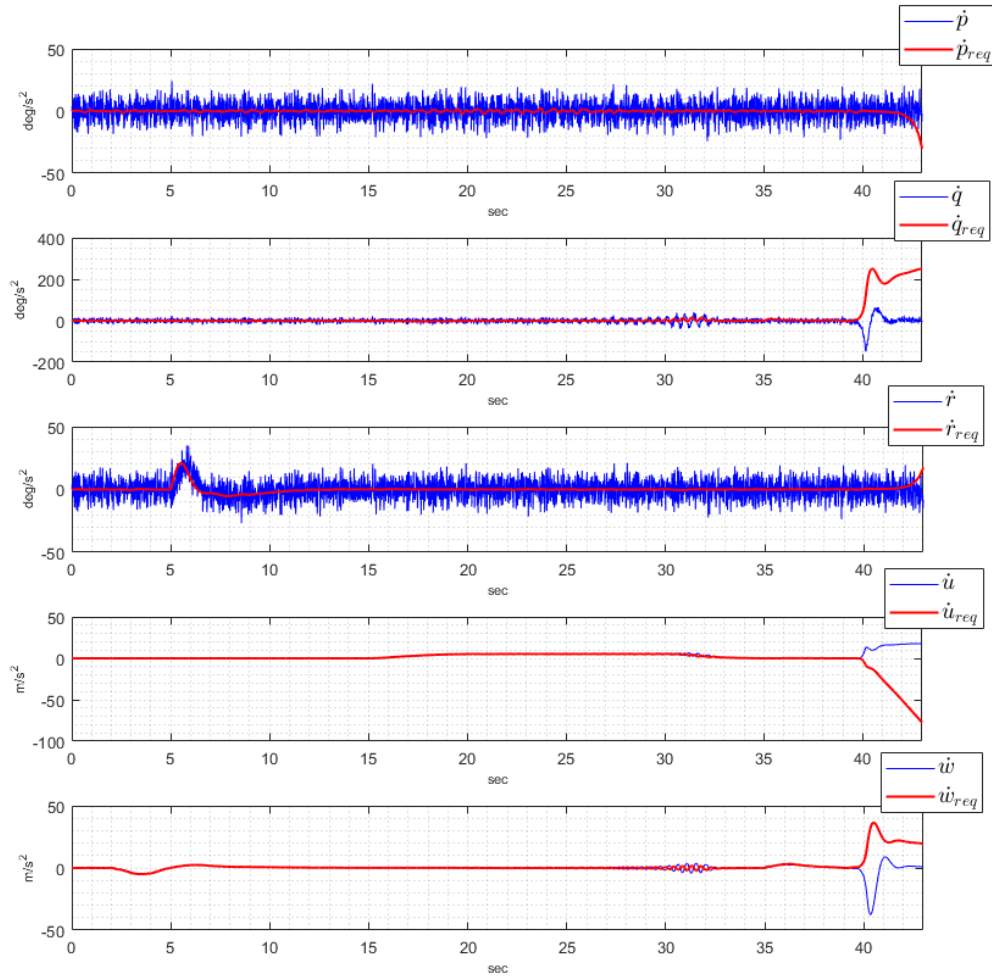


Figure 3.20: Hover to cruise transition test results without the Control Allocation, required and obtained state derivatives.

satisfactory. However, the INDI controller’s outputs are out of actuator limits after 40 seconds (Figure 3.21). Then, actuator commands generated by the INDI can not be achieved in reality due to the position limits, and control is lost since the INDI controller becomes ineffective. As described in Section 3.3.3.2, the same transition test case is performed successfully when the CA algorithm is active.

*To conclude, the CA has a vital role regarding the proper allocation of the limited control authority. Criticality of the CA will be also discussed thoroughly in disturbance rejection test case (Section 3.3.3.6).*

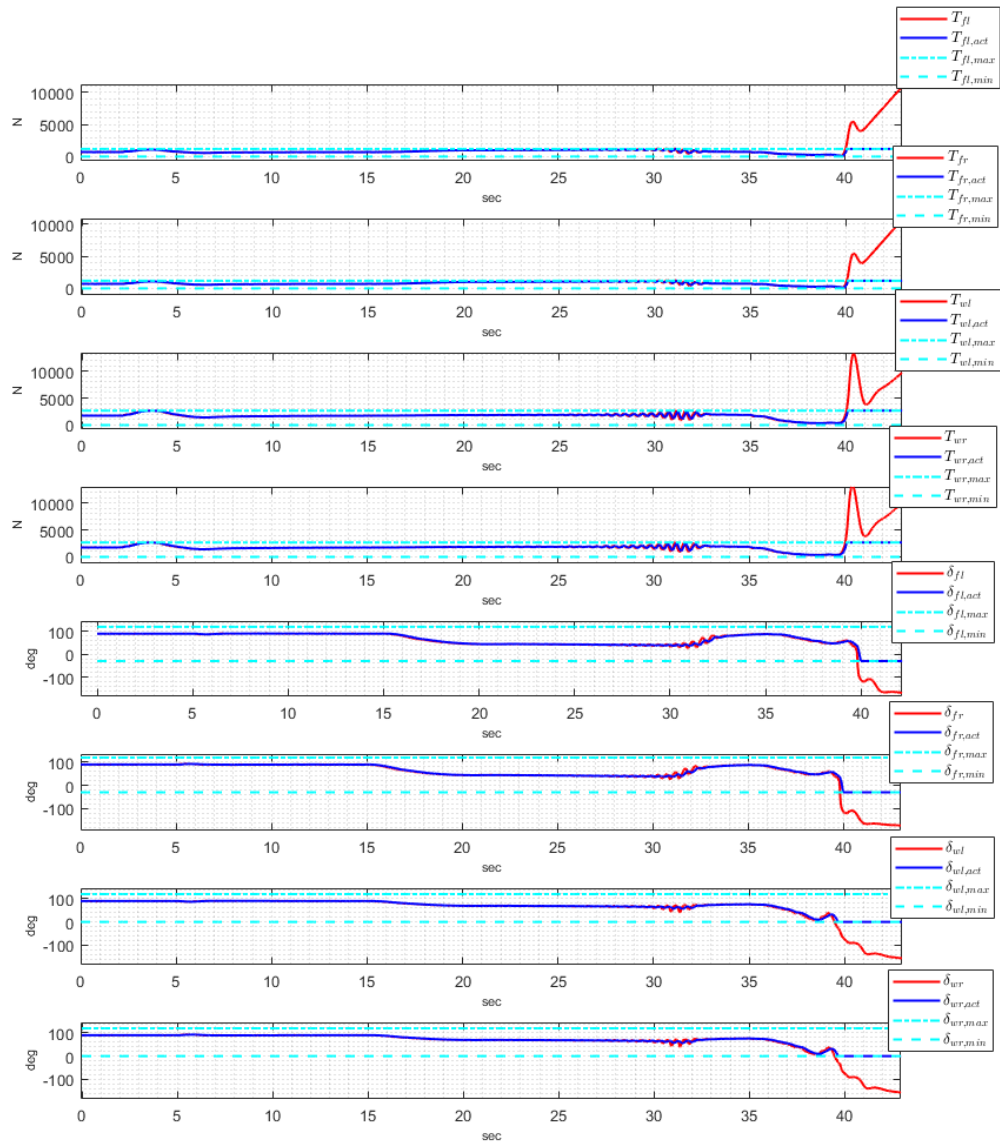


Figure 3.21: Hover to cruise transition test results without the Control Allocation, actuator states.

### 3.3.3.4 Climb/Descent & Coordinated Turn at Cruise

Climb, descent and turn maneuvers are tested at cruise condition. Results are given in Figures 3.22, 3.23, and 3.24.

First,  $\pm 5$  degree flight path angle commands are applied between 45 and 70 seconds

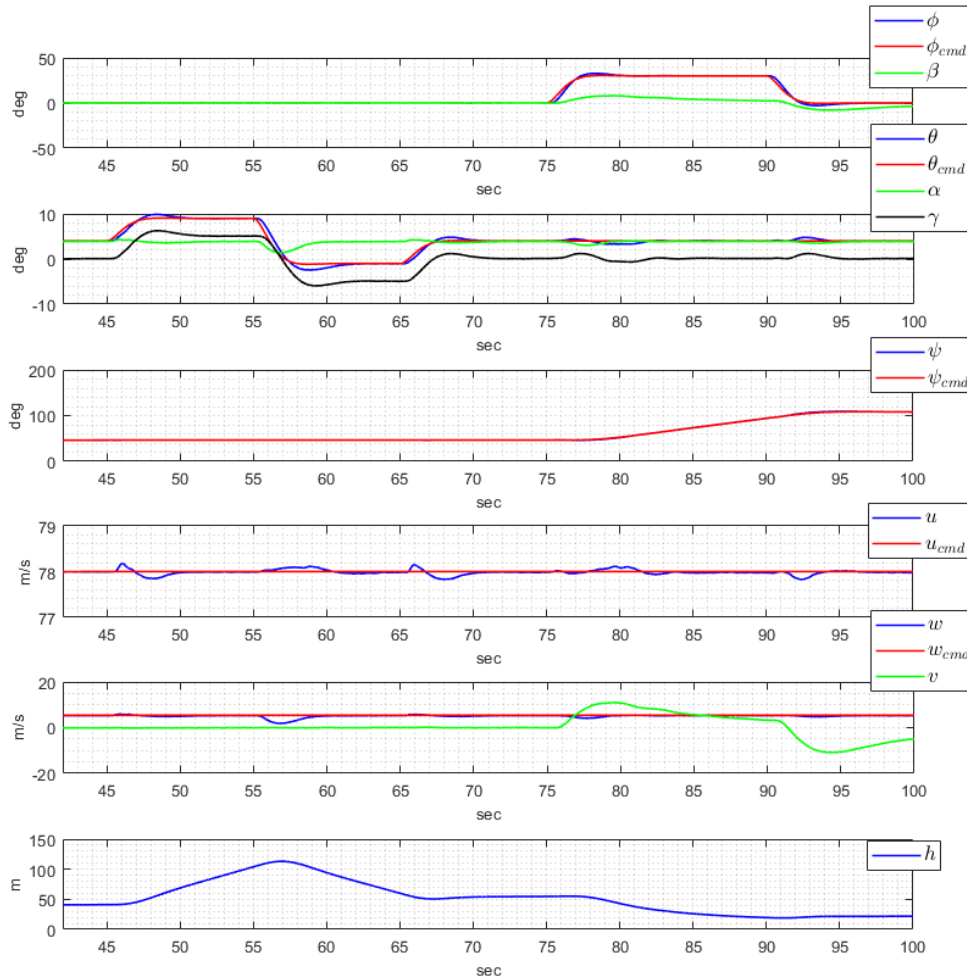


Figure 3.22: Climb/Descent & Coordinated turn at cruise, states.

(Figure 3.22). Then, coordinated turn is performed applying 30 degree roll angle command and the corresponding yaw rate command given in Equation 3.12. Controller's performance is satisfactory during the climb, descent and turn maneuvers. Note that the aircraft loses altitude during the turns (altitude response after 80 seconds in Figure 3.22). An outer loop controller can be designed to improve the altitude loss behavior during the turns.

According to the actuator states plot given in Figure 3.24, the CA algorithm becomes active several times during the climb, descent and turn maneuvers. Lower tilt angle and thrust limits are reached numerous times during the maneuvers. The CA priori-

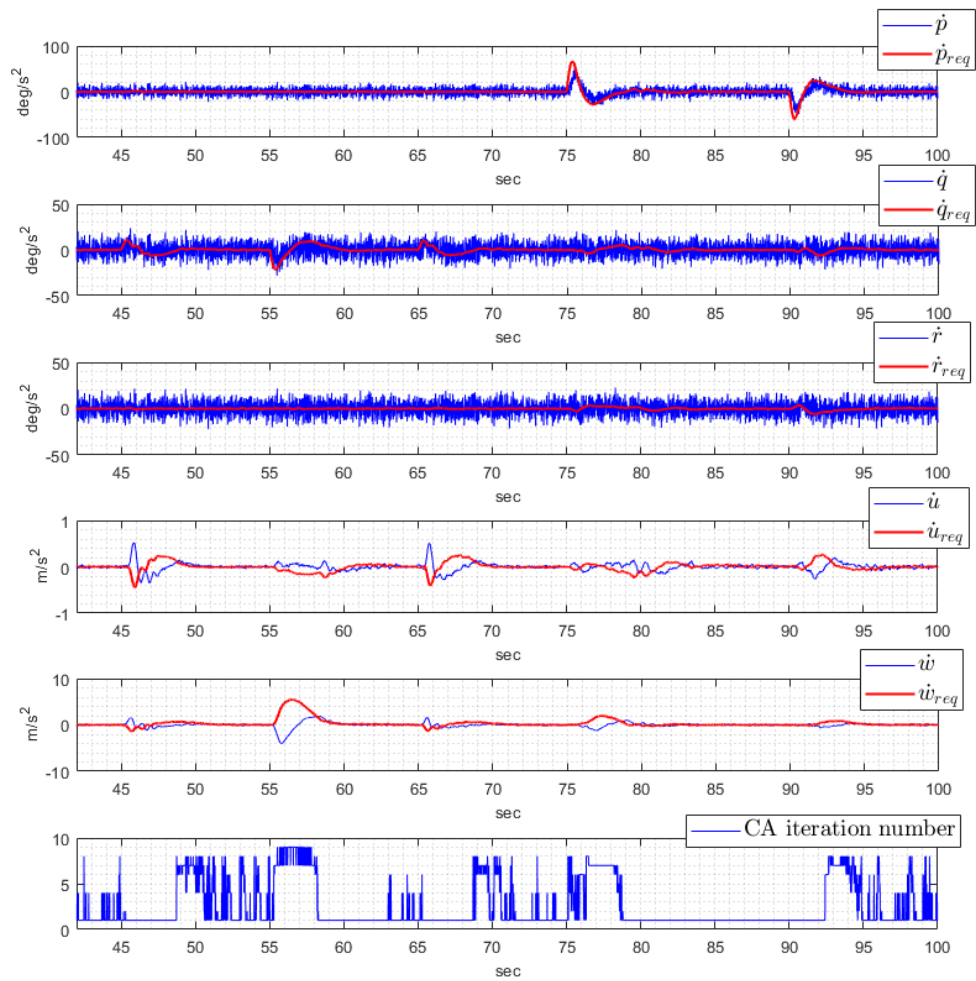


Figure 3.23: Climb/Descent & Coordinated turn at cruise, required and obtained state derivatives.

tizes rotational channels over the translational channels to satisfy stable flight in case of actuator saturation. This prioritization order can be seen in Figure 3.23. Translational commands ( $\dot{u}_{req}$  and  $\dot{w}_{req}$ ) are not tracked well when the CA prioritizes the rotational channels to make sure that the rotational commands are tracked accurately. Note that the maximum iteration number of the CA algorithm is less than 10, and the actuator commands are continuous (Figure 3.24).

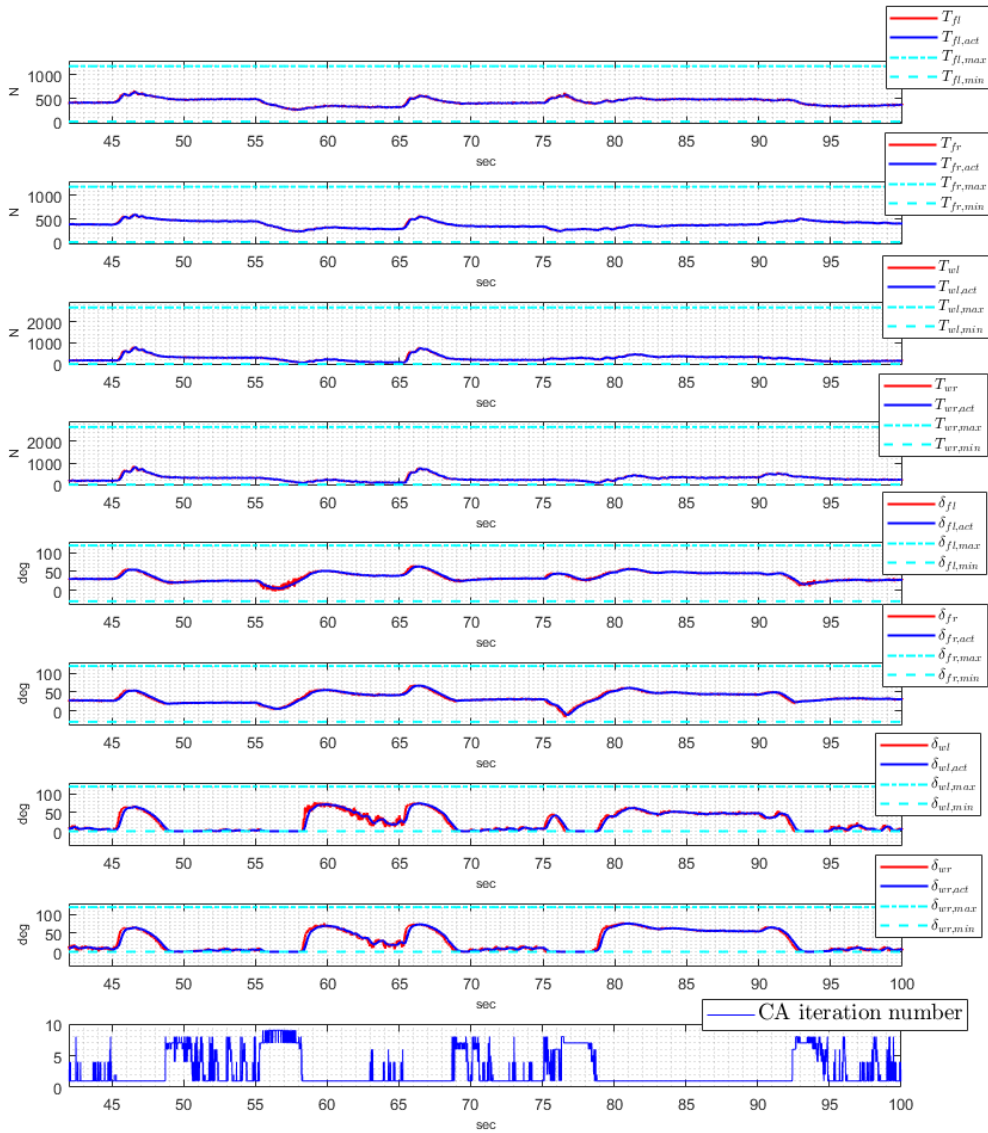


Figure 3.24: Climb/Descent & Coordinated turn at cruise, actuator states.

### 3.3.3.5 Transition from Cruise Flight to Hover & Vertical Landing

*Transition from high speed cruise flight to hover flight is also a critical flight phase due to highly coupled thrust vector control during transition and nonlinearities emerging in the flight dynamics model (i.e., the blending between forward and hover flight aerodynamic models). Results of the transition tests are given in Figures 3.25, 3.26,*

and 3.27.

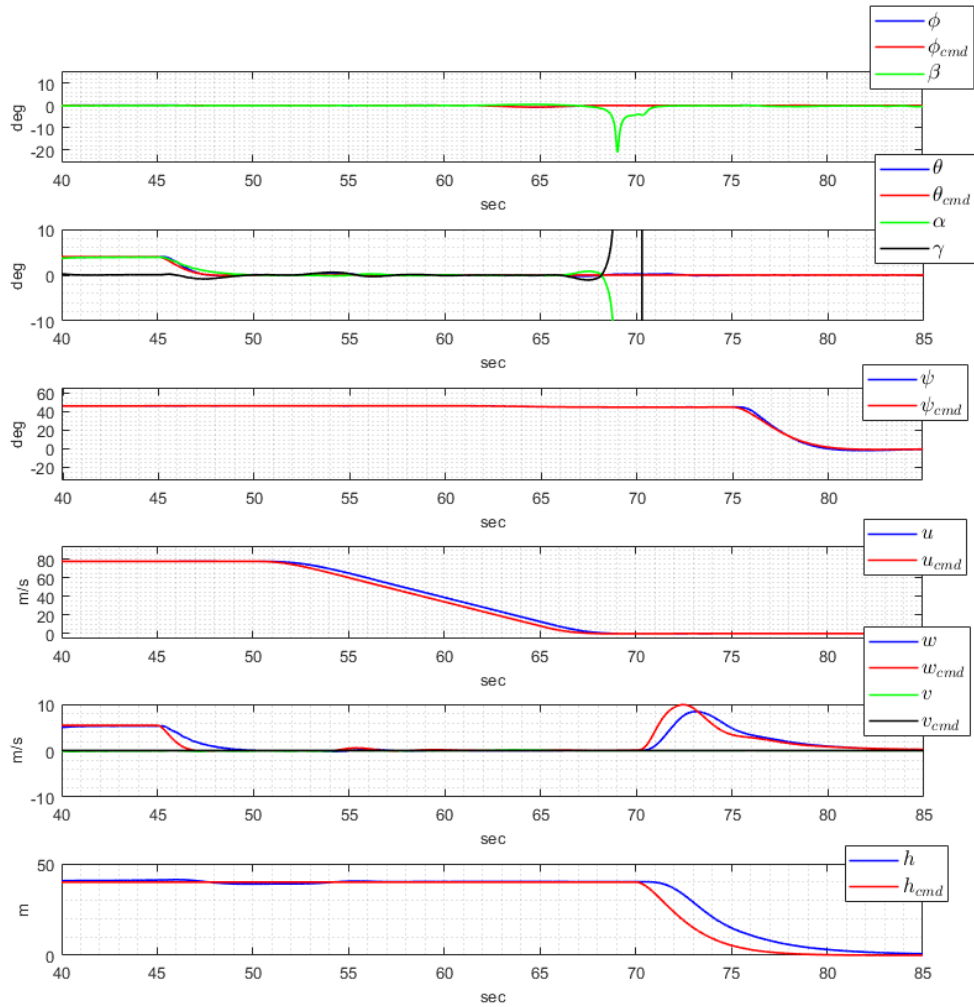


Figure 3.25: Transition from Cruise Flight to Hover & Vertical Landing, states.

Cruise to hover transition tests are starting at the cruise condition with 4 degree angle of attack and 78 m/s airspeed. First, zero angle of attack is achieved via commanding the corresponding pitch angle ( $\theta_{cmd}$ ) and body vertical velocity ( $w_{cmd}$ ) at 45 seconds. Then,  $5\text{ m/s}^2$  deceleration command is applied at 50 m/s (Figure 3.26). As expected, tilt angles and rpm/thrust increase during the transition since lift generated by the wing reduces with the decreasing airspeed. At 70 seconds, aircraft reach the hover condition with 90 degree tilt angles and hover trim thrust values (Figure 3.27). After 70 seconds, zero altitude command is applied and the aircraft lands vertically at 85

seconds. During the vertical landing, aircraft heading is also changed.

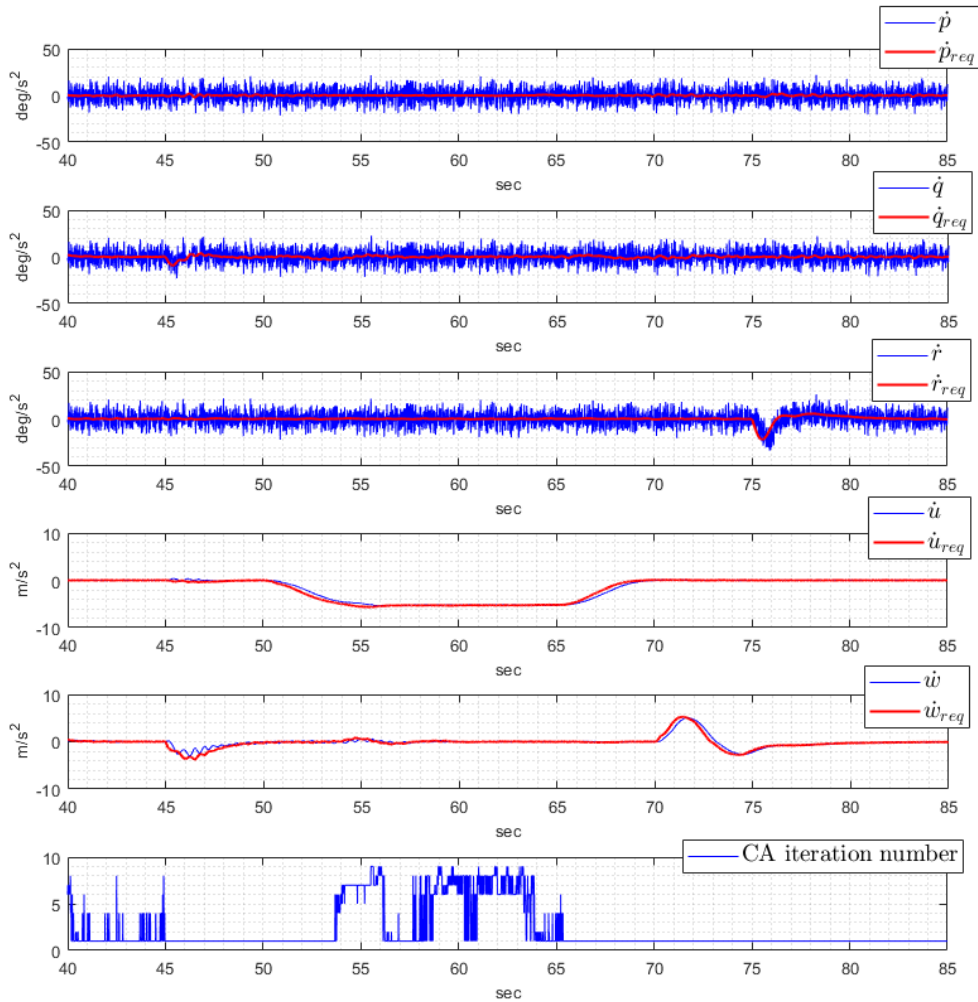


Figure 3.26: Transition from Cruise Flight to Hover & Vertical Landing, required and obtained state derivatives.

*In general, controller's performance is satisfactory during the transition and vertical landing. Note that the CA algorithm also works properly during the transition maneuver (Figure 3.27).*



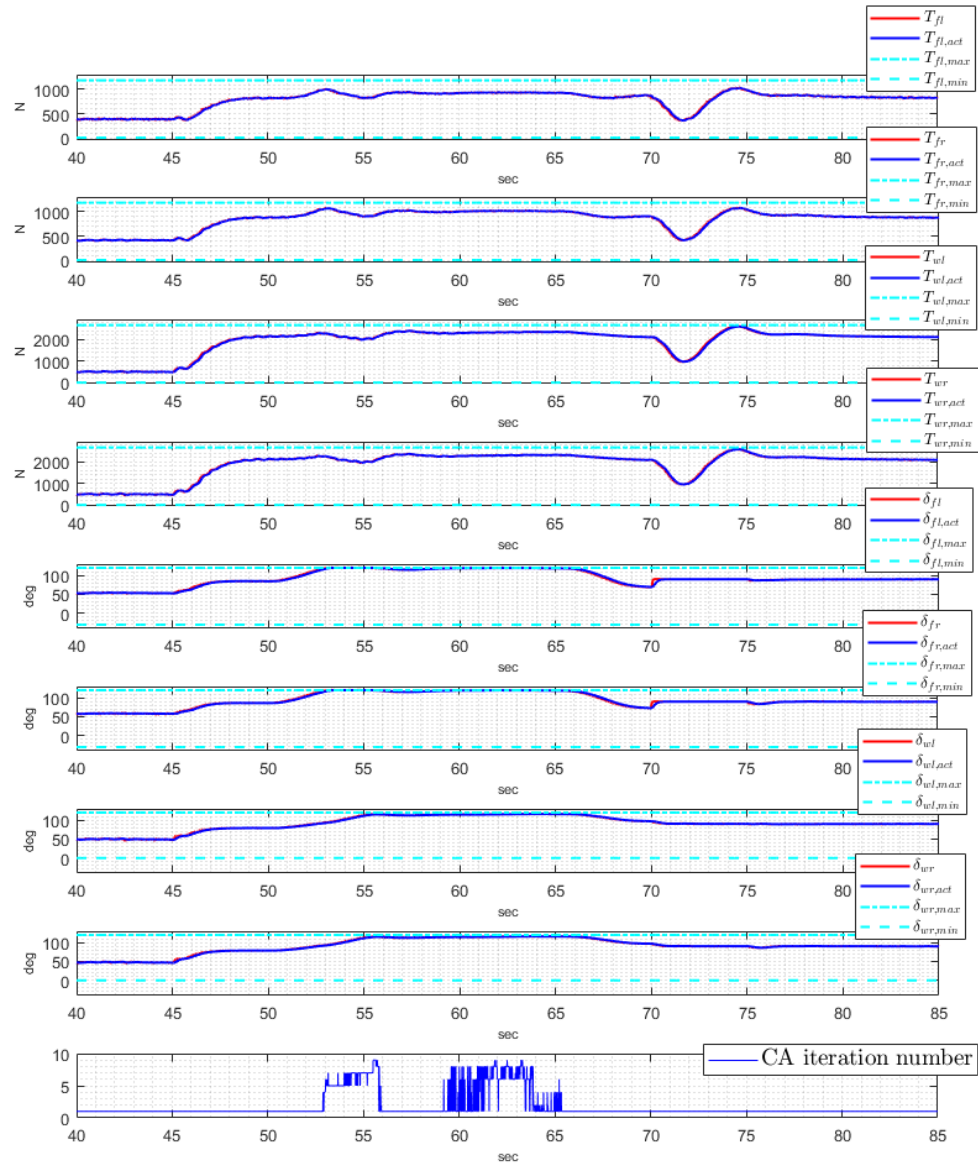


Figure 3.27: Transition from Cruise Flight to Hover & Vertical Landing, actuator states.

### 3.3.3.6 Importance of the CA: Disturbance Rejection with and without the CA

To analyze the disturbance rejection characteristics of the controller, severe roll moment disturbance is injected to the simulation model at hover condition. To observe the disturbance rejection characteristics at limited control authority, a climb command

(i.e, a negative vertical velocity command,  $w_{cmd}$ ) is also applied during the roll moment disturbance (Figure 3.28). The aim is to observe the effectiveness of the CA algorithm at limited control authority. Therefore, the same test case is runned when the CA algorithm is enabled ("CA ON, INDI+CA") and disabled ("CA OFF, only INDI"). Figures 3.28, 3.29, and 3.30 show the results for two cases.

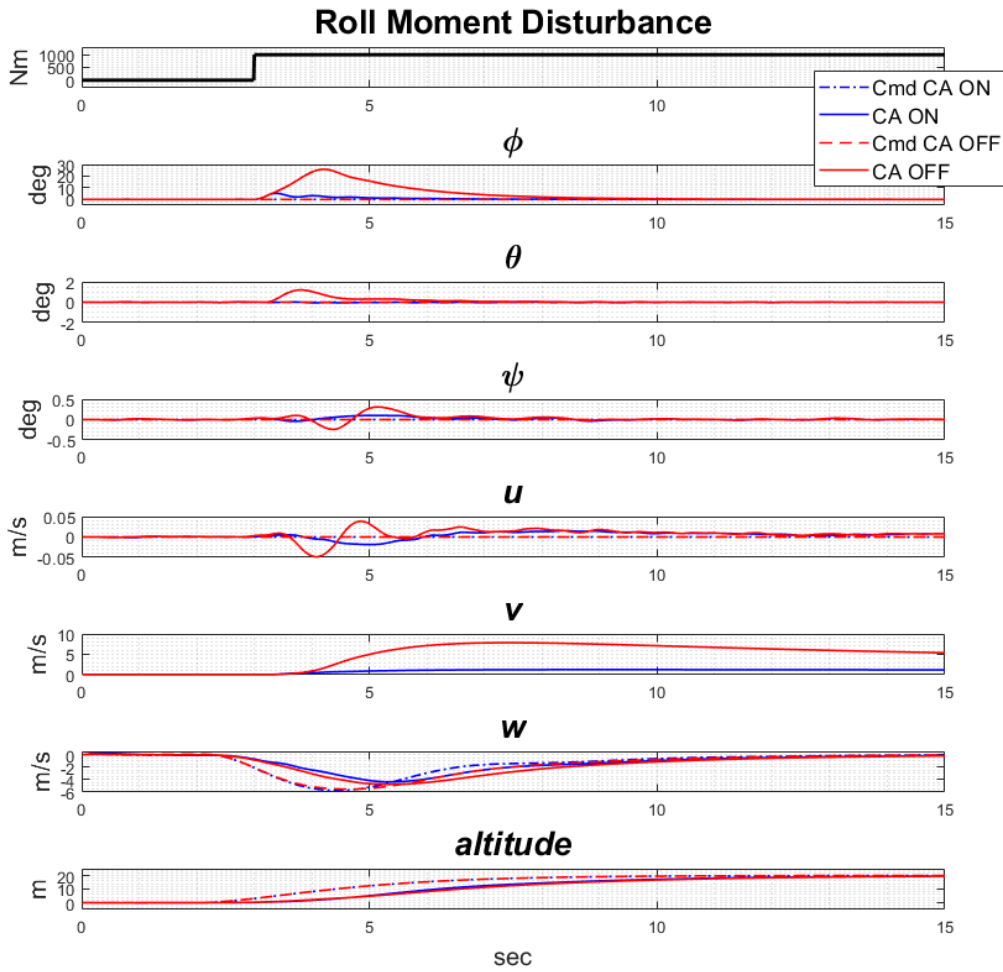


Figure 3.28: Roll moment disturbance rejection characteristics at hover with and without Control Allocation, states.

First, the results when the CA algorithm is not active are analyzed. *Remind that when the CA algorithm is not active, the pure INDI controller outputs are used, and only the pseudo-inverse approach that does not take into account actuator limits is considered*

for the allocation (see Equation 3.21).

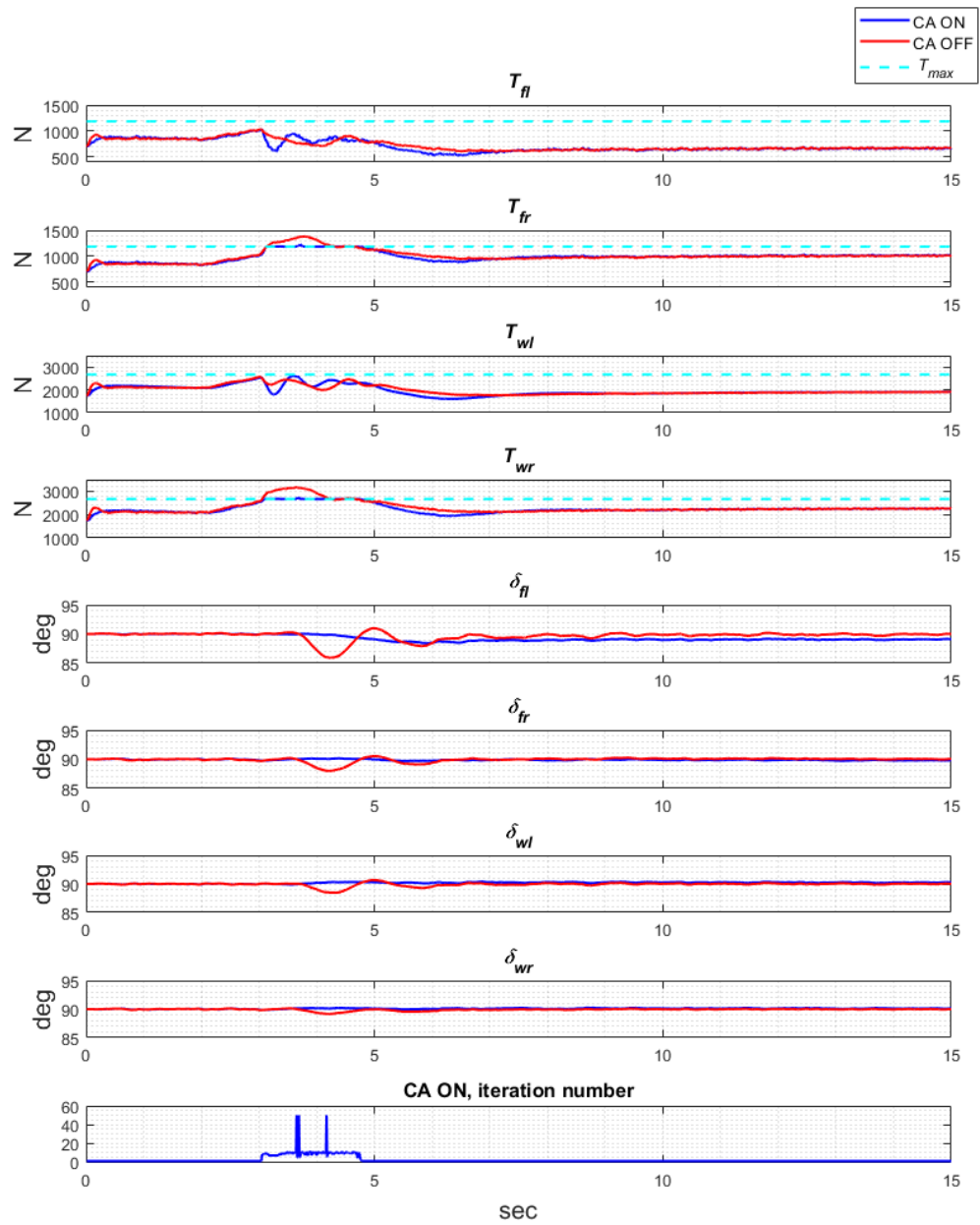


Figure 3.29: Roll moment disturbance rejection characteristics at hover with and without Control Allocation, actuator dynamics.

Based on Figure 3.28, at 3 seconds pilot gives climb command at hover and just after that a strong roll moment disturbance occurs. Then, the INDI controller increase

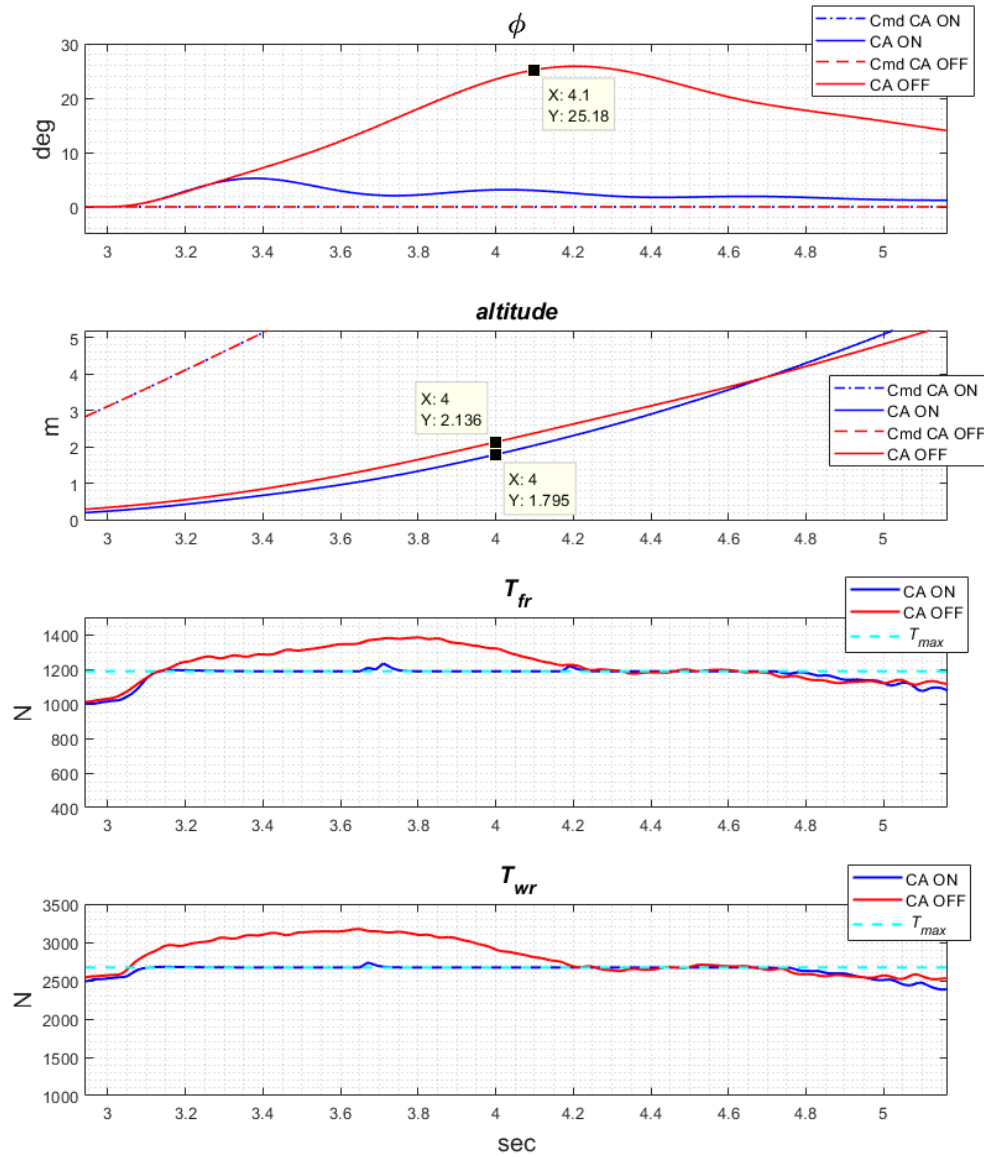


Figure 3.30: Roll moment disturbance rejection characteristics at hover with and without Control Allocation, the CA trade-off between roll moment disturbance rejection and altitude command tracking.

*thrust at right EDFs and decrease thrust at the left EDFs to reject the roll moment disturbance. However, all EDFs are already close to the maximum thrust limit due to the climb command. Additional thrust command generated by the INDI controller to reject the roll moment disturbance is not effective since the actuators are satu-*

rated (Figure 3.29). Then, roll moment disturbance cause large deviations on the roll and pitch angles while the actuators are saturated (Figure 3.28, red lines-CA OFF). When the same test is applied with the CA enabled, it is seen that the CA prioritizes the rotational channels over the translational channels (i.e., prioritizes the rejection of roll disturbance over the tracking of climb command), and consider the actuator limits in the optimum allocation. As a result, disturbance rejection characteristics are improved significantly thanks to the proper allocation of the limited control authority (Figure 3.28, blue lines-CA ON). The trade-off is the worsen tracking performance of the climb command. This is an expected result since the CA makes sure that rotational commands are tracked well as a first objective. Moreover, according to Figure 3.30, the performance loss on the altitude tracking when the CA is active is not significant. To conclude, the CA works very well and provides good disturbance rejection characteristics in case of limited control authority.

### 3.3.3.7 Inherent Robustness to the Modeling Errors: Error in Drag Coefficient

As mentioned in Section 3.3.2.2, the main advantage of the INDI controller is inherent robustness to modeling errors. As a reminder, the INDI control law given in Equation 3.21 is only dependent on the mass, inertia and level arms as model parameters. The other required model information is replaced with the sensor data thanks to the time-scale separation principle.

To test the INDI controller's inherent robustness to modeling errors, the transition from hover to cruise test is performed by multiplying the drag coefficient by 2. The error in drag coefficient is compensated by the INDI controller via minimizing the error between the measured and required state derivatives,  $\dot{x}_0$  and  $\dot{x}_{req}$  in Equation 3.20 respectively. Robustness to error in drag coefficient are analyzed comparing the simulation results for the nominal Cd and erroneous Cd cases. Figure 3.31 shows the state response and Figure 3.32 gives the actuator states and drag force for two test cases.

Based on the last plot of Figure 3.32, multiplying the drag coefficient by 2 increase the drag force at cruise condition approximately 997N (1693 – 696). To compensate the modeling error, the INDI controller generates further thrust at cruise condition

compared to the nominal case (red and blue lines in Figure 3.32). The total increase in the wing and front EDFs are roughly equal to  $964N$  ( $610 - 410 + 559 - 382 + 459 - 175 + 464 - 171$ ) which is consistent with increase in drag force due to the modeling error.

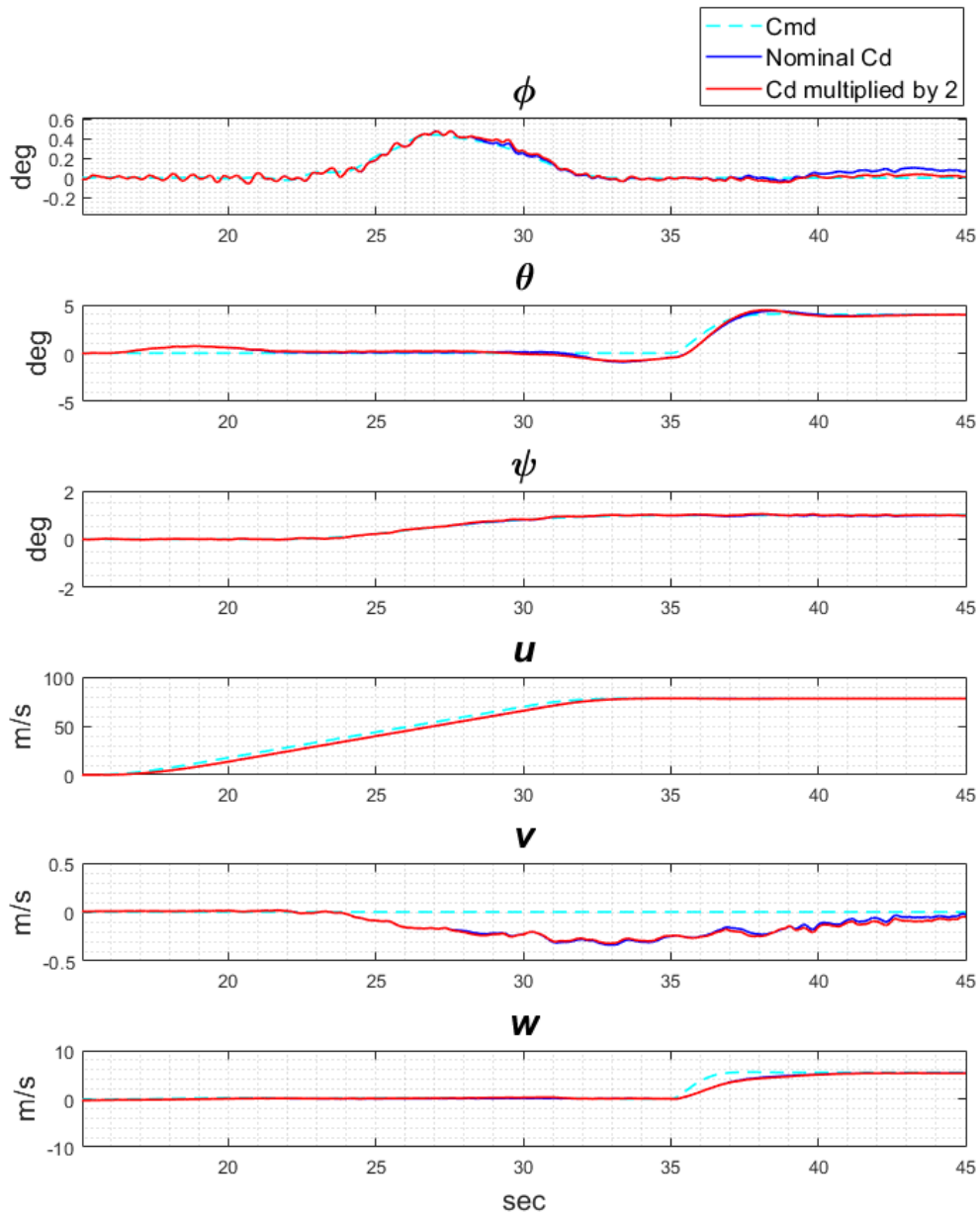


Figure 3.31: Inherent robustness to error in drag coefficient.

As given in Section 2.1.3, the forward flight model becomes dominant after 20 m/s

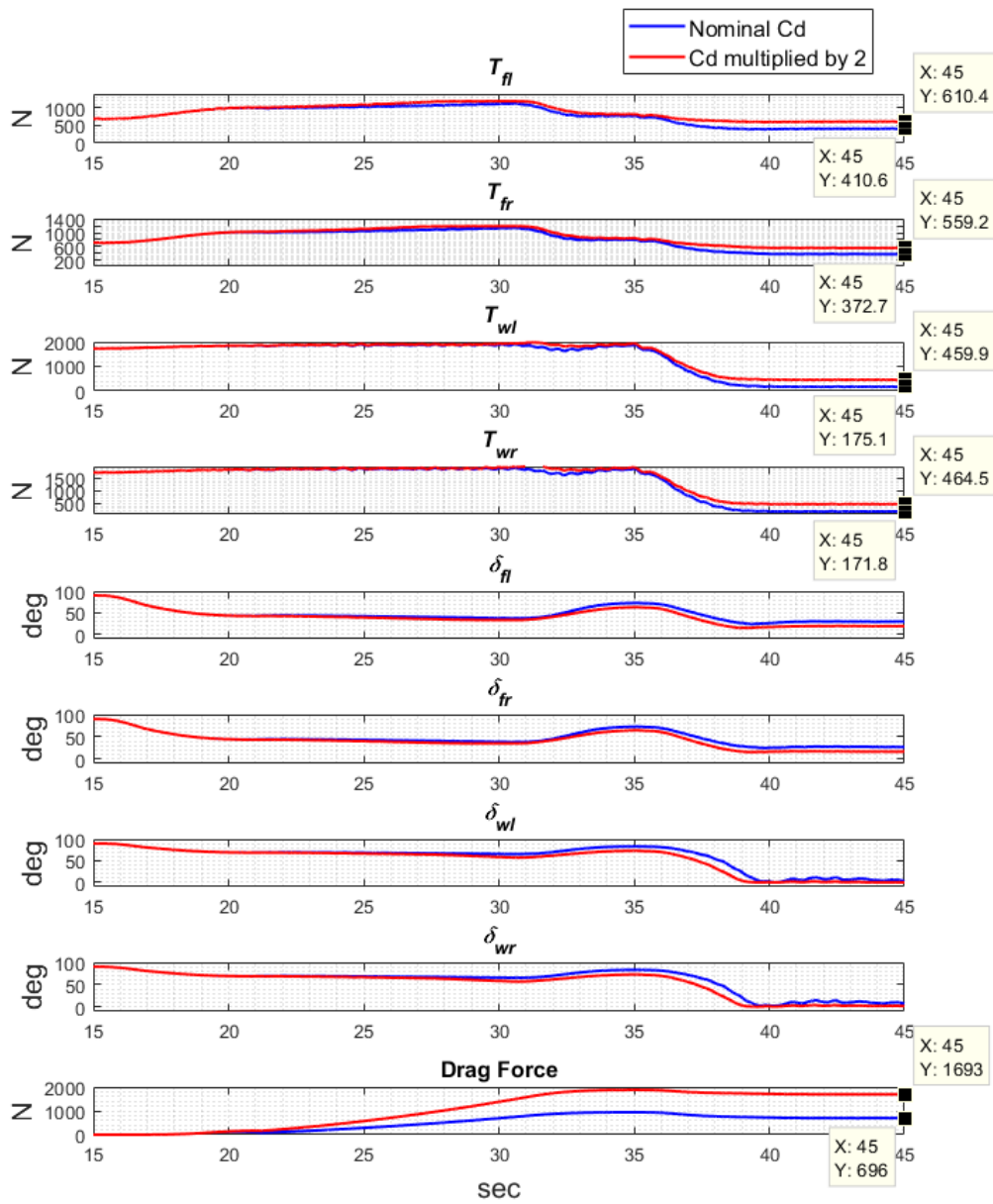


Figure 3.32: Inherent robustness to error in drag coefficient, actuator states.

airspeed. Therefore, it is expected to see adjustments in the EDF thrust to compensate the modeling error in drag coefficient after 20 m/s. This expectation is consistent with the results given in Figure 3.32.

*To conclude, the INDI controller is highly robust against the modeling errors as expected thanks to the sensor-based approach. As mentioned in Section 3.1, this is a*

*significant advantage considering the unified controller design problem for a unique aircraft that has highly nonlinear and coupled flight dynamics.*

In the next section, robustness of the controller against the model dependent parameters (i.e., mainly the mass and inertia) are analyzed in details.

### **3.3.3.8 Robustness to the Model Dependent Parameters: Error in Roll and Yaw Moment of Inertia and Mass**

In the previous section, inherent robustness to the modeling errors is analyzed applying error in drag coefficient. As a reminder, the INDI controller law given in Equation 3.22 is only dependent on the mass, inertia and lever arms. In this section, robustness to the error in model dependent parameters is analyzed.

Following robustness tests are performed to analyze the sensitivity to the modeling errors in mass and roll and yaw moment of inertia. Erroneous mass and roll/yaw moment of inertia values are applied up to the values that result in unstable response. All of tests are performed at hover trim condition. Results are given in Figures 3.33, 3.34, 3.35, 3.36, 3.37, and 3.38.

Based on the results, % 10 decrease and % 100 increase in the roll moment of inertia are tolerated by the controller (Figures 3.33, 3.34). Similarly, the controller can handle % 20 decrease and % 100 increase in the yaw moment of inertia (Figures 3.35, 3.36). In Figures 3.37 and 3.38, results of % 20 percent error in mass are given. As expected, the controller increase and decrease thrust accordingly when higher and lower mass values are applied, and stability is not effected at all.

*To conclude, the INDI controller has an acceptable level of robustness against the error in model dependent parameters (i.e., the mass and inertia) considering that only very large modeling errors cause instability.*



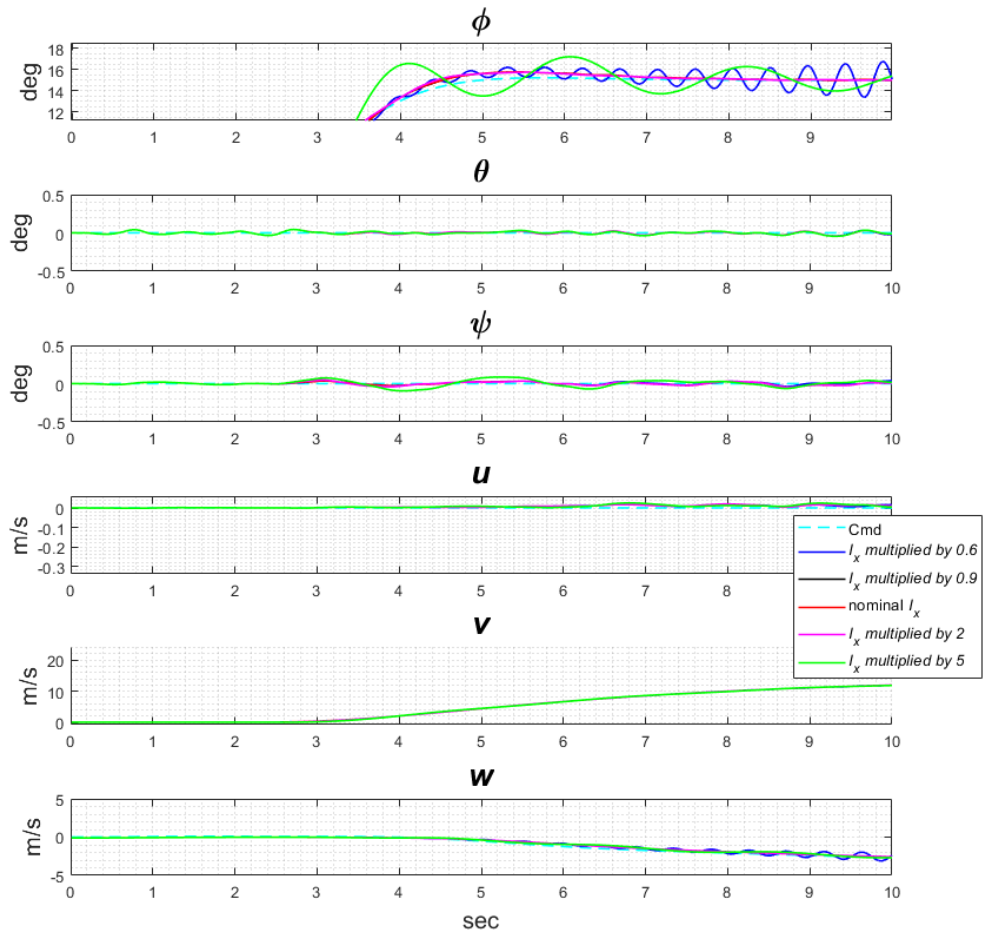


Figure 3.33: Robustness to error in roll moment of inertia, states.

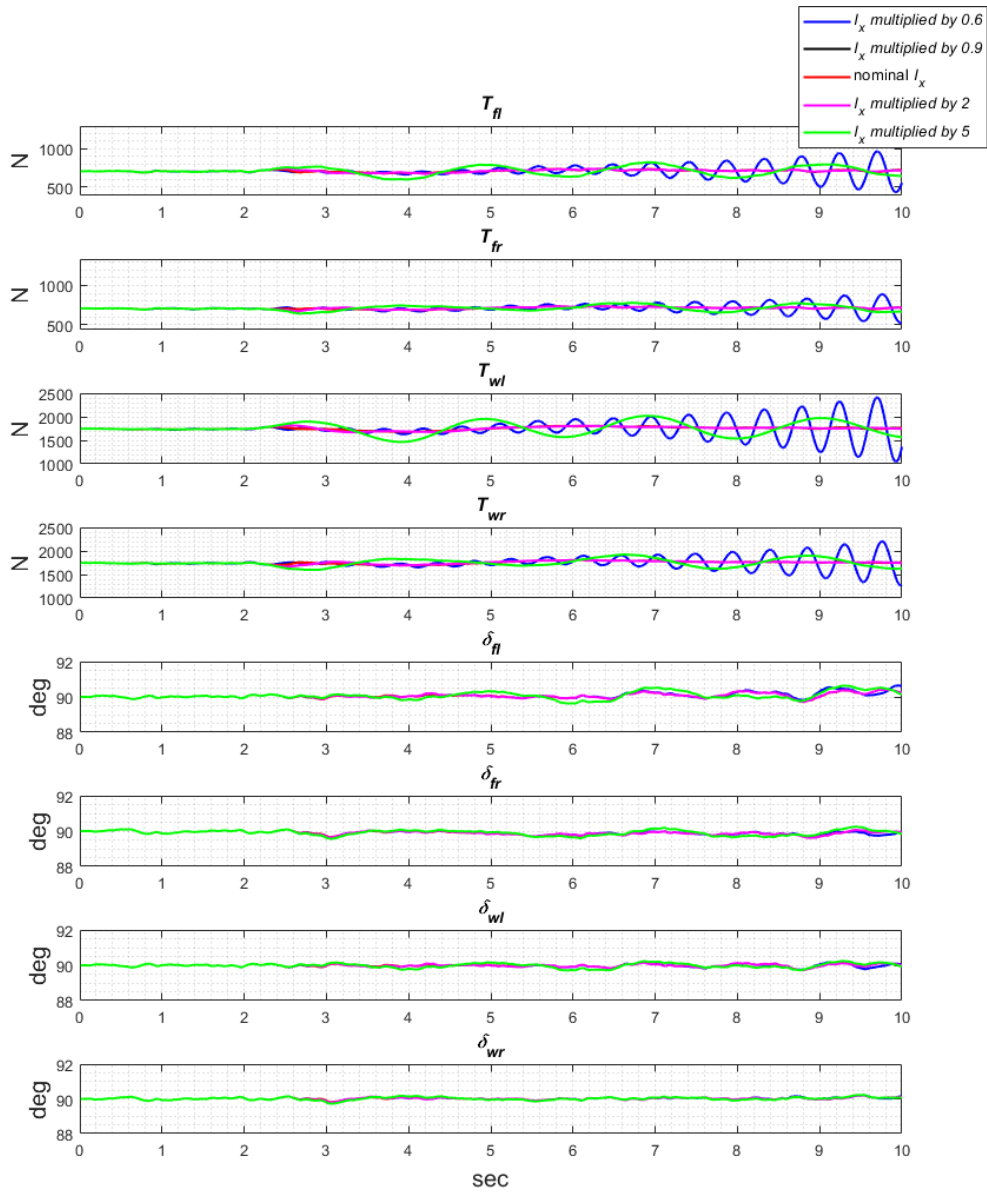


Figure 3.34: Robustness to error in roll moment of inertia, actuator states.

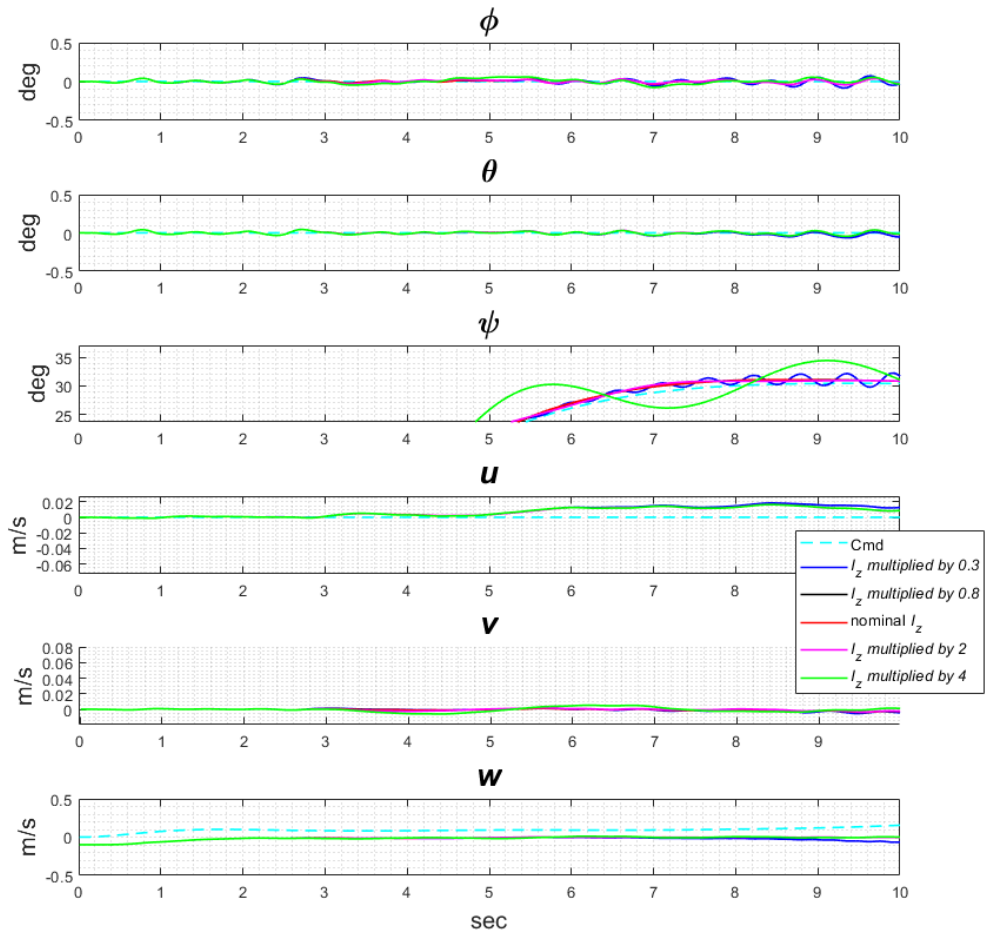


Figure 3.35: Robustness to error in yaw moment of inertia, states.

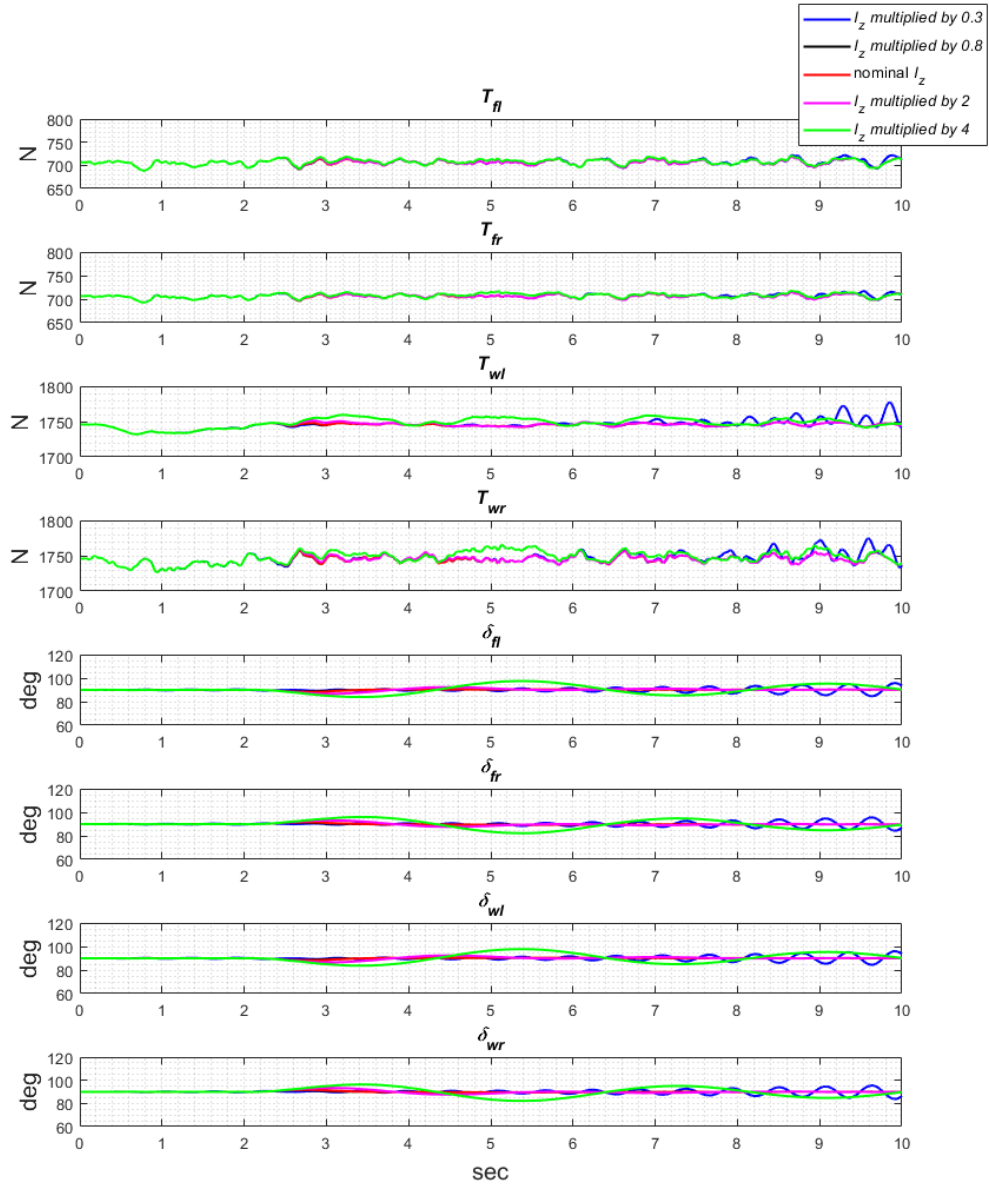


Figure 3.36: Robustness to error in yaw moment of inertia, actuator states.

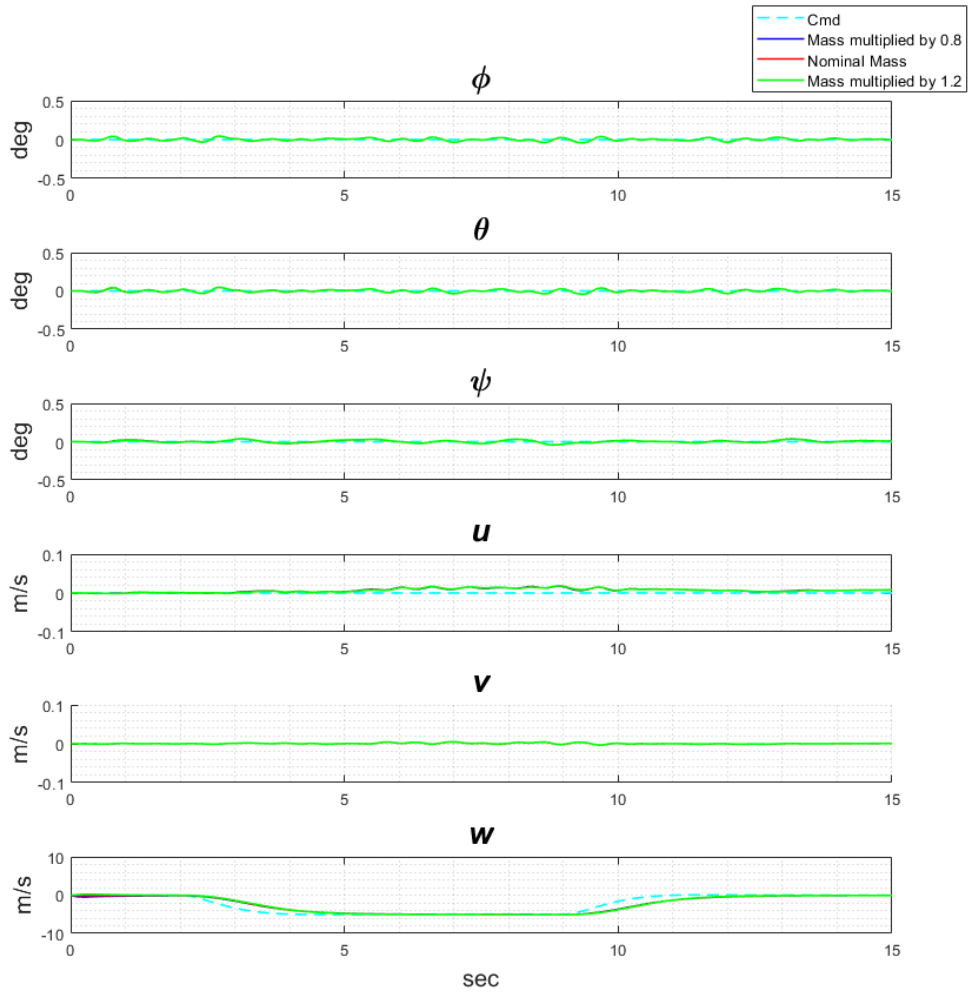


Figure 3.37: Robustness to error in mass, states.

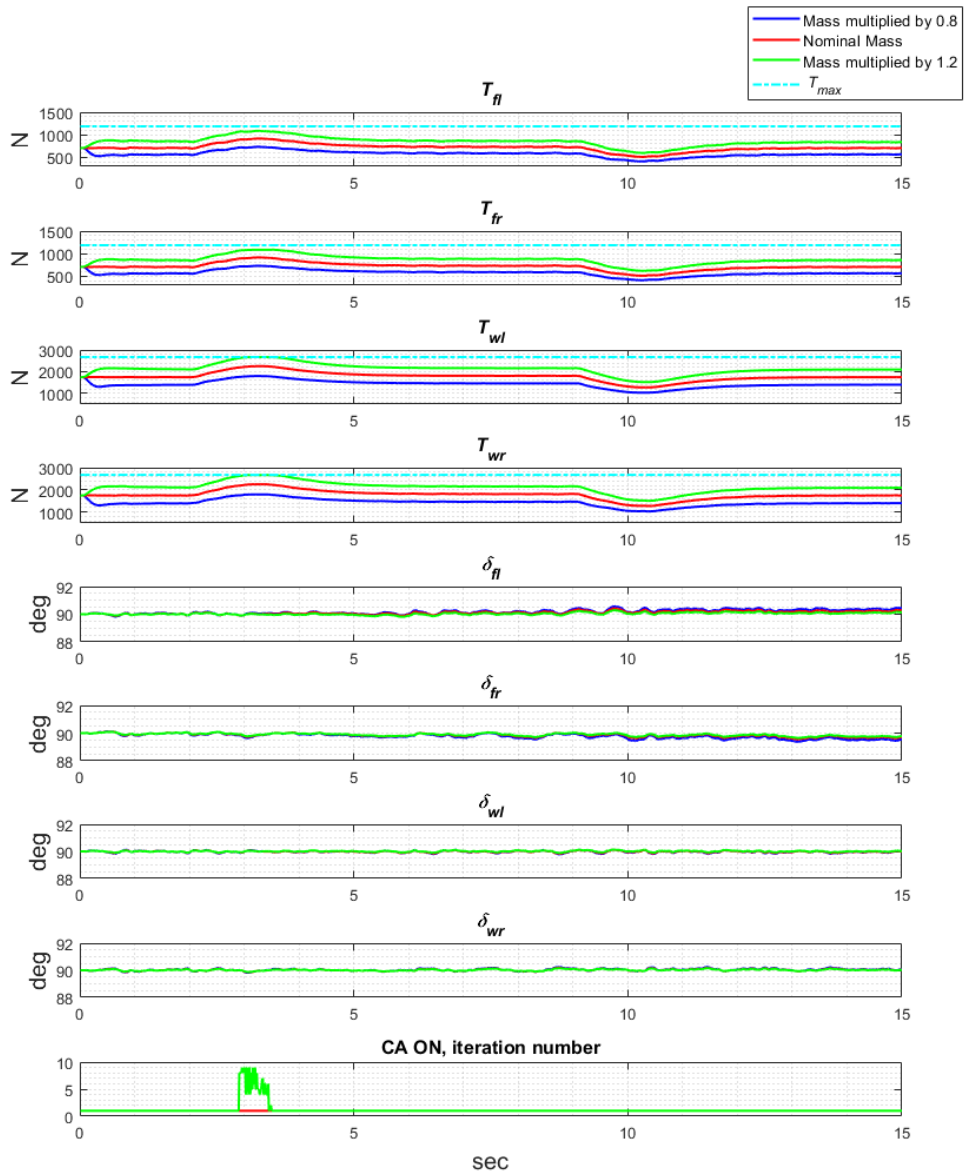


Figure 3.38: Robustness to error in mass, actuator states.

## CHAPTER 4

### CONCLUSION AND FUTURE WORKS

On-demand Urban Air Mobility (UAM) is an emerging concept that can shape the future of aviation. Distributed Electric Propulsion (DEP) eVTOL (Electric Vertical Takeoff and Landing) air-taxi concept has quite promising features considering the hard requirements of on-demand Urban Air Mobility. Combination of DEP eVTOL with fixed-wing aerodynamic surfaces provides efficient long range flight such that even regional all electric on-demand air-transportation becomes feasible. With this motivation, a novel fixed-wing eVTOL air-taxi with DEP concept is studied in this thesis. The air-taxi has a fixed-wing structure and numerous Electric Ducted Fans (EDFs) distributed through the front and wing sections of the air-taxi. EDFs are tilting to provide required thrust at hover, to overcome the drag at high speed forward flight, and to perform transition between the hover and forward flight. Air-taxi has longer range and endurance compared to the eVTOLs without a wing surface thanks to the aerodynamically efficient lift generation at high speed flight via fixed-wing surface. The air-taxi use pure thrust vector to achieve full envelope flight control, and conventional stability/control surfaces such as aileron, elevator, rudder, vertical/horizontal tail do not exist. This configuration makes the fixed-wing eVTOL air-taxi unique compared to the other concepts studied in the literature. Not having conventional control/stability surfaces has many advantages (e.g., improved aerodynamic efficiency at cruise, design flexibility-simplicity, better sizing-weight savings, etc.) However, it also comes with several problems/challenges regarding the flight control such as open-loop directional instability at forward flight, limited control authority at severe flight conditions, resolving actuator saturation is not straightforward due to the thrust vector couplings, etc. The full envelope flight control is achieved via controlling the thrust vector by adjusting rpm and tilt angle of several EDFs. The full flight

envelope of the air-taxi mainly consists of; vertical takeoff, transition from hover to forward flight, climb, cruise, descent, transition from forward to hover flight, and vertical landing. Due to the wide range of flight envelope, the flight dynamics model includes strong nonlinearities especially during the transition regions. Moreover, pure thrust vector control is highly coupled and over-actuated. Severe nonlinearities and couplings complicates the full envelope flight controller design for the novel eVTOL air-taxi.

The air-taxi studied has a novel configuration, and flight dynamics model is not available in the literature. Therefore, first a preliminary flight dynamics model is generated considering the wide flight envelope. Component build-up approach is used to generate the flight dynamics model for hover and forward flight models separately. To model the transition dynamics, hover and forward flight models are simply merged using the airspeed as the merging coefficient. Some of the effects (e.g., aero-propulsion couplings, ground effect at hover, etc.) are not included into the preliminary flight dynamics model since they require complex modeling study. A high fidelity flight dynamics model generation is not the scope of this study and can be part of a dedicated work focusing on aerodynamics and propulsion. Although some of the nonlinear effects are not modeled, the flight dynamics model has strong nonlinearities during the transition regions due to the merging of the hover and forward models, and coupled thrust vector control.

Considering the strong nonlinearities and couplings in the flight dynamics model, a sensor-based nonlinear control approach called Incremental Nonlinear Dynamic Inversion (INDI) is adapted to the control problem to design a unified flight controller valid for the entire flight envelope. The INDI is a promising control approach and has become popular in recent years thanks to the developments in sensor and computer technology. It is based on nonlinear dynamic inversion (NDI), but is has quite different characteristics due to the sensor-based incremental approach. The classical NDI is highly dependent on the aircraft model to perform the dynamic inversion accurately. On the other hand, the INDI replaces most of the model information with the acceleration estimations coming from the sensor measurements thanks to the time-scale separation principle. The INDI controller designed in this thesis use only the aircraft mass, inertia and EDF lever arms as model information in the control law. Therefore,



the modeling dependency is reduced significantly compared to the classical NDI. On the other hand, there are inherent problems of the INDI controller mainly due to the sensor-based incremental control approach (e.g., the sensor noise, delay, data synchronization, etc.). Noted that a realistic sensor model is added to the simulation model to verify the sensor-based INDI controller.

As mentioned, the aircraft has many tilting EDFs to control the thrust vector. Therefore, the system is highly over-actuated. Over-actuation and pure thrust vector control with strong couplings cause another challenge for the flight control. The problem is allocation of the limited control authority properly to guarantee stable flight in severe flight conditions. In literature, this problem is referred as "Control Allocation (CA)" in general. For the studied air-taxi, simulation results show that proper allocation of the limited control authority is very critical and must be solved carefully as part of the controller design. To allocate the limited control authority in case of actuator saturation, the relation between the control axis and control effectors/actuators need to be formulated. This relation is more straightforward for the aircraft with conventional control surfaces. However, for the studied air-taxi, the pure thrust vector control is used and, CA problem becomes more complicated due to the strong couplings. An optimization-based CA approach is designed and integrated into the INDI controller considering the described problems. Details of the INDI and CA design are given in Section 3.3. To conclude, an effective unified flight controller is designed and verified considering the challenges regarding the full envelope flight control of this novel eVTOL air-taxi that is not studied before to the best of author's knowledge. The contributions of the study are given in Section 3.1 in detail.

To verify the unified controller, several tests are performed using the nonlinear simulation model. Controller's tracking and stability performance is tested at different flight conditions considering the wide flight envelope. In addition, the CA design is tested via applying severe disturbances that limits the control authority and cause severe actuator saturation. It is observed that, the CA has a vital role of properly allocating the limited control authority and guaranteeing the stable flight as a first objective. The INDI controllers inherent robustness to modeling errors is verified via applying significant modeling error in flight dynamics model (i.e., the drag coefficient is multiplied by 2). As expected, the INDI controller can tolerate the error in flight

dynamics model very well so it has quite promising robustness to the modeling errors. Moreover, robustness to the model dependent parameters (i.e., the mass and inertia) are also tested to analyze the sensitivity of the controller considering that the only model information required for the INDI controller are the mass, inertia and EDF lever arms. Results show that the INDI controller has an acceptable level of robustness against the error in model dependent parameters considering that only very large modeling errors cause instability. To sum up, the unified controller's performance is satisfactory considering the full envelope flight control, disturbance rejection characteristics, and robustness to the modeling errors.

To conclude, a unified nonlinear controller is designed and verified for the novel fixed-wing eVTOL air-taxi considering the full envelope flight control challenges. Based on the several verification tests, the unified controller solves the defined problems effectively and shows satisfactory performance.

In future, the designed controller can be improved and analyzed considering other challenges in the design such as improved noise filtering in the INDI design, analyzing the INDI's sensitivity to sensor measurements, resolving rate-limit saturations in the CA algorithm, etc. Moreover, real-time implementation of the INDI controller with CA integration will be very valuable to analyze the feasibility of the proposed controller structure in real life. Real-time implementation is important since INDI is still a relatively new control approach. Therefore, verification via flight tests will be invaluable for the industrial projects and future INDI based controller studies. INDI controller's stability analyses is also an open topic for further researches. Theoretical stability proofs will encourage the real-time implementation of INDI. Other than the controller study, high fidelity flight dynamics modeling for the unique air-taxi can be topic of studies focusing on the aerodynamics and propulsion system modeling.

## REFERENCES

- [1] Airbus Vahana. <https://www.airbus.com/innovation/zero-emission/urban-air-mobility/vahana.html>, 2021. [Online; accessed 19-03-2021].
- [2] Aurora Flight Sciences. <https://www.aurora.aero/pav-evtol-passenger-air-vehicle/>, 2021. [Online; accessed 19-03-2021].
- [3] Crunchbase. <https://www.crunchbase.com/>, 2021. [Online; accessed 30-04-2021].
- [4] Digital DATCOM. [https://en.wikipedia.org/wiki/United\\_States\\_Air\\_Force\\_Stability\\_and\\_Control\\_Digital\\_DATCOM](https://en.wikipedia.org/wiki/United_States_Air_Force_Stability_and_Control_Digital_DATCOM), 2021. [Online; accessed 19-03-2021].
- [5] Digital DATCOM MATLAB Aerospace Toolbox. <https://www.mathworks.com/help/aerotbx/ug/importing-digital-datcom-data.html>, 2021. [Online; accessed 19-03-2021].
- [6] Ehang AAV. <https://www.ehang.com/ehangaav>, 2021. [Online; accessed 19-03-2021].
- [7] Graphic News. <https://www.graphicnews.com/en/pages/39120/aviation-lilium-air-taxi>, 2021. [Online; accessed 30-04-2021].
- [8] Joby Aviation. <https://www.jobyaviation.com>, 2021. [Online; accessed 19-03-2021].
- [9] Kittyhawk Aero. <https://kittyhawk.aero>, 2021. [Online; accessed 19-03-2021].

- [10] Lilium Jet. <https://lilium.com>, 2021. [Online; accessed 19-03-2021].
- [11] NASA Greased Lightning. [https://en.wikipedia.org/wiki/NASA\\_GL-10\\_Greased\\_Lightning](https://en.wikipedia.org/wiki/NASA_GL-10_Greased_Lightning), 2021. [Online; accessed 19-03-2021].
- [12] Pixhawk Flight Control Board. <https://ardupilot.org/dev/docs/learning-ardupilot-rc-input-output.html>, 2021. [Online; accessed 19-03-2021].
- [13] Schuebeler EDF. <https://www.schuebeler-jets.de/en/products/hst-en>, 2021. [Online; accessed 19-03-2021].
- [14] Volocopter GmbH. <https://www.volocopter.com/en/>, 2021. [Online; accessed 19-03-2021].
- [15] L. Abdallah and T. El-Shennawy. Reducing carbon dioxide emissions from electricity sector using smart electric grid applications. *Journal of Engineering*, 2013, 2013.
- [16] E. Abney and M. McDaniel. High angle of attack aerodynamic predictions using missile datcom. In *23rd AIAA applied aerodynamics conference*, page 5086, 2005.
- [17] B. D. Anderson and J. B. Moore. *Optimal control: linear quadratic methods*. Courier Corporation, 2007.
- [18] A. Ang, A. Gangoli Rao, T. Kanakis, and W. Lammen. Performance analysis of an electrically assisted propulsion system for a short-range civil aircraft. *Proceedings of the Institution of Mechanical Engineers, Part G: Journal of Aerospace Engineering*, 233(4):1490–1502, 2019.
- [19] K. J. Åström and R. M. Murray. *Feedback systems*. Princeton university press, 2010.
- [20] B. Bacon and A. Ostroff. Reconfigurable flight control using nonlinear dynamic inversion with a special accelerometer implementation. In *AIAA Guidance, Navigation, and Control Conference and Exhibit*, page 4565, 2000.

- [21] S. Baldwin. Carbon footprint of electricity generation. *London: Parliamentary Office of Science and Technology*, 268, 2006.
- [22] C. Banks. A discussion of methods of real-time airplane flight simulation. *A paper in Aerospace Engineering, The Pennsylvania State University*, 2000.
- [23] L. Barreda Pupo. Characterization of errors and noises in mems inertial sensors using allan variance method. Master's thesis, Universitat Politècnica de Catalunya, 2016.
- [24] R. Berger. Aircraft electrical propulsion—the next chapter of aviation. *Think: Act*, 10, 2017.
- [25] W. Blake. Prediction of fighter aircraft dynamic derivatives using digital datcom. In *3rd Applied Aerodynamics Conference*, page 4070, 1985.
- [26] W. B. Blake. Missile datcom: User's manual-1997 fortran 90 revision. Technical report, Air Force Research Lab Wright-Patterson AFB OH Air Vehicles Directorate, 1998.
- [27] S.-S. Boddupalli. *Estimating demand for an electric vertical landing and take-off (eVTOL) air taxi service using discrete choice modeling*. PhD thesis, Georgia Institute of Technology, 2019.
- [28] M. Bodson. Evaluation of optimization methods for control allocation. *Journal of Guidance, Control, and Dynamics*, 25(4):703–711, 2002.
- [29] N. K. Borer, C. L. Nickol, F. Jones, R. Yasky, K. Woodham, J. Fell, B. Litherland, P. Loyselle, A. Provenza, L. Kohlman, et al. Overcoming the adoption barrier to electric flight. In *54th AIAA Aerospace Sciences Meeting*, page 1022, 2016.
- [30] K. Budziak. *Aerodynamic Analysis with Athena Vortex Lattice (AVL)*. Hamburg: Aircraft Design and Systems Group (AERO), Department of Automotive . . . , 2015.
- [31] H. B. Chen and S. G. Zhang. Robust dynamic inversion flight control law design. In *2008 2nd International Symposium on Systems and Control in Aerospace and Astronautics*, pages 1–6. IEEE, 2008.

- [32] A. Deperrois. About xflr5 calculations and experimental measurements. *Presentation document*, 2009.
- [33] G. Di Francesco and M. Mattei. Modeling and incremental nonlinear dynamic inversion control of a novel unmanned tiltrotor. *Journal of Aircraft*, 53(1):73–86, 2016.
- [34] F. Dul, P. Lichota, and A. Rusowicz. Generalized linear quadratic control for a full tracking problem in aviation. *Sensors*, 20(10):2955, 2020.
- [35] W. Durham, K. A. Bordignon, and R. Beck. *Aircraft control allocation*. John Wiley & Sons, 2017.
- [36] D. Enns, D. Bugajski, R. Hendrick, and G. Stein. Dynamic inversion: an evolving methodology for flight control design. *International Journal of control*, 59(1):71–91, 1994.
- [37] T. Espinoza-Fraire, A. Dzul, F. Cortés-Martínez, and W. Giernacki. Real-time implementation and flight tests using linear and nonlinear controllers for a fixed-wing miniature aerial vehicle (mav). *International Journal of Control, Automation and Systems*, 16(1):392–396, 2018.
- [38] D. Finger, C. Braun, and C. Bil. The impact of electric propulsion on the performance of vtol uavs. 66. *Deutscher Luft-Und Raumfahrtkongress DLRK 2017*, 2017.
- [39] D. F. Finger, C. Braun, and C. Bil. A review of configuration design for distributed propulsion transitioning vtol aircraft. In *Asia-Pacific International Symposium on Aerospace Technology-APISAT*, pages 3–5, 2017.
- [40] T. Foster and J. Bowman. Dynamic stability and handling qualities of small unmanned-aerial vehicles. In *43rd AIAA Aerospace Sciences Meeting and Exhibit*, page 1023, 2005.
- [41] J. L. Freeman and G. T. Klunk. Dynamic flight simulation of spanwise distributed electric propulsion for directional control authority. In *2018 AIAA/IEEE Electric Aircraft Technologies Symposium (EATS)*, pages 1–15. IEEE, 2018.

- [42] A. S. Gohardani, G. Doulgeris, and R. Singh. Challenges of future aircraft propulsion: A review of distributed propulsion technology and its potential application for the all electric commercial aircraft. *Progress in Aerospace Sciences*, 47(5):369–391, 2011.
- [43] F. Grondman, G. Looye, R. O. Kuchar, Q. P. Chu, and E.-J. Van Kampen. Design and flight testing of incremental nonlinear dynamic inversion-based control laws for a passenger aircraft. In *2018 AIAA Guidance, Navigation, and Control Conference*, page 0385, 2018.
- [44] O. Harkegard. Efficient active set algorithms for solving constrained least squares problems in aircraft control allocation. In *Proceedings of the 41st IEEE Conference on Decision and Control, 2002.*, volume 2, pages 1295–1300. IEEE, 2002.
- [45] O. Härkegård and S. T. Glad. Resolving actuator redundancy—optimal control vs. control allocation. *Automatica*, 41(1):137–144, 2005.
- [46] J. Holden and N. Goel. Fast-forwarding to a future of on-demand urban air transportation (uber elevate, 2016).
- [47] T. A. Johansen and T. I. Fossen. Control allocation—a survey. *Automatica*, 49(5):1087–1103, 2013.
- [48] M. H. Khalesi, H. Salarieh, and M. S. Foumani. Dynamic modeling, control system design and mil–hil tests of an unmanned rotorcraft using novel low-cost flight control system. *Iranian Journal of Science and Technology, Transactions of Mechanical Engineering*, pages 1–20, 2019.
- [49] H. D. Kim, A. T. Perry, and P. J. Ansell. A review of distributed electric propulsion concepts for air vehicle technology. In *2018 AIAA/IEEE Electric Aircraft Technologies Symposium (EATS)*, pages 1–21. IEEE, 2018.
- [50] J. Koschorke, W. Falkena, E.-J. Van Kampen, and Q. P. Chu. Time delayed incremental nonlinear control. In *AIAA Guidance, Navigation, and Control (GNC) Conference*, page 4929, 2013.

- [51] M. Kreimeier, J. Reichmuth, and E. Stumpf. Evaluation of on-demand air mobility concepts with utilization of electric powered small aircraft. Technical report, Lehrstuhl und Institut für Luft-und Raumfahrtsysteme (ILR), 2018.
- [52] M. Kreimeier, P. Strathoff, D. Gottschalk, and E. Stumpf. Economic assessment of air mobility on-demand concepts. *Journal of Air Transportation*, 26(1):23–36, 2018.
- [53] S. H. Lane and R. F. Stengel. Flight control design using non-linear inverse dynamics. *Automatica*, 24(4):471–483, 1988.
- [54] F. L. Lewis, D. Vrabie, and V. L. Syrmos. *Optimal control*. John Wiley & Sons, 2012.
- [55] T. Lombaerts, J. Kaneshige, S. Schuet, B. L. Aponso, K. H. Shish, and G. Hardy. Dynamic inversion based full envelope flight control for an evtol vehicle using a unified framework. In *AIAA Scitech 2020 Forum*, page 1619, 2020.
- [56] T. Lombaerts, J. Kaneshige, S. Schuet, G. Hardy, B. L. Aponso, and K. H. Shish. Nonlinear dynamic inversion based attitude control for a hovering quad tiltrotor evtol vehicle. In *AIAA Scitech 2019 Forum*, page 0134, 2019.
- [57] F. Maschia. Model analysis with xflr5. *Radio Controlled Soaring Digest*, 25(2):27–51, 2008.
- [58] D. McLean. Automatic flight control systems(book). *Englewood Cliffs, NJ, Prentice Hall, 1990, 606*, 1990.
- [59] D. McLean and Z. Zaludin. Stabilization of longitudinal motion of a hypersonic transport aircraft. *Transactions of the Institute of Measurement and Control*, 21(2-3):99–105, 1999.
- [60] P. Menon, M. Badgett, R. Walker, and E. Duke. Nonlinear flight test trajectory controllers for aircraft. *Journal of Guidance, Control, and Dynamics*, 10(1):67–72, 1987.
- [61] M. D. Moore. Distributed electric propulsion (dep) aircraft. *NASA Langley Research Center*, 2016.



- [62] M. D. Moore and B. Fredericks. Misconceptions of electric propulsion aircraft and their emergent aviation markets. In *the 52nd Aerospace Sciences Meeting AIAA SciTech*, volume 17, 2014.
- [63] M. W. Oppenheimer, D. B. Doman, and M. A. Bolender. Control allocation for over-actuated systems. In *2006 14th Mediterranean Conference on Control and Automation*, pages 1–6. IEEE, 2006.
- [64] M. D. Patterson, B. J. German, and M. D. Moore. Performance analysis and design of on-demand electric aircraft concepts. In *12th AIAA Aviation Technology, Integration, and Operations (ATIO) Conference and 14th AIAA/ISSMO Multidisciplinary Analysis and Optimization Conference*, 2012.
- [65] T. Pollack, G. Looye, and F. Van der Linden. Design and flight testing of flight control laws integrating incremental nonlinear dynamic inversion and servo current control. In *AIAA Scitech 2019 Forum*, page 0130, 2019.
- [66] C. Pornet, C. Gologan, P. C. Vratny, A. Seitz, O. Schmitz, A. T. Isikveren, and M. Hornung. Methodology for sizing and performance assessment of hybrid energy aircraft. *Journal of Aircraft*, 52(1):341–352, 2015.
- [67] A. L. Prasuhn. Fundamentals of fluid mechanics. prentic-hall. *Inc., Englewood Cliffs, NJ*, 1980.
- [68] S. Rajendran and S. Srinivas. Air taxi service for urban mobility: a critical review of recent developments, future challenges, and opportunities. *Transportation research part E: logistics and transportation review*, 143:102090, 2020.
- [69] A. Reizenstein. Position and trajectory control of a quadcopter using pid and lq controllers, 2017.
- [70] C. Rosema, J. Doyle, L. Auman, M. Underwood, and W. B. Blake. Missile datcom user’s manual-2011 revision. Technical report, Army Aviation and Missile Research Development ENG CTR Redstone Arsenal AL . . . , 2011.
- [71] J. Roskam. *Airplane Design: Preliminary calculation of aerodynamic, thrust and power characteristics*. Roskam Aviation and Engineering Corporation, 1985.

- [72] J. Roskam. *Airplane flight dynamics and automatic flight controls*. DARcorporation, 1995.
- [73] J. M. Seddon and S. Newman. *Basic helicopter aerodynamics*, volume 40. John Wiley & Sons, 2011.
- [74] S. Sieberling, Q. Chu, and J. Mulder. Robust flight control using incremental nonlinear dynamic inversion and angular acceleration prediction. *Journal of guidance, control, and dynamics*, 33(6):1732–1742, 2010.
- [75] P. Simplício, M. Pavel, E. Van Kampen, and Q. Chu. An acceleration measurements-based approach for helicopter nonlinear flight control using incremental nonlinear dynamic inversion. *Control Engineering Practice*, 21(8):1065–1077, 2013.
- [76] J.-J. E. Slotine, W. Li, et al. *Applied nonlinear control*, volume 199. Prentice hall Englewood Cliffs, NJ, 1991.
- [77] E. Smeur, D. Höppener, and C. De Wagter. Prioritized control allocation for quadrotors subject to saturation. In *International Micro Air Vehicle Conference and Flight Competition*, number September, pages 37–43, 2017.
- [78] E. J. Smeur, M. Bronz, and G. De Croon. Incremental control and guidance of hybrid aircraft applied to the cyclone tailsitter uav. *arXiv preprint arXiv:1802.00714*, 2018.
- [79] E. J. Smeur, M. Bronz, and G. C. de Croon. Incremental control and guidance of hybrid aircraft applied to a tailsitter unmanned air vehicle. *Journal of Guidance, Control, and Dynamics*, 43(2):274–287, 2020.
- [80] E. J. Smeur, Q. Chu, and G. C. de Croon. Adaptive incremental nonlinear dynamic inversion for attitude control of micro air vehicles. *Journal of Guidance, Control, and Dynamics*, 39(3):450–461, 2016.
- [81] E. J. Smeur, G. C. de Croon, and Q. Chu. Gust disturbance alleviation with incremental nonlinear dynamic inversion. In *2016 IEEE/RSJ International Conference on Intelligent Robots and Systems (IROS)*, pages 5626–5631. IEEE, 2016.

- [82] E. J. Smeur, G. C. de Croon, and Q. Chu. Cascaded incremental nonlinear dynamic inversion for mav disturbance rejection. *Control Engineering Practice*, 73:79–90, 2018.
- [83] P. Smith. A simplified approach to nonlinear dynamic inversion based flight control. In *23rd Atmospheric Flight Mechanics Conference*, page 4461, 1998.
- [84] S. A. Snell, D. F. Enns, and W. L. Garrard Jr. Nonlinear inversion flight control for a supermaneuverable aircraft. *Journal of guidance, control, and dynamics*, 15(4):976–984, 1992.
- [85] T. J. Sooy and R. Z. Schmidt. Aerodynamic predictions, comparisons, and validations using missile datcom (97) and aeroprediction 98 (ap98). *Journal of spacecraft and rockets*, 42(2):257–265, 2005.
- [86] B. L. Stevens, F. L. Lewis, and E. N. Johnson. *Aircraft control and simulation: dynamics, controls design, and autonomous systems*. John Wiley & Sons, 2015.
- [87] E. Stumpf, M. Kreimeier, P. Strathoff, J. Lückhof, K.-U. Schröder, and F. Janser. Small aircraft concept for regional on-demand air mobility. In *Proceedings of the 31st ICAS Congress*, 2018.
- [88] E. C. Suicmez and A. T. Kutay. Attitude and altitude tracking of hexacopter via lqr with integral action. In *2017 International Conference on Unmanned Aircraft Systems (ICUAS)*, pages 150–159. IEEE, 2017.
- [89] S. Sun, L. Sijbers, X. Wang, and C. de Visser. High-speed flight of quadrotor despite loss of single rotor. *IEEE Robotics and Automation Letters*, 3(4):3201–3207, 2018.
- [90] Y. Suzuki, W. Dunham, I. Kolmanovsky, and A. Girard. Failure detection and control of distributed electric propulsion aircraft engines. In *AIAA Scitech 2019 Forum*, page 0109, 2019.
- [91] O. Tekinalp, T. Unlu, and I. Yavrucuk. Simulation and flight control of a tilt duct uav. In *AIAA Modeling and Simulation Technologies Conference*, page 6138, 2009.

- [92] O. Tekinalp and E. Yavuzoglu. A new steering law for redundant control moment gyroscope clusters. *Aerospace science and technology*, 9(7):626–634, 2005.
- [93] A. Tewari. *Advanced control of aircraft, spacecraft and rockets*, volume 37. John Wiley & Sons, 2011.
- [94] R. van't Veld, E.-J. Van Kampen, and Q. P. Chu. Stability and robustness analysis and improvements for incremental nonlinear dynamic inversion control. In *2018 AIAA Guidance, Navigation, and Control Conference*, page 1127, 2018.
- [95] J. D. Vasile, J. Bryson, and F. Fresconi. Aerodynamic design optimization of long range projectiles using missile datcom. In *AIAA Scitech 2020 Forum*, page 1762, 2020.
- [96] X. Wang, E.-J. v. Kampen, Q. Chu, and P. Lu. Incremental sliding-mode fault-tolerant flight control. *Journal of guidance, control, and dynamics*, 42(2):244–259, 2019.
- [97] X. Wang, E. Van Kampen, Q. Chu, and R. De Breuker. Flexible aircraft gust load alleviation with incremental nonlinear dynamic inversion. *Journal of Guidance, Control, and Dynamics*, 42(7):1519–1536, 2019.
- [98] X. Wang, E.-J. Van Kampen, Q. Chu, and P. Lu. Stability analysis for incremental nonlinear dynamic inversion control. *Journal of Guidance, Control, and Dynamics*, 42(5):1116–1129, 2019.
- [99] X. Wang, E.-J. Van Kampen, and Q. P. Chu. Gust load alleviation and ride quality improvement with incremental nonlinear dynamic inversion. In *AIAA Atmospheric Flight Mechanics Conference*, page 1400, 2017.
- [100] J. E. Williams and S. R. Vukelich. The usaf stability and control digital datcom. volume i. users manual. Technical report, McDonnell Douglas Astronautics Co St Louis Mo, 1979.
- [101] N. M. Zimmerman. *Flight control and hardware design of multi-rotor systems*. 2016.

## APPENDIX A

### ACTIVE SET ALGORITHM USED TO SOLVE THE CA PROBLEM

To solve the Control Allocation problem defined in Equation 3.27, following active set algorithm described in [44] is used. First, problem is defined in weighted least squares form. Then, the cost function is rewritten as in Algorithm 3.3 given below. Finally, Algorithm 3.1 is applied to solve the optimization problem using the active set method.

The critical part of the CA design is integration of the incremental constraint evaluation considering the INDI controller structure. Details are given in Section 3.3.2.7.

$$u_W = \arg \min_{\underline{u} \leq u \leq \bar{u}} \|W(u - u_p)\|^2 + \gamma \|W_a(Bu - v)\|^2$$

---

*Algorithm 3.3 (Active set algorithm for weighted LS)*

---

1. Let  $u^0$  and  $\mathcal{W}$  be the resulting solution and working set from the previous sampling instant.
2. Rewrite the cost function as

$$\|W(u - u_p)\|^2 + \gamma \|W_a(Bu - v)\|^2 = \left\| \underbrace{\begin{pmatrix} \gamma W_a B \\ W \end{pmatrix}}_A u - \underbrace{\begin{pmatrix} \gamma W_a v \\ W u_p \end{pmatrix}}_b \right\|^2$$

and solve

$$u_W = \arg \min_u \|Au - b\|$$

$$\underline{u} \leq u \leq \bar{u}$$

using Algorithm 3.1.

---

**Algorithm 3.1 (Active set algorithm)**

---

Let  $u^0$  be a feasible starting point. A point is feasible if it satisfies (6b) and (6c). Let the working set  $\mathcal{W}$  contain (a subset of) the active inequality constraints at  $u^0$ .

for  $k = 0, 1, 2, \dots, N - 1$

    Given  $u^k$ , find the optimal perturbation  $p$ , considering the constraints in the working set as equality constraints and disregarding the remaining inequality constraints. Solve

$$\begin{aligned} \min_p \quad & \|A(u^k + p) - b\| \\ & Bp = 0 \\ & p_i = 0, \quad i \in \mathcal{W} \end{aligned}$$

    if  $u^k + p$  is feasible

        Set  $u^{k+1} = u^k + p$  and compute the Lagrange multipliers,  $\begin{pmatrix} \mu \\ \lambda \end{pmatrix}$ , where  $\mu$  is associated with (6b) and  $\lambda$  with the active constraints in (6c).

        if all  $\lambda \geq 0$

$u^{k+1}$  is the optimal solution to (6).

        else

            Remove the constraint associated with the most negative  $\lambda$  from the working set.

    else

        Determine the maximal step length  $\alpha$  such that  $u^{k+1} = u^k + \alpha p$  is feasible. Add the primary bounding constraint to the working set.

end

---

## CURRICULUM VITAE

### PERSONAL INFORMATION

**Surname, Name:** Suiçmez, Emre Can

**Nationality:** Turkish (TC)

**Date and Place of Birth:** 31.08.1988, Ankara

**Marital Status:** Married

**Phone:** 0 533 3804982

### EDUCATION

<b>Degree</b>	<b>Institution</b>	<b>Year of Graduation</b>
M.S.	METU Aerospace Engineering	2014
B.S.	METU Aerospace Engineering	2011
High School	Atatürk Atatürk High School	2006

### PROFESSIONAL EXPERIENCE

<b>Year</b>	<b>Place</b>	<b>Enrollment</b>
2021-Present	TÜBİTAK BİLGEM İLTAREN	Researcher
2020-2021	Lilium GmbH	Design Engineer
2016-2020	TÜBİTAK BİLGEM İLTAREN	Researcher
2014-2016	Turkish Aerospace Industries (TAI)	Design Engineer
2012-2014	METU Aerospace Engineering	Research Assistant

## **PUBLICATIONS**

1. Suiçmez E.C., Kutay A.T., Hexacopter control with input constraints: Comparison between model predictive control and LQR, 10th Ankara International Aerospace Conference, Ankara, TURKEY, 2019
2. Suiçmez E.C., Kutay A.T., Longitudinal automatic landing controller design by using optimization methods, 10th Ankara International Aerospace Conference, Ankara, TURKEY, 2019
3. Suiçmez E.C., Kutay A.T., Attitude and altitude tracking of hexacopter via LQR with integral action, International Conference on Unmanned Aircraft Systems, 150-159, Miami, USA, 2017
4. Suiçmez E.C., Kutay A.T., Path tracking control of a quadrotor UAV with backstepping method, Journal of Aeronautics and Space Technologies 7 (2), 1-13, 2014
5. Suiçmez E.C., Trajectory tracking of a quadrotor unmanned aerial vehicle (uav) via attitude and position control, METU Master Thesis, 2014
6. Suiçmez E.C., Kutay A.T., Optimal path tracking control of a quadrotor UAV, 2014 International Conference on Unmanned Aircraft Systems, 115-125, Orlando, USA, 2014